



UNIVERSITY OF
BIRMINGHAM

**Ex-situ Characterisation of Solid Oxide Fuel Cell Operating on
Biogas using Tin Anode-infiltration**

by

Rizki Putri Andarini

A thesis submitted to
The University of Birmingham
for the degree of

MASTER OF RESEARCH

**Chemical Engineering
School of Engineering
University of Birmingham
Edgbaston
Birmingham
B15 2TT**

September 2017

UNIVERSITY OF
BIRMINGHAM

University of Birmingham Research Archive

e-theses repository

This unpublished thesis/dissertation is copyright of the author and/or third parties. The intellectual property rights of the author or third parties in respect of this work are as defined by The Copyright Designs and Patents Act 1988 or as modified by any successor legislation.

Any use made of information contained in this thesis/dissertation must be in accordance with that legislation and must be properly acknowledged. Further distribution or reproduction in any format is prohibited without the permission of the copyright holder.

Abstract

This work presents ex-situ characterisation and cell performance of Sn-infiltration on SOFC anodes for SOFC operating in biogas dry reforming. Using commercially available Ni-YSZ-based anode supported full cells with LSCF cathode layers, Sn-infiltrated Ni-YSZ SOFCs containing different amounts of Sn were manufactured. The pipette drop infiltration technique was selected to introduce the Sn onto the anode surface as it was cheap, easy, repeatable, and reproducible. Mixed $\text{SnCl}_2 \cdot 2\text{H}_2\text{O}$ and 95 vol% ethanol was added drop by drop before being calcined at 600°C for 2 hours. Hydrogen and simulated biogas feed (1:2 volume ratio of $\text{CO}_2:\text{CH}_4$) were used for their electrochemical performance on dry reforming operation. Helium was added to the fuel for neutral gas and mass spectrometer measurements. Sn-infiltrated Ni-YSZ SOFCs had higher and more stable performance at 750°C dry reforming on biogas compared to the non-infiltrated cells. The best performance was shown from the 1 wt% Sn content on the anode surface with 0.38 W/cm^2 and 0.65 A/cm^2 . Sn/Ni-YSZ SOFCs also showed decreased carbon formation effect as the ohmic and transport limitations were sharply reduced. Various ex-situ characterisations such as SEM-EDX, XRF, XRD, and XPS were applied to the samples, with or without Sn-infiltration. The YSZ sites stayed in the same phase after reduction with hydrogen overnight. Meanwhile, after reduction, the Sn-infiltration Ni-YSZ was shown to have Ni metal, Ni_3Sn , NiO, SnO and YSZ phases. Sn is concluded to be forming Sn/Ni alloy which helps Ni-YSZ SOFCs increase the performance around 120 % in dry reforming on biogas operation.



In The Name of Allah, The Most Beneficent, The Most Merciful

Allah – there is no deity except Him, the Ever-Living, the Sustainer of All existence. Neither drowsiness overtakes Him nor sleep. To Him belongs whatever is in the heavens and whatever is on the earth. Who is it that can intercede with Him except by His permission? He knows what is presently before them, and they encompass not a thing of His knowledge except for what He wills. His Kursi extends over the heavens and the earth, and their preservation tires Him not. And He is the Most High, the Most Great. (QS 2: 255) And say, My Lord, cause me to enter a sound entrance and to exit a sound exit and grant me from Yourself a supporting authority. (QS 17: 80)

(Al-Qur'an, Surah 2. (Al Baqarah) verses 255, Surah 17. (Al Isra) verses 80)

I dedicate this thesis for my mother and my brother

For all their endless support and prayers

For everything

Acknowledgements

All praise is only Allah's, the Lord of the Worlds, who had allowed me to conduct this study and finish the thesis.

I am grateful to my supervisor Prof. Robert Steinberger-Wilckens for their continuous supports, assistance and invaluable guidance during the two years of my study. Thank you also to Dr. Lina Troskialina and Dr. Emily Smith for their invaluable insight and knowledgeable advice for this thesis writing.

I would like to also thank the Indonesia Endowment Fund for Education (LPDP) from Ministry of Finance Indonesia, for providing the scholarship for me to undertake and finish this study.

This study would not have been possible without the assistance of the administration and technical staffs at the University of Birmingham; namely Mrs Lynn Draper, John Hooper, Jackie Deans, Artur Majewski and Jong-Eun Hong. To them I am very grateful.

I would also like to offer my kindest thanks to my colleagues at the Fuel Cells and Hydrogen Research Centre for their supports and helps. Thank you, especially to Sophie, Anisa, Melissa, and Oujen to name but a few.

Special thanks go to my personal support-system: Chintari Dewi, Ruth Gultom, Nabila Aisa, Ryan Nugroho, Dwi Insani, Rinna Sijabat, Hanjaya Ekaputra, Indy Cesara and the ever-crazy partner in crime Enrico Gianino, who give their times, days and nights, to bring joy, support, and positivity all these years.

Finally, I would like to thank my loved ones, Mama, Papa, Mbak Mahar, Mas Nanang, Teh Helmy, Lana, Raziq and Nadzira, who never give up on me even when I nearly give up on myself. I hope I can make you guys proud of me.

Table of Content

Chapter 1 Introduction	1
1.1 Overview	2
1.2 Clean Alternative Energy.....	7
1.3 Fuel Cells	9
1.4 Solid Oxide Fuel Cell.....	14
1.5 Biogas as Fuel	21
1.6 Project Aim and Objectives.....	28
Chapter 2 Literature Review	30
2.1 Overview	31
2.2 Hydrogen Production on Nickel-based Catalyst	31
2.2.1 Nickel in Alloys	37
2.2.2 Nickel-based alloys in SOFCs.....	39
2.3 Internal Reforming of Methane	42
2.4 Anode Supported Utilization with Sn Dopant Addition	50
2.5 Tin Performance on Fuel Cells	53
Chapter 3 Methods and Materials.....	60
3.1 Overview	61
3.2 Materials	61
3.3 Methods.....	63
3.3.1 SOFC Sn-infiltration method via pipette drop	64
3.3.2 SOFC manufacturing steps.....	66
3.3.3 Electrical performance test	70
3.3.4 SOFC outlet gas monitoring	71
3.4 Imaging and Characterisation	72
Chapter 4 Cell Testing.....	76
4.1 Overview	77
4.2 Preparation of the Cell	77
4.2.1 Undoped Cell	88
4.2.2 Doped Cell	88
4.3 Cell Testing	89
4.3.1 Preparation Before the Cell Testing	90
4.3.2 Cell Testing Results.....	92
Chapter 5 Cell Characterisation.....	105
5.1 Overview	106
5.2 Before Reduction	107
5.2.1 SEM-EDX.....	107
5.2.2 XRF.....	115
5.2.3 XRD.....	118
5.2.4 XPS.....	123
5.3 After Reduction	126

5.3.1	SEM-EDX.....	127
5.3.2	XRF.....	129
5.3.3	XRD.....	132
5.3.4	XPS.....	135
Chapter 6 Conclusions.....		140
6.1	Overview	141
6.2	Main Points	141
6.3	Further Work.....	142
Bibliography		143

List of Figures

Figure 1 Global greenhouse gas emissions by gas [2]	2
Figure 2 Global greenhouse gas emissions by economic sector [2]	2
Figure 3 World rankings of four climates impacts based on extreme weather, sea level rise, agricultural productivity loss and overall effects	3
Figure 4 Standard activation energy diagram for an exothermic reaction [20]	10
Figure 5 SEM cross section of SOFC and the reaction that occurs [29]	15
Figure 6 SOFC single cell configuration: (a) electrolyte-supported, (b) anode-supported, (c) cathode- supported [A=Anode layer, E=Electrolyte layer, C=Cathode Layer] *figures not drawn to scale	16
Figure 7 Japan schematic diagram for Fuel Cell development [41]	19
Figure 8 Biogas plant for farm scale [https://www.host.nl/en/biogas-plants/ ; accessed on 22 March 2018]	21
Figure 9 Fundamental steps for anaerobic digestion [www.e-inst.com/biomass-to-biogas/ ; accessed on 21 March 2017]	25
Figure 10 Formation of monomers [48].....	25
Figure 11 Methane formation from acetate and carbon dioxide [48]	28
Figure 12 Common nickel catalyst transformation from electropositive d^{10} transition metal [65]	33
Figure 13 Filamentous carbon spreading inside an anode SOFC [84]	35
Figure 14 Classification of super alloys [88].....	38
Figure 15 The electron and oxygen ions course within the solid oxide fuel cells [91]	40
Figure 16 Equilibrium constant of reactions involved in the methane-carbon dioxide reaction at different temperatures, at atmospheric pressure [96]	46
Figure 17 Position of the mixtures of inlet gases in the carbon-hydrogen-oxygen ternary diagram [97]	47
Figure 18 Comparison of the outlet gas composition at 800° (~70 mg): (a) pure methane, (b) $CO_2:CH_4 = 1$, (c) $CO_2:CH_4 = 2$, (d) $CO_2:CH_4 = 3$ [97]	48
Figure 19 Carbon dioxide conversion as a function of temperature and CO_2/CH_4 ratio at 1 atm and for $n_{(CH_4+CO_2)} = 2$ mol [96]	49
Figure 20 Comparison of measurements (symbols) and model (solid lines) for dry reforming (CO_2) within the anode ($CH_4 = 0.20$, $H_2 = 0.028$, $Ar = 0.772$, $CO_2 = 0.5$, temp 800°C) [98]	50

Figure 21 The measured conductivity plotted against calculated adsorption energies of oxygen on the close-packed pure metal surface [106]	51
Figure 22 The measured conductivity plotted against calculated adsorption energies of hydrogen on the close-packed pure metal surface [106]	52
Figure 23 Ni/Sn phase diagram [137]	54
Figure 24 DFT-calculated reaction energies for C-C and C-O bond formation on a) Ni (111) and b)Sn/Ni (111) [63].....	55
Figure 25 DFT calculated adsorption energies per carbon atom for a C atom, C ₈ cluster, and a graphene chain adsorbed on Ni (211) and Sn/Ni (211) [63].....	56
Figure 26 Normalised methane conversion as a function of the time on stream for 1 wt% Sn/Ni/YSZ, 5 wt% Sn/Ni/YSZ, and Ni/YSZ catalysts measured at the steam-to-carbon ratio of 0.5 and at 800°C [63].....	56
Figure 27 Comparison in current density performance between Ni-YSZ and Sn/Ni-YSZ in various Sn compositions (2 drops, 4 drops, 6 drops and 10 drops) [136].....	58
Figure 28 Full cell with LSCF cathode with 30 mm outside diameter and 22 mm inner diameter	62
Figure 29 Side image of the cell sample	62
Figure 30 Anode side of the cell sample	62
Figure 31 Cathode side of the cell sample	62
Figure 32 Sample cells when drying in air in between drops	64
Figure 33 weighing each sample before and after treatment.....	65
Figure 34 Temperature profile for calcination of Sn infiltrated via pipette drop	66
Figure 35 Cell holder made from an alumina (macor) cylinder with ceramabond sealing	67
Figure 36 Silver paste application on the cathode side	68
Figure 37 Silver paste application on the anode side	68
Figure 38 Cell holder preparation for mounting the SOFC sample	68
Figure 39 After 12 hours drying in 150° C for sealing the rim of the mounted sample	69
Figure 40 Close-up look of the cathode side after sealing the sample.....	69
Figure 41 Schematic diagram of the test rig *drawn not to scale	70

Figure 42 The image model of fluorescence occurrence [https://www.bruker.com/products/x-ray-diffraction-and-elemental-analysis/handheld-xrf/how-xrf-works.html , accessed on 22 August 2017]	73
Figure 43 Photoelectron process in XPS [141]	75
Figure 44 SEM images anode surface with 5000x magnification of a) AS+AFL, b) Half-cell, c) LSM Full-cell, d) LSCF Full-cell	78
Figure 45 XRD analysis on anode surface a) LSM Full-cell, b) AS+AFL, c) Half-cell, and d) LSCF Full-cell (as supplied)	80
Figure 46 Improvement in cathode screen printing (SP) performance and improved LSCF cathodes by standard Juelich cells [143]	81
Figure 47 Hf peak scan from XRF analysis.....	84
Figure 48 Typical XRF scan result for LSCF type (impurities label removed)	84
Figure 49 Principle photoelectron peaks of undoped LSCF Full-cell sample (reference for the XPS analysis) from the anode surface.....	85
Figure 50 Comparison XPS spectra for one element a) Ni 2p spectrum of Undoped cell, b) High resolution Ni 2p spectrum of pure Ni metal[http://xpssimplified.com/elements/nickel.php], and c) Ni2p spectra of Ni oxide and hydroxide [http://xpssimplified.com/elements/nickel.php]	86
Figure 51 Ni 2p _{3/2} spectral fitting parameter: binding energy (eV), percentage of total area, FWHM value (eV) for each pass energy, and spectral component separation (eV)[146,147]	87
Figure 52 OCV at the starting cell testing in hydrogen fuel between UD, 4D, and 6D cells	94
Figure 53 OCV at the starting cell testing in biogas fuel between UD, 4D and 6D	95
Figure 54 OCV states comparison at 13 hours operation in hydrogen fuel between UD, 4D, and 6D	96
Figure 55 OCV states comparison at 23 hours operation in biogas fuel between UD, 4D, and 6D ...	97
Figure 56 IV curves at 6 hours operation on hydrogen fuel	98
Figure 57 IV curves at 8 hours operation on biogas fuel	98
Figure 58 IV curves comparison on biogas operation with the additional 3D cell testing	99
Figure 59 EIS spectra of Sn-infiltrated SOFCs comparison between hydrogen and biogas fuel	100
Figure 60 Typical mass spectra of outlet gases of an undoped samples on biogas operation	103
Figure 61 Typical mass spectra of outlet gases of a doped samples on biogas operation.....	104

Figure 62 SEM images for an undoped cell using three different detectors in 500x magnification for the same area, (a) BSE, (b) SE, and (c) EDX	108
Figure 63 EDX area scan at 500x magnification and 15 kV for undoped cell	109
Figure 64 SEM imaging spots	110
Figure 65 The formation of surface tension phenomenon on Sn-infiltration with pipette drop technique	113
Figure 66 EDX scan of surface area phenomenon and SnO sites on the surface of the anode	114
Figure 67 4D sample XRF scan result (impurities label removed)	117
Figure 68 XRD analysis for undoped cells	119
Figure 69 XRD spectrum analysis for 4D samples	120
Figure 70 XRD spectrum analysis for 6D samples	120
Figure 71 Superimposed XRD spectra of UD, 4D and 6D	120
Figure 72 XRD spectra comparison of 4D cell with three in-house cells: NiYSZ_1, NiYSZ_2, and NiYSZ_3	121
Figure 73 Sn 3d/5 spectrum BR sample	124
Figure 74 O 1s/4 spectrum BR sample	124
Figure 75 BSE images of 4D samples AR at 500x magnification	127
Figure 76 XRF qualitative scan for 4D (impurities removed)	131
Figure 77 XRD spectrum of after reduction UD sample	133
Figure 78 XRD spectrum of after reduction 4D sample	134
Figure 79 XRD spectrum of after reduction 6D sample	134
Figure 80 Superimposed XRD spectra of UD, 4D, and 6D	135
Figure 81 Various superimposed Ni 2p spectra for before (red) and after (black) reduction	136
Figure 82 Sn 3d/4 spectra comparison for before (red) and after used (black) for (a) 4D and (b) 6D	138

List of Tables

Table 1 Types of Fuel Cell Systems	13
Table 2 Comparison of fuel cell with other power generating systems [21]	14
Table 3 Advantages of SOFCs.....	20
Table 4 Energy balance from different energy carrier [48]	23
Table 5 Typical Biogas composition	24
Table 6 Acetonic degradation [48].....	26
Table 7 Methanogenic conversion [48]	27
Table 8 Gas phase reactions on CO ₂ reforming of methane [96]	45
Table 9 Proposed reactions on Sn/Ni during calcination, reduction and alloying [136]	58
Table 10 List of Materials	63
Table 11 XRF composition results on various types of fuel cells (representative for the 95% confidence interval)	83
Table 12 The depth of the XRF scan results for each element	83
Table 13 Typical base weight for each type of fuel cell, before and after doping	89
Table 14 Potentiostatic average measurements between UD, 4D, and 6D samples	102
Table 15 Undoped cell typical chemical contents for 500x magnification areas	110
Table 16 Various BSE images on anode surface with 500x magnification and 15 kV	112
Table 17 4D cell chemical compositions of anode surface for 500x magnification areas.....	115
Table 18 6D cell chemical compositions of anode surface for 500x magnification area	115
Table 19 Comparison of elements concentration before reduction.....	116
Table 20 Comparison of analysed layer for the elements before reduction.....	116
Table 21 BR samples average atomic % based on wide scan spectra peak intensities.....	123
Table 22 Sn 3d binding energy lists [145]	125
Table 23 Zr 3d/7 and Y 3d/8 comparison analysis with database spectrum from [144].....	126

Table 24 4D chemical composition for after reduction on anode surface at 500x magnification area	128
Table 25 6D chemical composition for after reduction on anode surface at 500x magnification area	128
Table 26 Comparison of elements concentration after reduction	129
Table 27 Comparison of analysed layer for the elements before reduction.....	130
Table 28 Comparison of element concentrations before and after reduction (in wt%)	130
Table 29 XPS average atomic concentration for each elements spectrum in AR samples	137
Table 30 Zr and Y spectra comparison for 4D and 6D	139

Abbreviations

AD	Anno Domini
AFC	Alkaline Fuel Cell
AFL	Anode Functional Layer
AS	Anode Supported
ASC	Anode Supported Cell
ATR	Auto Thermal Reforming
BC	Before Christ
BSE	Back Scattered Electron
CFC	Catalytic Filamentous Carbon
CHP	Combined Heat And Power
EDX	Energy Dispersive X-Ray Spectroscopy
EIS	Electrochemical Impedance Spectroscopy
EMF	Electromotive Force
FC	Full Cell
FCM	Fuel Cell Model
FCEV	Fuel Cell Electric Vehicle
GC	Gas Chromatography
GDP	Gross Domestic Product
GHG	Greenhouse Gas
HC	Half Cell
IEA	International Energy Agency
IFC	International Fuel Cell
LSCF	Lanthanum Strontium Cobalt Ferrite
LSM	Lanthanum Strontium Manganite
LTFC	Low Temperature Fuel Cell
MCFC	Molten Carbonate Fuel Cell
MJ	Mega Joule
MS	Mass Spectroscopy
Mtoe	Mega Ton Electricity
NASA	National Aeronautics and Space Administration

NEDO	New Energy and Industrial Technology Development Organisation
NiYSZ	Nickel-Yttria Stabilised Zirconia
NO _x	Nitrogen Oxides
OCV	Open Circuit Voltage
OPEC	Organisation of the Petroleum Exporting Countries
PAFC	Phosphoric Acid Fuel Cell
PEFC	Polymer Electrolyte Fuel Cell
ppb	Part per billion
ppm	Part per million
RNG	Renewable Natural Gas
SE	Secondary Electron
SECA	Solid-State Energy Conversion Alliance
SEM	Scanning Electron Microscopy
SMIC	Study of Man's Impact on Climate
SMR	Steam Methane Reforming
SOFC	Solid Oxide Fuel Cell
SOFC-GT	Solid Oxide Fuel Cell – Gas Turbine
SotA	State-of-the-Art
SO _x	Sulphur Oxides
SRK	Suave-Redlich-Kwong
TEC	Thermal Expansion Coefficient
TEM	Transmission Electron Microscopy
TGA	Thermal Gravimetric Analysis
TPB	Triple Phase Boundary
WGS	Water-Gas-Shift
WtE	Waste-to-Energy
XPS	X-Ray Photoelectron Spectroscopy
XRD	X-Ray Diffraction
XRF	X-Ray Fluorescence
YSZ	Yttria Stabilised Zirconia

Chapter 1 Introduction

1.1 Overview

Global concern and awareness of the impacts of using fossil fuels rose in the 20th century along with the impact on the environment. The perturbations in seasons, rising sea-level, higher global temperature are some of the discernible consequences of the global climate change. This is the result of the greenhouse gas (GHG) effect mainly due to human-induced changes in the atmosphere through carbon emissions [1]. Reducing the global impact of carbon emissions, shown in Figure 1 and Figure 2, from conventional fuels has been one of the most important issues in recent years for converting energy.

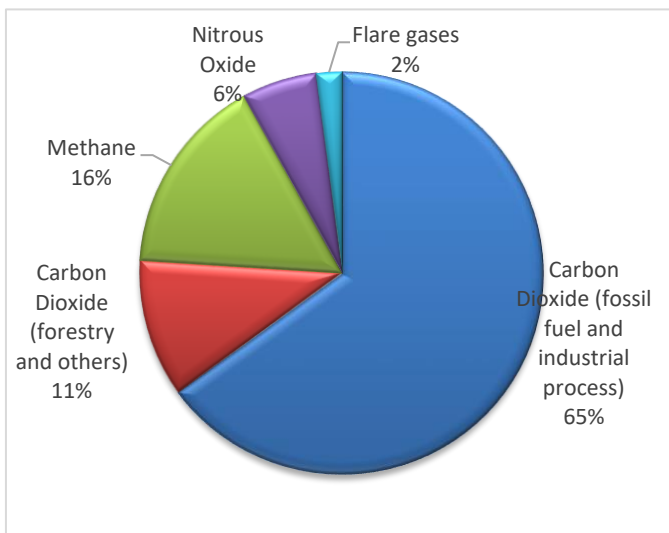


Figure 1 Global greenhouse gas emissions by gas [2]

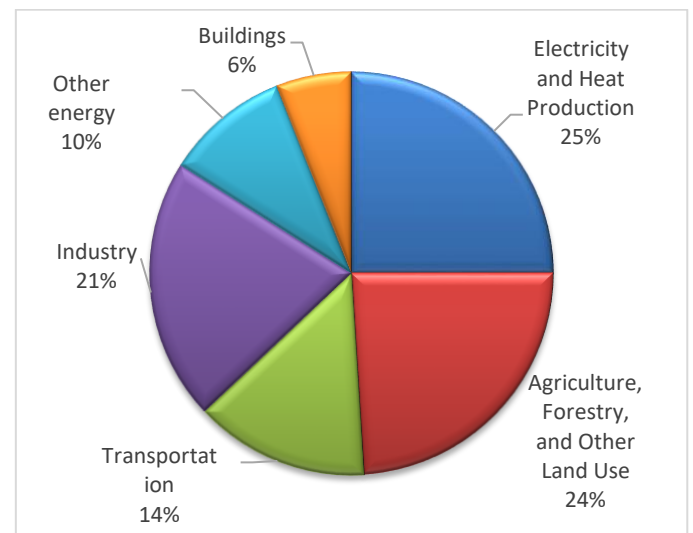


Figure 2 Global greenhouse gas emissions by economic sector [2]

According to the International Energy Agency in their 2016 report [3], fossil fuels including oil, coal, and natural gas in 2014 have reached 66.4% of the total world energy consumption of 9425 Mtoe. This number has been reduced by 10% from 1973 where they reached 75.8% the total world energy consumption. However, the total amount of energy produced back in 1973 was 4661 Mtoe [3], half of the energy production in 2014. The data suggests that there has been a considerable increase in the total energy production and consumption. The impact of the expanding energy supply and demand is the increasing amount of carbon

dioxide and other greenhouse gases to further worsen the global climate change impact (Figure 3).

The attempts to study global climate change have been ongoing since the 1970s. 42 papers in the 1970s showed evidence of the change in climate towards an increase in earth temperature [4] thus leading the global policy-makers and stakeholders to take action. Research focusing on climate change was deemed crucial after a 1971 Stockholm meeting – a “Study of Man’s Impact on Climate” (SMIC) showed agreement for more extensive reports and the need for more knowledge about global climate change and its impacts. It is believed that carbon dioxide released will lead to faster global warming. This result is currently forcing the change from fossil energy to more environmentally friendly energy development.

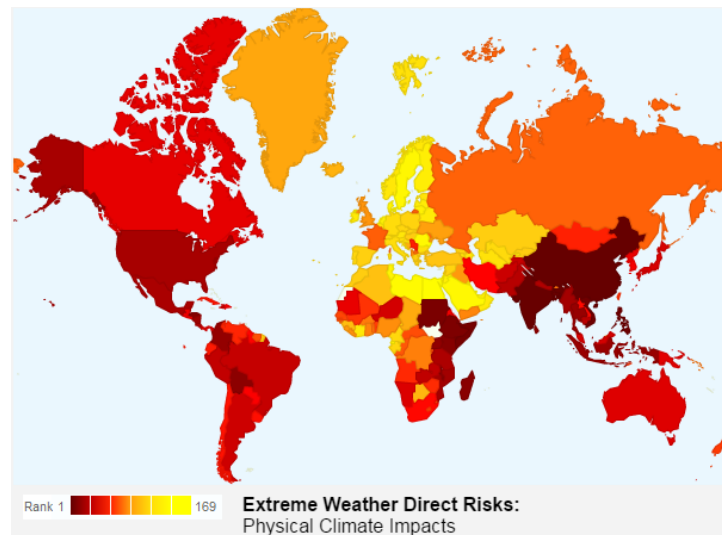


Figure 3 World rankings of four climates impacts based on extreme weather, sea level rise, agricultural productivity loss and overall effects¹

Historical evidence suggests that environmentally friendly energy development has been known since 200 BC in Europe where flowing water energy was used to power mills. Europe has always had a massive potential of harnessing water as energy resource with a lot

¹ <http://www.cgdev.org/page/mapping-impacts-climate-change> [accessed on 07 August 2016]

of areas suitable and beneficial with vertical waterwheels [5]. There is evidence that Persians built the first windmills as energy source by the tenth century AD [6]. Wind power has been used for sailing ships across the oceans in the earlier centuries. The usage of renewable energy for larger purposes began in the 1590s when windmills reached the most efficient and biggest sizes built by the Dutch engineers [7]. William Nicholson and Sir Anthony Carlisle, English scientists, discovered the electrolysis process in 1800 and started the century of early fuel cells. The 19th century was also the time when solar power systems were invented by Augustine Mouchot because of the possibility of fossil fuels running out [8]. In 1870, petroleum began its monopoly of the primary fuel in the world and the development of renewable energy stagnated. Since then the research for oil increased exponentially until the oil crisis hit the world.

The oil crisis in 1970s led various developed countries starting from the United States [9], Germany [9,10], the Netherlands [10] and Sweden [11] to change their focus from non-renewable to renewable and clean alternative energy [12]. Another reason for major countries changing to more environmentally clean energy was the Kyoto Protocol 1997 whose objectives focused on decreasing the rate of global warming. Developed countries started their pathway towards a carbon-constrained environment after the meeting, yet many problems still persist with developing countries.

Developing countries are widely known as the largest contributors towards global carbon emissions. These countries still need to rely on fossil fuel to provide energy because it is the cheapest and most reliable energy source available. Developing countries need massive investment to start their transition towards cleaner technology which oftentimes they cannot afford. As developing countries tried to grow their economic sector, their carbon emissions would also increase. Higher Gross Domestic Product (GDP) also brings higher demand for

energy directly proportional to the total population. Another problem of developing countries is the increasing population.

Rapid growth of global population also brings several impacts and concerns towards the future. First, it will spur global economic growth which will lead directly to additional energy demand. The International Energy Agency (IEA) reported their projection of 1.8 billion tonne oil equivalents in 2035, growing 1.5 times from 2009 demand [13]. Secondly, with human population on the exponential rise compared to the 19th century, global demand of electric energy becomes a major problem. Low tolerance towards traditional forms of energy from centralized fossil fuels due to hazardous emissions (NO_x and SO_x) offers the opportunity for other types of clean alternative energy that can provide 24/7 power. Thirdly, the global transportation system still uses petroleum as main fuel which needs to be replaced by environmentally more sustainable fuels. Fuel cells offer the possibility of clean alternative energy technology to address all of these global problems.

The fuel cell ideas and simple technology were invented in the early 19th century. This technology offers the possibility to convert chemical energy directly into electricity and heat with nearly zero emissions. Fuel cells have the upper hand towards other sustainable energy technologies because of their relatively high efficiencies and adaptation to use various fuels. Yet, in the early nineteenth century, fuel cells were still in the early stages of development. Materials sciences were not sufficiently developed and the catalyst needed was expensive.

The progress of fuel cell research to provide continuous clean alternative energy to promote the advancement of zero carbon emissions in the world is essential. Fuel cell systems are believed to be one of the answers for energy problems in both developed and developing countries because of the myriad possibilities of fuel sources depending on a country's characteristics and their versatility to be combined with renewable energy. Furthermore, fuel

cells are a viable contender for carbon-constrained vehicles worldwide and powerful auxiliary power units, for instance in jet aircraft. Fuel cells can potentially be used either for single power generation or in hybrid systems with renewable energy for example with wind and photovoltaic energy technologies.

However, before the full usage of fuel cells for a future hydrogen world can be achieved, researchers and scientists still need to overcome various problems. The Solid Oxide Fuel Cell (SOFC) is a high potential fuel cell for power generation, transportation, or for combination with renewable energy thus making this fuel cell a prominent option to study. Yet, the State-of-the-Art (SotA) SOFC right now still has a way to go before reaching a steady commercialisation phase for instance by introducing new material technologies to reach better performance and results.

Various problems with SOFCs that still need to be addressed include but are not limited to the electrode, the interconnection, and the catalysts. The problem with current Cr-based metallic interconnection on SOFCs is about maintaining the conductivity and reducing the resistivity of the protective film (Cr_2O_3) formed on the stainless-steel surface. Materials selection for SOFCs encounters various developments beyond the current SotA to obtain better stability, affordability and sustainability. Monometallic catalysts such as Ni give a good performance as they are stable at high temperature, relatively cheap, and abundant in the world yet cause various problems with carbon formation over time and being easily poisoned by sulphur, which is frequently found in biogas.

This study will observe one of the problems regarding the anode-supported SOFC. The main idea is to put a promoter into a monometallic nickel catalyst in a nickel/yttria-stabilized-zirconia (Ni/YSZ) cermet anode supported cell in dry reforming mode with biogas as fuel. Tin (Sn) is selected to be the promoter following a previous study in our

group. This study will focus on the analytical observations of the microstructure of Sn inside the modified cells and the performance comparison with standard cells without promoter.

1.2 Clean Alternative Energy

Clean alternatives using hydrogen as main fuel and renewable energy are the focus of the hydrogen economy movement towards a zero-carbon emissions world. Finite reserves of fossil fuel and the global climate change force the world to move from carbon-intensive fuel to carbon-restrained fuel. Hydrogen needs to be mass-produced [14–18] in effective and efficient ways as the primary fuel for fuel cells and internal combustion engines [17] due to its future role as clean energy vector [18]. Hydrogen production technology uses various methods such as steam methane reforming, dry reforming, auto-thermal reforming, electrolysis, thermochemical electrolysis, photochemical electrolysis, and biomass conversion (pyrolysis, gasification, fermentation, anaerobic digestion and bio-photolysis) [19].

Commonly mistaken as the same concept, clean alternative energy is not interchangeable with renewable energy. While renewable energy resources come from nature and could be potentially used without change to the energy balance at large, clean alternative energy is a form of energy that might or might not come from renewable resources but produces cleaner energy overall. The clean alternative energy sources² also include natural gas, ‘clean coal’ (through carbon capture and sequestration processes), and nuclear as part of their clean alternative energy examples.

² <https://cleantechnica.com/clean-energy/> [accessed on 08 August 2016]

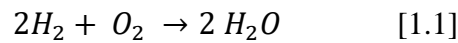
Natural gas has been considered as clean alternative energy for the last few decades. According to the U.S Department of Energy Alternative Fuel Data Center³, there are two production methods of natural gas which consists mainly of methane (CH₄). The first one is the fossil fuel gas as the result of organic matter trapped for millions of years under heat and pressure that need to be extracted from a well, often together with crude oil extractions. This natural gas needs to be processed through pre-treatment before use. The second is the renewable natural gas or biomethane, produced from organic material through the anaerobic digestion process. The organic materials coming from landfills and livestock produce renewable natural gas (RNG). Fuel cells fall into the clean alternative energy categories. SOFCs can use natural gas as fuel and have the possibility to forego the gas pre-treatment unit but still produce CO₂. However, carbon dioxide can help the reaction inside an SOFC to some extent. SOFCs can be used with natural gas or coal gasification process gas (syn-gas) to offer lower emissions. SOFCs can be used for power generation, including hybridisation with Gas Turbines (SOFC-GT), or for replacing boilers for housing (micro-CHP).

The challenges for clean alternative energy lie in their source of fuels, disparate opinions about the emissions to the environment, and their potential threats towards sustainability. Some concepts for clean alternative energy still consider using coal gasification or natural gas which count as non-renewable sources. The other option is using nuclear energy as it would yield massive energy and lack of CO₂ emissions but with high concerns about safety, maintenance, and waste management. The best approach for the energy issue globally is to do exhaustive research on every renewable technology and search for more alternative energy with gradually less usage of fossil fuel.

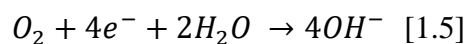
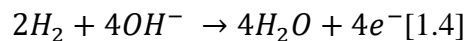
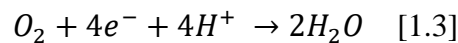
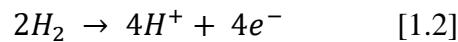
³ http://www.afdc.energy.gov/fuels/natural_gas_basics.html [accessed on 08 August 2016]

1.3 Fuel Cells

Fuel cells are not a new technology in the world of clean alternative energy based on hydrogen. The available evidence suggests that the first experiment of a fuel cell was conducted by William Grove in 1839 [20]. Grove used the reverse experiment of electrolysis of water and found that a small electric current was produced. An alternative looks on the Grove fuel cell experiment is to think hydrogen as the fuel being combusted in reaction 1.1.



Further observations on each electrode give better understanding for the reaction between hydrogen and oxygen that produces electric current as shown in reaction 1.2 to 1.5.



Reaction 1.2 and 1.3 are the reactions for acid electrolyte fuel cells, meanwhile reactions 1.4 and 1.5 are valid for alkaline electrolyte fuel cells. Different from other electrochemical devices, fuel cells have the anode as the electrode from which electrons are produced and flow, meanwhile the cathode is the electrode that receives the electrons. Thus, this makes the cathode the positive electric terminal and the anode the negative one. The reaction for each electrode as presented in reaction 1.2 through 1.5 gives clear indication that in a continuous fuel cell system, electrons produced at the anode must flow through an “outside” electric circuit and the ions (H^+ for acid electrolyte and OH^- for alkaline electrolyte) must

pass through the electrolyte [20]. If the electrons pass through the electrolyte, there will be no electric current generated in the system.

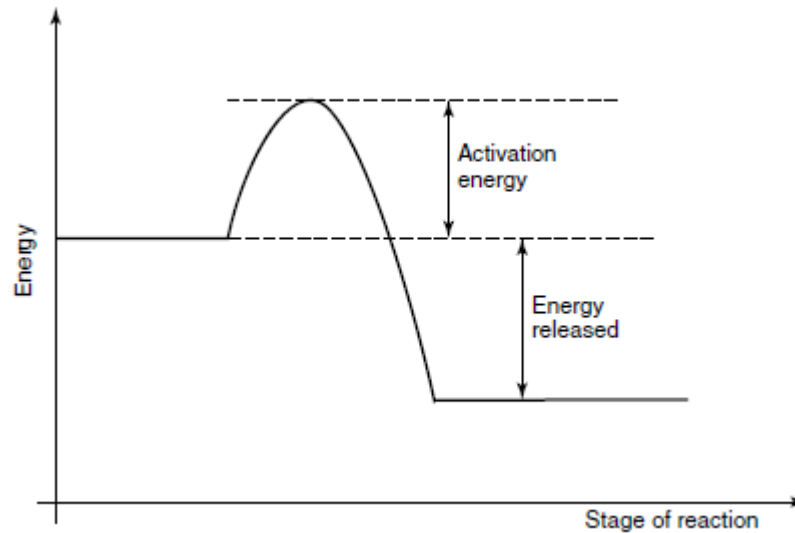


Figure 4 Standard activation energy diagram for an exothermic reaction [20]

The former reactions also indicate that in a fuel cell system, there are at least four main parts to produce electricity using hydrogen as fuel: anode, cathode, electrolyte and external circuit. In general fuel cell concepts, energy is released in the anode. However, there are some limitations that relate closely with the fuel cell materials and kinetic performance. The anode side is limited because there is an activation energy barrier to pass through before the reaction occurs (Figure 4). The activation energy relates to the low reaction rate which can be surmounted by operating in high temperature conditions, using a catalyst, or increasing the electrode area [20].

In theory, the energy release in a fuel cell can be explained using the Gibbs free energy concept. The change in Gibbs free energy is the energy release by a fuel cell due to differences in Gibbs free energy of the product and the reactants.

$$\Delta G_f = G_f \text{ of products} - G_f \text{ of reactants}$$

The Gibbs free energy can be used to calculate the output voltage (electrical work) of an ideal fuel cell. The electrical work equals the product of the charge and voltage, then if $-e$ is one electron charge and there are two electrons that flow in a fuel cell per mole of H_2 fuel with a total charge as follows, where N is Avogadro's number of 6.022×10^{23} and F being the Faraday constant of 96,485.

$$-2Ne = -2F$$

The Gibbs free energy released (ΔG_r) in a reversible fuel cell system is

$$W = \Delta G_r = \text{charge} \times \text{voltage} = -2FE_o$$

Thus, the electromotive force (EMF) or reversible open circuit voltage of a fuel cell is

$$E_o = \frac{-\Delta G_r}{2F}$$

For a stationary open system with mass flow across its boundaries (control volume) and using the 1st Law of Thermodynamics (i.e the kinetic and potential energies are constant in time), then the enthalpy can be defined as the difference between the heat Q and the work W involved in a system (fuel cell case)

$$\Delta H = \Delta Q - \Delta W$$

If the change in enthalpy and Gibbs free energy is negative, heat is liberated, and the reaction occurs spontaneously. Hydrogen is being ionised in the anode and the change in enthalpy ΔH is zero while in the cathode where the oxygen reacts with the electrons, ΔH is -285.5 kJ. Hence, in a typical fuel cell, 285 kJ/mol are converted into heat (Q) and electricity (W). In addition, a thermodynamic fuel cell reaction uses entropy to indicate the energy

“quality”. In a reversible isothermal process involving heat transfer Q_{rev} at a temperature T_0 , the entropy is defined as

$$\Delta S = \frac{Q_{rev}}{T_0}$$

The “equal” sign (=) defines the minimum amount of heat Q_{min} required in the process.

Thus, the maximum efficiency for a fuel cell is

$$\eta_{max} = \frac{W}{\Delta H} = 1 - \frac{Q_{min}}{\Delta H}$$

The definition of entropy is related to the 2nd Law of Thermodynamics. One interpretation of the law is that it is impossible to convert all the energy related with irreversible processes, such as heat and chemical energy, into work. Hence, in a fuel cell system, the Gibbs Free Energy can be used to represent the reversible part of the energy. Then, the maximum possible energy conversion efficiency in a fuel cell is

$$\eta_{max} = \frac{\Delta G}{\Delta H}$$

Fuel cells are differentiated in terms of electrolyte and mobile ions. Various types of fuel cell were found after Grove’s experiments (with an Alkaline Fuel Cell, AFC) such as Solid Oxide Fuel Cells (SOFCs), Polymer Electrolyte Fuel Cells (PEFCs), Molten Carbonate Fuel Cells (MCFC), and Phosphoric Acid Fuel Cells (PAFCs). Low temperature fuel cells (AFC, PEFC, PAFC) are employed for portable and vehicles applications. Meanwhile, the high temperature fuel cells (MCFC, SOFC) are mainly considered for large-scale power generation and stationary applications (shown in Table 1).

Table 1 Types of Fuel Cell Systems

	Alkaline Fuel Cells (AFC)	Phosphoric Acid Fuel Cells (PAFC)	Polymer Electrolyte Fuel Cells (PEFC)	Solid Oxide Fuel Cells (SOFC)	Molten Carbonate Fuel Cells (MCFC)
	Low Temperature			High Temperature	
Electrolyte	Alkaline	Phosphoric acid	Polymer	Ceramic	Molten Carbonate
Temperature	80-200°C	200°C	80-120°C	700-1000°C	650°C
Fuel	H ₂	H ₂	H ₂	H ₂ /CO/CH ₄	H ₂ /CO/CH ₄
Oxidant	O ₂ /Air	O ₂ /Air	O ₂ /Air	O ₂ /Air	O ₂ /Air + CO ₂
Mobile Ion	OH ⁻	H ⁺	H ⁺	O ²⁻	CO ₃ ²⁻
Efficiency	50-60%	40-45%	40-45%	50-55%	50-55%
Applications	Space vehicles (Apollo, Space Shuttle)	Large numbers of 200 kW CHP systems	Vehicles & mobile apps, lower power CHP system	Suitable for all sizes of CHP systems 2kW to multi MW	Suitable for medium to large scale CHP systems

National Aeronautics and Space Administration (NASA) used the AFC type developed by International Fuel Cell (IFC, later UTC Power)⁴ in the early 1960s for on-board electric power in space missions. PEFC have been used for fuel cell electric vehicles (FCEV) since the 1970s, around the same time as the oil crisis and Organisation of the Petroleum Exporting Countries (OPEC) embargoes. Major car companies were starting to research and develop FCEV in the same decade and focusing on hydrogen as fuel for the fuel cell vehicles as it generates zero emissions. The 1980s was the time when fuel cells were used for stationary and transport applications with PAFC development becoming the main active area. Nowadays, fuel cells have been researched and developed to further substantiate the global hydrogen economy.

⁴ <http://www.fuelcelltoday.com/history#The Space Programme> [accessed on 12 July 2016]

Table 2 Comparison of fuel cell with other power generating systems [21]

	Reciprocating Engine Diesel	Turbine Generator	Photovoltaic	Wind Turbine	Fuel Cells
Capacity Range	500 kW–50 MW	500 kW– 400MW	1 kW – 100 MW	10 kW – 7 MW	200 kW – 4 MW
Efficiency	35%	29-42%	-*	-*	40-75%
Capital cost (\$/kW)	200-350	450-870	1000	< 1000	1500-8000
O&M (\$/kW)	0.005-0.015	0.005-0.0065	0.001-0.004	0.01	0.0019-0.0153

* No fuel input

Latest progress in fuel cell technology systems includes the ideas of multifunctional fuel cell systems and the hybridisation of fuel cells with other types of renewable energy. The basic idea of a multifunctional fuel cell system is to fully utilise all the fuel cell output whether it is the main product or any by-products (heat, steam, CO₂, H₂, amongst others). These attempts have been applied to Combined Heat and Power (CHP) applications [22–24], residential micro-CHP [25], and integration into aircraft systems [26].

1.4 Solid Oxide Fuel Cell

The Solid Oxide Fuel Cell (SOFC) is one type of high temperature fuel cell that can be employed for both portable and stationary applications. This branch of fuel cells has been an active area of research because of its prospect of megawatt electricity production from a single system. SOFC is not a novel type of fuel cell but the long-term research efforts on this type alone show its potential for future energy supply. Like any other high temperature types of fuel cells, SOFC can also be considered as part of an integrated fuel processing and heat generating system [20].

SOFCs have emerged as the most promising type of fuel cell due to their characteristics ever since their discovery in 1937 by Swiss Scientists Emil Baur and H. Preis [27]. These two scientists successfully developed a first SOFC based on earlier work by Walther Nernst in

which a combination of zirconium and yttrium oxides acted as the electrolyte. However, it was not until the National Aeronautics and Space Administration (NASA) used fuel cells for space flight that people became aware of them as one potential power source [28].

SOFCs are a solid-state device and are made of ceramics with a mostly nickel based anode layer. One cell comprises of three main parts; anode, electrolyte, and cathode. SOFCs can be divided based on the supported layer in the cell. Thus, there are electrode-supported (anode- & cathode-supported), electrolyte-supported and metal or interconnect supported SOFCs. The supporting layer is mostly the thickest part of either one of anode, electrolyte, or cathode.

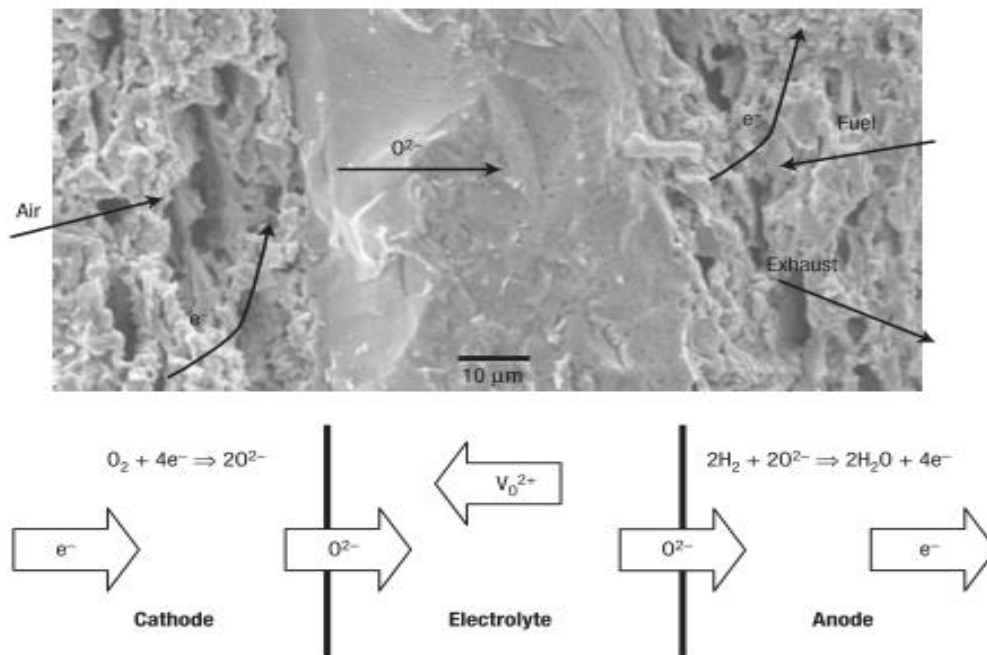


Figure 5 SEM cross section of SOFC and the reaction that occurs [29]

Other than with the “typical” fuel cell reactions like in PEFCs reaction, SOFCs has the oxygen disassociated and converted into oxygen ions at the cathode which then migrate through the electrolyte [30]. The anode side on SOFCs is the place of electrochemical

reaction. If the SOFC system uses the internal reforming reactions, the anode side also acts as the reformer for the system.

Another important feature of SOFCs is their dependency in the cell stack design and cell configuration towards their performance. Figure 6 shows the typical cell configuration type on SOFCs: (a) electrolyte-supported cell 50 μm anode layer, 200 μm electrolyte layer, and 50 μm cathode layer [31]; (b) anode-supported cell with $\sim 0.5\text{-}1.0$ mm anode layer, $\sim 10\text{-}20$ μm electrolyte layer, and $\sim 35\text{-}50$ μm cathode layer [32]; and (c) cathode-supported cell with 50 μm anode layer, 20 μm electrolyte layer, and 500 μm cathode layer [33].

Different design and configurations lead to different performances. Planar-type SOFCs with higher power density and shorter current path regularly produce higher performance than tubular-type SOFCs [34]. Different gas flow configuration, different design of current collectors, and cell-to-cell electrical connection also offer a range of possibilities.

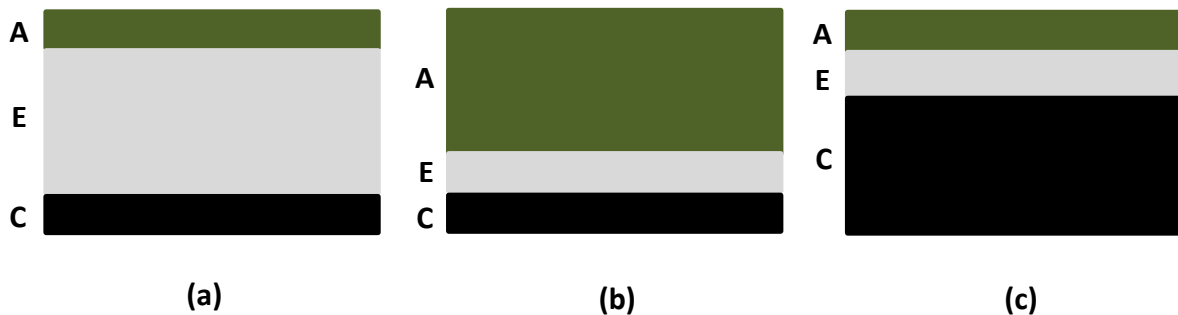


Figure 6 SOFC single cell configuration: (a) electrolyte-supported, (b) anode-supported, (c) cathode-supported [A=Anode layer, E=Electrolyte layer, C=Cathode Layer] *figures not drawn to scale

Nowadays, anode supported SOFCs are deemed as the best design option since this concept provides more mechanical strength for the cell and offers advantages with low electrolyte ohmic losses [33]. Another reason is the catalytic activity in the anode area. Anode supported SOFCs can be further divided into two types: the first one is the type that contains only an anode support layer, and the second one is the type which contains an anode support with anode functional layer. Electrolyte-supported cells need higher temperature operating

conditions to accommodate the ohmic loss from the thick electrolyte [35,36]. The high temperature requirement leads to a limited choice of materials and higher fabrication cost. Thus, electrode-supported cells are much preferred over electrolyte-supported SOFCs. Further investigation on electrode-supported SOFCs shows that cathode-supported SOFCs are harder to fabricate compared to the anode-supported type [33].

SOFCs also offer the advantage to use the waste heat from high temperature operation for fuel reforming, provide additional heat for other uses, and drive turbines in integrated hybrid systems. Aside from that, SOFCs can use gas fuel from various sources, not necessarily needing hydrogen in high purity as with low temperature fuel cells. SOFCs can operate using the internal reforming reaction which is the cause of its characteristic fuel flexibility. Indirect reforming can also be applied for reducing the reforming load on the anode side of the SOFCs. If SOFCs use biogas as fuel, they operate carbon-neutral.

SOFCs have the possibility to operate in internal reforming conditions with a nickel based ceramic compound as their core cell element. Both steam and dry reforming can be used in SOFC operations. The advantage of the SOFC capability to perform under internal reforming is attractive for development of stationary energy generator fuel cells. SOFCs get the benefit compared to low temperature fuel cells (LTFC) because they involve only solid and gas phases, much simpler technology than LTFC. From the mechanical point of view, SOFCs have many advantages such as high flexibility in manufacturing, shapes and sizes. SOFCs can use different materials and be operated at various operating temperatures, ranging from 650° to 850°C [20]. In several cases, it is even considered to increase the range up to 1000°C with shorter lifetime from faster degradation of SOFC component [37]. One major problem with SOFCs in internal reforming conditions is rapid carbon formation on their catalysts, usually in the form of nickel-cermet. Thus, in order to address the

problem of carbon formation in nickel anode cermets, a new nickel alloy-based catalyst is introduced in this study.

SOFC efficiency yields higher energy conversion compared to conventional heat engines and other fuel cells system [38]. Nowadays, typical SOFCs in the market show conversion up to 60% net efficiency [39]. An SOFC CHP system integrated into an office building for Charlotte and Minneapolis (United States of America) has lowered their annual utility costs up to 14.5% with a 175 kW-sized SOFC. The reduction in annual utility costs also comes with around 60% reduction in CO₂ emissions from the integrated SOFC CHP system [40]. This development aligns with the Copenhagen Accord and the results of the United Nations Climate Change Conference 2009 to reduce energy-related emissions for stabilizing greenhouse gases in the atmosphere by 2020 [40,41]. Further development in SOFCs must comply with the 2015 United Nations Climate Change Conference, Conference of Parties 21 (COP21) in Paris agreements on climate act to keep the 2°C global warming threshold in check⁵.

⁵ <http://www.cop21paris.org/about/cop21> [accessed on 21 August 2017]

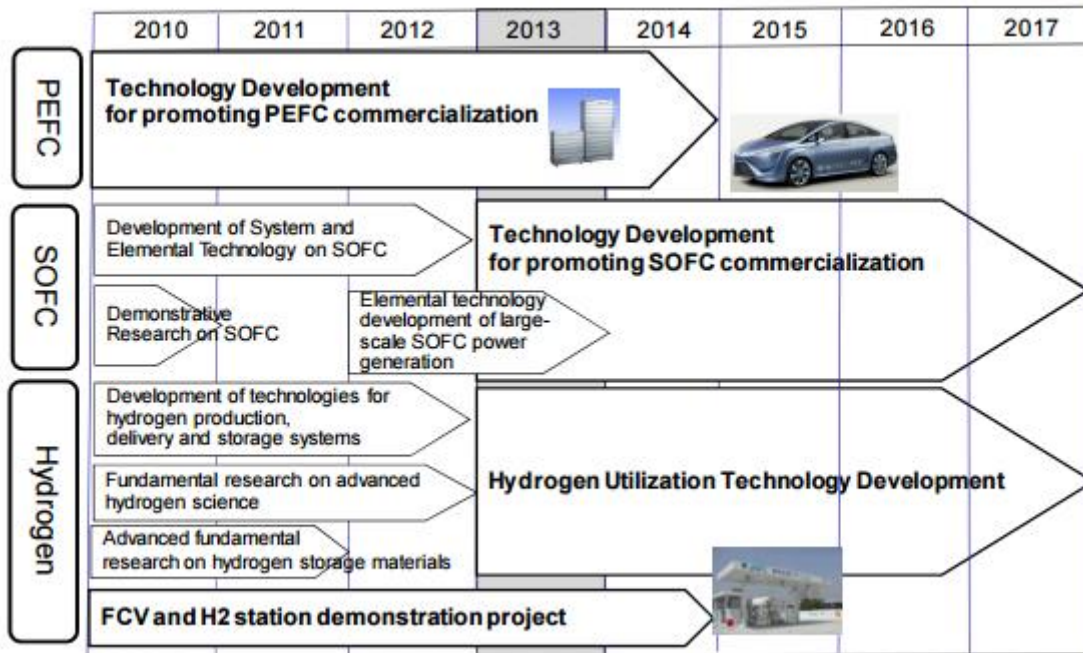


Figure 7 Japan schematic diagram for Fuel Cell development [42]

The Japanese New Energy and Industrial Technology Development Organisation (NEDO) has identified the SOFC as a promising technology for carbon dioxide reduction. Japan has been working on the project of “Technology development for promoting SOFC commercialization” (2013-2017) after finishing the first project of “Development of system and elemental technologies on SOFC” (2008-2012) [42]. The purpose of the NEDO projects follows the plan as shown in Figure 7.

NEDO has achieved their goals from the project about the forecast of degradation rate less than 0.25%/1000 hours, equal to 10% in 40,000 hours, and the forecast of 250 start and shut down events. SOFC from the project have been used in the “ENE-FARM type S” project realised by JX Nippon Oil and Energy in 2011 [42]. Japan is on the way to a hydrogen economy with its research projects not only on SOFC but also on fuel cells in general. The Japanese government pushed their fuel cell development with the 120,000 fuel cell

residential units with the ENE-FARM commercialisation project⁶. This has been arguably the most successful SOFC commercialisation project in the world.

On the western hemisphere side, the interest in SOFC as the high potential candidate for the stationary market and large central-power plants has been developed since 1989 [43]. In the United States, under the Solid-State Energy Conversion Alliance (SECA) guidance, there have been three focal areas of SOFC work including cost reduction, coal-based systems, and research and development (R&D)⁷. There have been two fuel cell stacks (around 10 kW each) tests from this project, as a collaboration between Versa Power Systems with FuelCell Energy Inc. for 5000 hours lifetime [43]. Wachsman and Singhal [43] also cited that Siemens Westinghouse stacks had been run for 5000 hours in 2009. Regardless, the target for SOFC development is to have stack lifetime for more than 40000 hours (corresponding to minimum 5 years operation) [44].

Table 3 Advantages of SOFCs

Advantages of SOFCs	
Efficiency	The most efficient in terms of fuel input to electricity output compared to other fuel cell types
Adaptability	The most prominent fuel cells in fuel flexibility
Applications	Suitable for distributed generation markets because of high conversion rate
Manufacture	Has a modular and solid construction with no moving parts; do not contain noble materials thus reducing the problems for high volume manufacture; easy electrolyte management
Byproduct	High quality heat byproduct for other applications (co-generation, combined cycle, etc.)
Emissions	Extremely low emissions with no danger of carbon monoxide or NO _x from the exhaust gases
Lifetime	Has potential for long lifetime and suitable for large power generator plants

⁶ <https://fuelcellsworld.com/archives/2015/09/23/ene-farm-installed-120000-residential-fuel-cell-units/> [accessed on 12 March 2017]

⁷ <https://energy.gov/fe/science-innovation/clean-coal-research/solid-oxide-fuel-cells> [accessed on 21 March 2017]

SOFCs are highly competitive in their potential markets and have the most demanding materials choices compared to other advanced fuel cell commercial developments such as PEFC [45]. Stambouli and Traversa [45] concluded all the advantages of SOFCs in Table 3.

1.5 Biogas as Fuel

As the conventional and non-renewable fuels such as oil, coal and natural gas, are facing unpredictable fluctuation of price and rapid abatement of supplies globally, various efforts to produce and sustain energy for the world are being made. Moreover, this movement is paralleled with concern for the environment thus renewable energy is becoming the trend in the field. ‘Sustainable’ and ‘renewable’ are the main themes for major international conferences and large amounts of money are being invested to advance renewable technology.



Figure 8 Biogas plant for farm scale [<https://www.host.nl/en/biogas-plants/>;
accessed on 22 March 2018]

The idea to use rotting vegetables to produce flammable gases has been used since the ancient Persian [46]. In the 17th century, Van Helmont discovered that decaying organic matter could be used for flammable gases [47]. The same source also stated that the claim was backed by Alessandro Volta in 1776 saying that there is a correlation between decaying organic matter and the flammable gas produced. In 1808, Sir Humphry Davy found that methane was present in the gases from anaerobic digestion of livestock waste [47]. The

earliest digestion plant was built in Bombay, India, in 1859⁸ and the technology was brought to England to fuel street lamps in Exeter [48]. In the 1930s, the research to develop anaerobic bacteria to produce methane was begun. This is the origin of the biogas technology of today.

Biogas stems from biomass that undergoes biochemical transformation and is converted into secondary chemical products [49]. Based on this source, the fermentation process is especially advantageous and in favour of biogas because the energy balance will reach an output to biomass input ratio of 28.8 (MJ/MJ). The energy balance ratio is the highest for biogas compared to other energy sources when considering the energy yield.

Biogas has long become one of the main candidates for future energy supply due to its origin from organic material that has been broken down by bacteria⁹. The production of biogas results in various gases, mainly methane, carbon dioxide, and hydrogen. Composition and impurities content of the biogas highly depend on the feedstock of the biogas production. Biomass with the ratio of C:N within the range of 20-30:1 and a harvesting humidity over 45% is suitable for biogas production [50]. Furthermore, the same study concludes that the product composition would depend on the content of proteins, polysaccharides and lignin, the degree of polymerisation, and cellulose crystallinity.

⁸ www.kingdombio.com/history1.html [accessed on 23 March 2017]

⁹ <http://www.darvill.clara.net/altenerg/biogas.htm> [accessed on 14 February 2017]

Table 4 Energy balance from different energy carrier [49]

Energy Source	Energy Balance	
	Output:input ratio (MJ/MJ)	Remarks
Rapeseed oil	5.7	Energy recovery of the colza cake and green waste included
Ethanol	2.7	From wheat
	1.6	From sugar beet
	5.0	From sorghum
		Energy recovery of the bagasse included
Electricity and heat	8.5	Combustion of the whole plant From cereals
	19.7	Combustion of <i>Miscanthus</i> plants (not dried)
	14.2	Combustion of energy plants
	20.4	Combustion of residual straw
	19.0	Combustion of forest residual wood
Biogas	28.8	From excrement (CHP cycle)

Table 4 shows many raw materials have been considered as substrate for biogas fermentation, including but not limited to: waste water, organic waste from households and food industry, agricultural waste products, landfill for residual waste, and sewage sludge [49].

Table 5 Typical Biogas composition¹⁰

Compound	Formula	Concentration (%)
Methane	CH ₄	50-75
Carbon Dioxide	CO ₂	25-50
Nitrogen	N ₂	0-10
Hydrogen	H ₂	0-5
Hydrogen Sulphide	H ₂ S	0-3
Oxygen	O ₂	0-1
Hydrocarbon	C _x H _y	0-1
Ammonia	NH ₃	0-0.5
Silicone	R ₂ SiO	0-50 mg/m ³

Biogas production is called fermentation because the respective bacteria break down the chemical chain in the absence of oxygen (anaerobic), as the typical biogas composition shown in Table 5. The anaerobic reaction that occurs on wet and green biomasses in a suitable environment (pH, temperature, humidity) can produce gases that can substitute fossil fuels. Biogas can be produced using both liquid and solid wastes from biomass thus making the possibility of Waste-to-Energy (WtE) technology (shown in Figure 9) for massive power generation viable, as one solution for the energy and environmental crisis in the world.

¹⁰ www.e-inst.com/biomass-to-biogas/ [accessed on 21 March 2017]

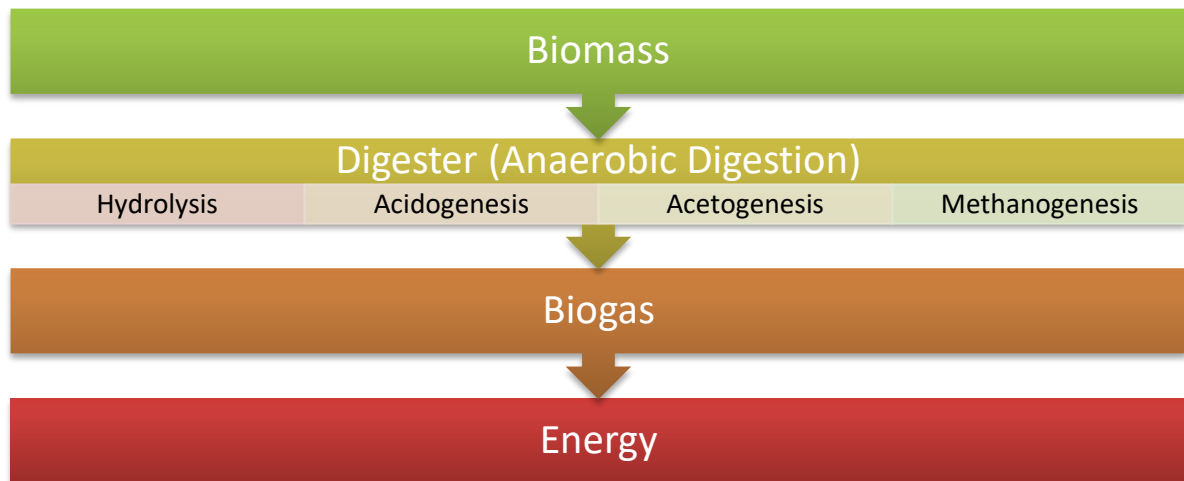


Figure 9 Fundamental steps for anaerobic digestion [www.e-inst.com/biomass-to-biogas/; accessed on 21 March 2017]

The Biological Reaction of Biogas Production

1. HYDROLYSIS

Figure 10 illustrates hydrolysis is the phase when the cellulose, proteins, and fats split into monomers by hydrolase and anaerobic bacteria [49]. According to this source, the process can take place within a few hours for carbohydrates and a few days for proteins and lipids.

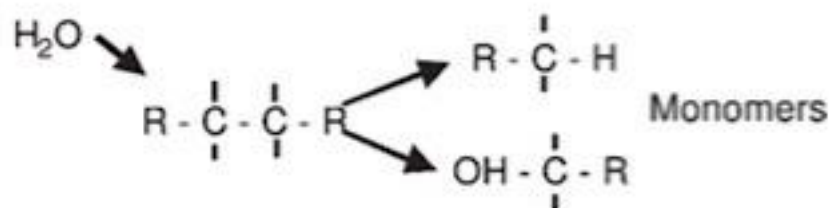


Figure 10 Formation of monomers [49]

2. ACIDOGENESIS

In this stage, the monomers from the first phase will be cut to short-chain organic acids, C1-C5 molecules, alcohols, hydrogen, and carbon dioxide. The amount of hydrogen ions in this intermediate phase will differ by the products to be fermented

as there would be three different degradation pathways for: carbohydrates (via propionic bacteria for succinate and acrylic, via clostridia for butyric acid pathway), fatty acids (from acetobacter via β -oxidation), and amino acids (via Stickland reaction by *Clostridium botulinum*) [49]

3. ACETOGENESIS

The acetogenic phase uses acetogenic bacteria to reduce exergonic hydrogen and carbon dioxide to acetic acid, as listed on Table 6. The bacteria involved in this stage are predominantly responsible for hydrogen production. Acetogenic bacteria need low hydrogen partial pressure for growing and thriving meanwhile for the next stage, methanogenic bacteria need higher hydrogen partial pressure. Both types of bacteria have symbiotic relations to keep the p_{H_2} at an optimum level for the reactions.

Table 6 Acetonic degradation [49]

Substrate	Reaction
Propionic Acid	$CH_3(CH_2)COOH + 2H_2O \rightarrow CH_3COOH + CO_2 + 3H_2$
Butyric Acid	$CH_3(CH_2)_2COO^- + 2H_2O \rightarrow 2CH_3COO^- + H^+ + 2H_2$
Valeric Acid	$CH_3(CH_2)_3COOH + 2H_2O$ $\rightarrow CH_3COO^- + CH_3CH_2COOH + H^+ + 2H_2$
Isovaleric Acid	$(CH_3)_2CHCH_2COO^- + HCO_3^- + H_2O \rightarrow 3CH_3COO^- + H_2 + H^+$
Capronic Acid	$CH_3(CH_2)_4COOH + 4H_2O \rightarrow 3CH_3COO^- + H^+ + 5H_2$
CO ₂ & H ₂	$2CO_2 + 4H_2 \leftrightarrow CH_3COOH + 2H_2O$
Glycerine	$C_3H_8O_3 + H_2O \rightarrow CH_3COOH + 3H_2 + CO_2$
Lactic Acid	$CH_3CHOCOO^- + 2H_2O \rightarrow CH_3COO^- + HCO_3^- + H^+ + 2H_2$
Ethanol	$CH_3(CH_2)OH + H_2O \rightarrow CH_3COOH + 2H_2$

4. METHANOGENESIS

Methanogenesis is the last phase to form methane under complete anaerobic conditions. When the methanogenesis is disturbed, overacidification occurs in the systems listed on Table 7. The disturbance can also occur in the acetogenesis phase (illustrates in Figure 11) with the result of less input to the methanogenesis [49].

Table 7 Methanogenic conversion [49]

Substrate Type	Chemical Reaction	ΔG_f (kJ mol ⁻¹)	Methanogenic Species
CO ₂ -Type	$4H_2 + HCO_3^- + H^+ \rightarrow CH_4 + 3H_2O$	-135.4	All Species
	$CO_2 + 4H_2 \rightarrow CH_4 + 2H_2O$	-131.0	
CO ₂ -Type	$4HCOO^- + H_2O + H^+ \rightarrow CH_4 + 3HCO_3^-$	-130.4	Many Species
Acetate	$CH_3COO^- + H_2O \rightarrow CH_4 + HCO_3^-$	-30.9	Some Species
Methyl Type	$4CH_3OH \rightarrow 3CH_4 + HCO_3^- + H^+ + H_2O$	-314.9	One Species
Methyl Type	$CH_3OH + H_2 \rightarrow CH_4 + H_2O$	-113.0	
Methyl Type (Ethanol)	$2CH_3CH_2OH + CO_2 \rightarrow CH_4 + 2CH_3COOH$	-116.3	

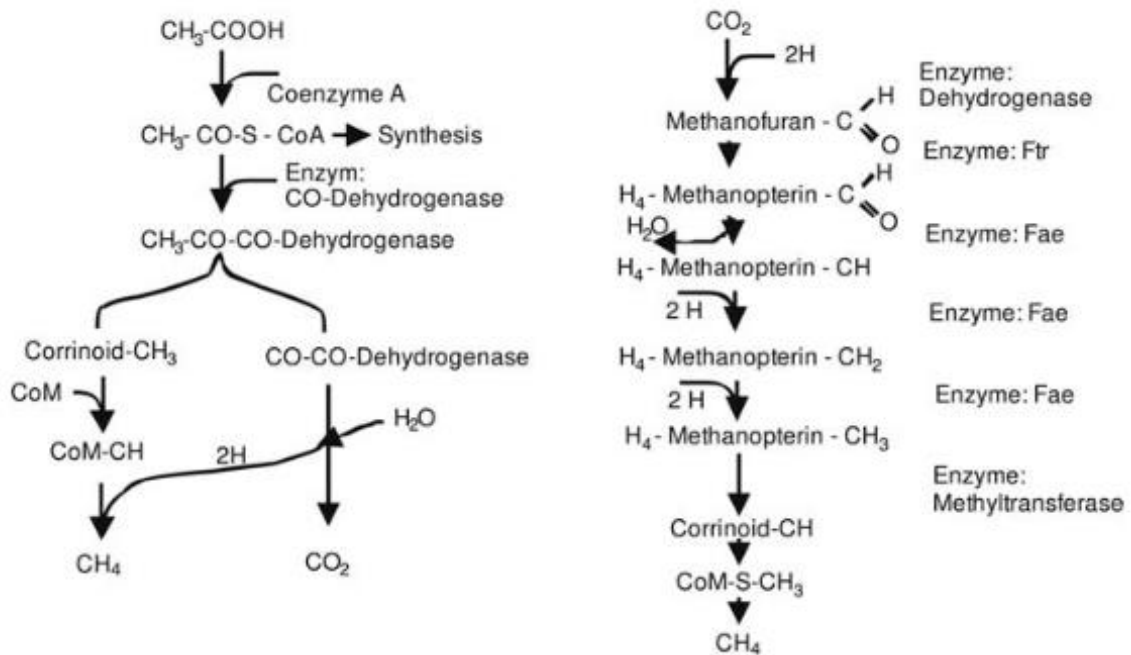


Figure 11 Methane formation from acetate and carbon dioxide [49]

With a high concentration of methane and carbon dioxide, biogas is the perfect candidate for fuelling SOFC systems for internal reforming operation. The entire system would be sustainable and at the same time can be regarded as clean energy. Another advantage from using biogas in SOFC systems is the reduction in capital cost because no pre-reformer is required after desulphurisation. Thus, it is beneficial to further analyse operational SOFCs on biogas to further enhance innovation towards cleaner energy. Biogas will not only bring advantages but also the disadvantages in SOFCs, especially from the carbon formation. Monometallic nickel has been used for hydrocarbon catalyst because of its superiority for hydrocarbon cracking. By using Sn doping on the nickel catalyst in SOFCs system using biogas, it would offer a solution to overcome the carbon formation problems.

1.6 Project Aim and Objectives

This thesis can be divided into several objectives as follows:

- i. To establish understanding of the role of Sn-infiltration for internal reforming using Ni/YSZ cells
- ii. To optimize the pipette drop Sn-infiltration technique for manufacturing Sn-Ni/YSZ
- iii. To evaluate the performance of Sn-doped cells in dry reforming mode

With the above three major objectives, this thesis is outlined into six chapters. The first three chapters serve as introduction chapters which consist of (1) Introduction, (2) Literature review, and (3) Materials and Methods. The results and discussions of the study will be included in the chapter (4) Cell Testing and (5) Cell Characterisation. The conclusions will be on the last chapter of this thesis.

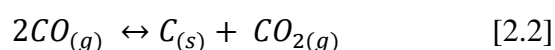
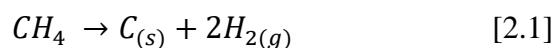
Chapter 2 Literature Review

2.1 Overview

This literature review is presented in several sections; the first section is on the hydrogen production on nickel-based catalysts, its features, merits and drawbacks, and recent research efforts to overcome the challenges including catalyst poisoning and fuel impurities. This is followed by a section on SOFCs with specific focus on elucidating fundamental aspects like thermodynamics, kinetics, electrochemical and catalytic parameters that define the performance of a fuel cell. It discusses the main components of SOFC and the research efforts to search for better alternative anodes to the state-of-the-art Ni/YSZ, including the use of dopants in the anodes. A section on anode supports with addition of dopants for SOFCs will discourse on the ongoing research and development, mainly related to tin as one of the potential elements to give higher resistance to carbon formation and improved performance to SOFCs.

2.2 Hydrogen Production on Nickel-based Catalyst

The nickel catalyst is the most reliable catalyst to support the formation of hydrogen and carbon monoxide via dissociation of methane (shown in reaction 2.1) on the surface of the catalyst [51–53]. Many efforts have been made through the years towards creating hydrogen by catalytic routes on nickel ranging from direct cracking [54,55] to the wide potential of reforming (steam, dry, partial oxidation, auto-thermal, plasma, and aqueous phase) [56]. The research and development in this area is very extensive pursuant to nickel's key role in ammonia and methanol synthesis [57], Fischer-Tropsch catalysis [58] and recently fuel cell systems [59–65].



Reaction 2.1 and 2.2 show hydrogen production via methane cracking and the Boudouard reaction over a nickel catalyst, either monometallic or as an alloy. Reaction 2.1 while giving twice the amount of hydrogen from a single mole of methane, also produces solid carbon. The solid carbon is the primary problem that need to be addressed in SOFC internal reforming reactions.

The hydrogen production using nickel catalysts in many types of oil and chemical industries has spawned the idea of using the same catalyst in fuel cell systems. The projection of using various means of fuels in SOFC can be very profitable if the electrochemical oxidation reaction in the fuel cell can be performed with the same catalysts as the production of hydrogen. It will reduce not only the whole duration of the process but also increase efficiencies.

Nickel has been used as a catalyst since French organic chemist, Paul Sabatier¹¹, and his partner Victor Grignard discovered the addition of hydrogen to molecules of carbon compounds in the hydrogenation reaction using nickel in 1897 [66]. The “Nickel-Effect”, found by Ziegler, Wilke and coworkers, asserted that nickel could catalyse the dimerization of ethylene gas [66]. In 1952, these two breakthroughs led to exhaustive development until the birth of the commercial reforming catalyst (Ni/Al₂O₃-MgO) in the 1970s. Nickel-based catalysts have been known for methanation [67], steam reforming [68], and for further purposes.

Ananikov [69] discussed the key advantages of nickel catalysts including high performance in reactions compared to other metals such as Co [70], Cu [71], and Fe [72]; it has varying degrees of electronic states namely Ni(0)/Ni(I)/Ni(II)/Ni(III) [69,73,74], high versatility to

¹¹ <https://www.britannica.com/biography/Paul-Sabatier-French-chemist> [accessed on 16 March 2017]

new reactions and transformation [69,75], simple activation and transformation of molecules for less reactive chemicals [69], and high flexibility to be combined with other catalyst materials [69,76–78]. Furthermore, nickel is practical to be used as the catalyst on fuel cell systems in accordance with its chemical and mechanical resistance to high temperature [75,76]. Given its properties as a metallic substance, nickel meshes are often used as a contacting element on the anode side, giving both corrosion resistance and mechanical robustness, besides also offering catalytic activity. These meshes typically allow for low pressure drops on the SOFC stack fuel electrode.

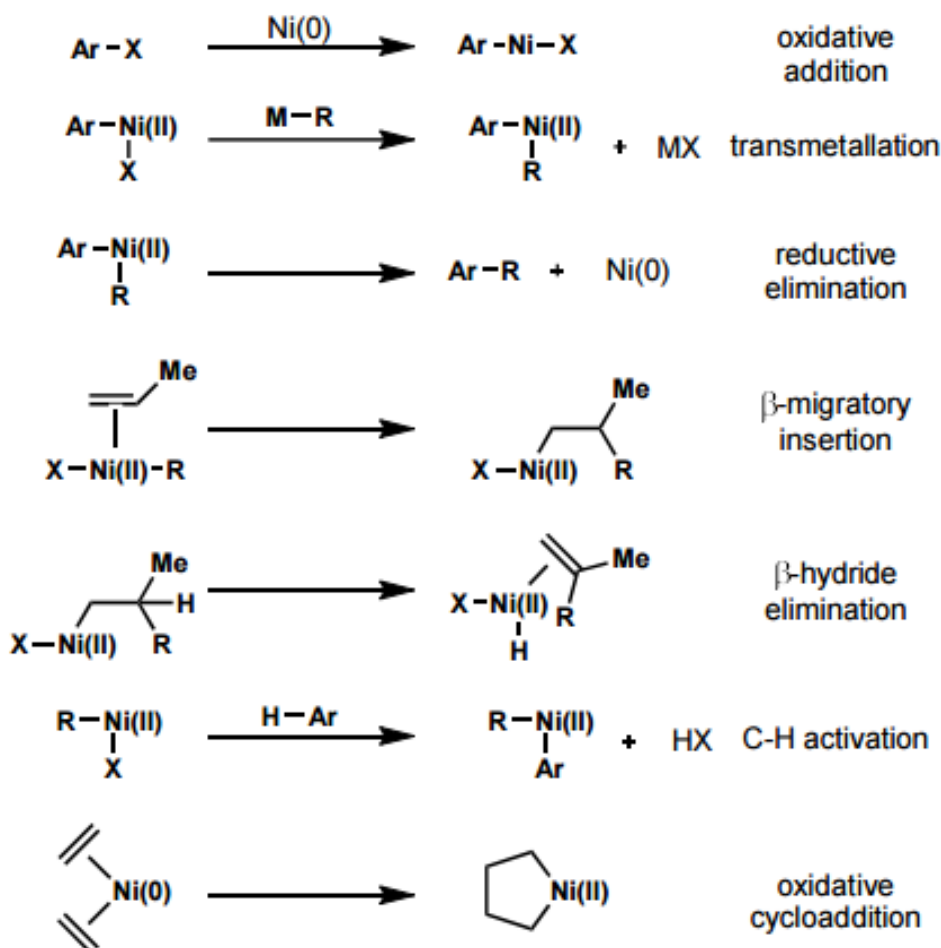


Figure 12 Common nickel catalyst transformation from electropositive d^{10} transition metal [66]

The first problem that arises from the Ni-based catalyst is catalyst poisoning. Nickel-based catalysts encounter problems with chemisorption of sulphur, especially in the steam reforming system [79]. Various reforming methods of fuel cell systems with SotA Ni-based anodes face the challenge of anode degradation due to the reactions with sulphur species [59]. The sulphur content in the fuel could be removed by using desulphurisation as a pre-treatment of the fuel before feeding into the fuel cell system [80]. However, even after prior desulphurisation, the feed still contains sulphur in the range of 0.1-15 ppm [59], which is confirmed dangerous for the cell's performance and electrochemical activity [81]. Another alternative to counter sulphur poisoning is to develop sulphur-tolerant anodes. There are three types of sulphur-tolerant anodes including: thiospinels and metal sulphides, metal cermet, and mixed ionic and electronic conductors [38].

Niakolas [59] takes neutral position on the importance of removing all the sulphur content in the pre-treatment or to invent sulphur-tolerant anodes for fuel cells. There is rapidly growing literature on developing Ni-based sulphur-tolerant anodes. Nickel catalysts with ceria-doping have been proposed as the foremost candidate for addressing the SOFCs with sulphur poisoning [82].

Ni-based catalysts also will readily introduce direct catalytic cracking in hydrocarbon thus producing hydrogen and catalytic filamentous carbon (CFC) [83]. Moreover, Ermakova [83] states that CFC straightforwardly form in enormous amount on metals of the iron group because nickel is used for catalytic decomposition of hydrocarbons. This is also the reason behind nickel reactivity towards hydrocarbon decomposition. Nickel is the most active metal in the iron group and can decompose the most stable hydrocarbon, methane, as opposed to other iron group elements such as cobalt and iron [83]. Methane is the most

prominent content in natural gas and biogas which also acts as the most important fuel for SOFCs in internal reforming.

There are two types of carbon formation found by Lee [84], graphitic carbon as the result of oxidation at high temperature and amorphous carbon at lower temperature oxidation. The production of filamentous carbon from methane decomposition in Ni-based catalysts is inadmissible for SOFC systems. Filamentous carbon is known to fill the pores of the SOFC anode and eventually cover the surface of the active area which will lead to a decrease in performance of the SOFC and eventual destruction of the cells. The increased demand on catalyst efficiency has spurred attention to catalyst deactivation [68]. The perennial problem is, however, the severe deactivation of the nickel catalyst due to carbon fibre formation. Figure 13 shows the pore infiltration of carbon into the anode of an SOFC.

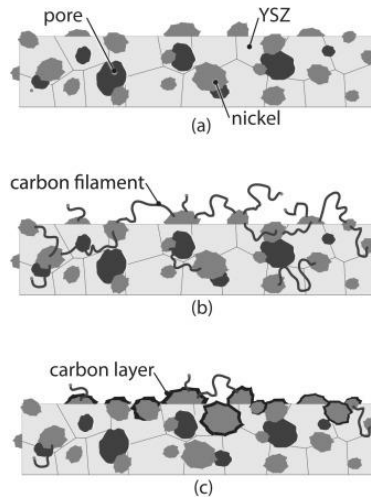


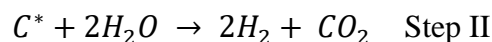
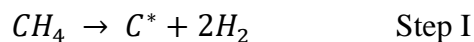
Figure 13 Filamentous carbon spreading inside an anode SOFC [85]

The main drawback of using nickel catalysts in various hydrogen production processes is the formation of carbon whiskers or long carbon-bond wires at certain operating conditions in the wide range of 300°C to 1000° [68,83,86,87]. This filamentous carbon could lead to catalyst degradation [68,87]. The C-C bond formation is undesirable inside the fuel cell

system. The carbon wires act as catalyst poison in the internal reforming as they will cover the active area of the catalyst. Even with addition of MgO to the commercial catalyst, coke formation is only suppressed at steam to carbon ratios above 1.0 [52].

Freni et.al [77] offered an approach to counter the coke formation problem on nickel catalysts for steam reforming with ethanol. In his study, Freni proposes the use of a two-layer fixed bed catalytic reactor using two different kinds of catalysts, namely, Cu/SiO₂ and Ni/MgO. The reason for carbon formation during ethanol steam reforming might be ethanol dehydration [77]. Ethanol could easily produce acetaldehyde and thus this reaction is being used as the first step to produce syngas at 300-400° C in the presence of a Cu-based catalyst. A Ni-based catalyst is used in the second step to convert acetaldehyde to syngas. The results show that this two-step system eliminates the coke formation and produces hydrogen close to equilibrium conditions.

Choudhary and Goodman [53] developed another alternative to produce hydrogen via methane steam reforming with a different route to CO-free hydrogen. Choudhary approached the hydrogen production with a two-step process that involves catalytic decomposition of methane and steam gasification of the surface carbon from methane respectively.



Surface carbon (C*) is always produced in the first step of methane decomposition and is removed by water in the second step of steam reforming. Supplying sufficient steam successfully eliminates most of the carbon formation on the catalyst by shifting the reaction balance towards carbon steam reforming. However, the primary breakthrough of addressing

the nickel-based reforming catalyst deactivation is from the innovation of alloying the surface of the catalyst. Carbon-induced catalyst degradation is principally correlated with the electrocatalytic and catalytic activity of reforming hydrocarbons on Ni-based catalysts [64]. Nikolla [64] asserts that by synthesizing Ni-containing surface alloys, C atoms will be oxidized rather than forming C-C bonds, as compared to a monometallic nickel-based catalyst. Along similar lines, by adding other transition metals to the nickel, the catalyst performance can be boosted.

Conceptually, the carbon-formation in the catalyst degradation and disintegration could be reduced by increasing the steam-to-methane feed ratio [64]. Conversely, this method is not favoured due to the additional heat that is required to heat and vaporise the water, not to mention the lower energy density in the fuel and additional system components for water/steam supply leading to much more complex systems.

Recent fuel cell systems use internal reforming to reduce the system components for producing hydrogen from carbonaceous fuels. Especially in SOFCs, high composition methane, synthesis gas, or biogas is utilised as primary fuel and can directly be reformed into hydrogen rich gases [88].

2.2.1 Nickel in Alloys

Nickel has been used in alloys manufacturing for centuries since governments started using it for coins. Nickel is a transition metal in group 10 (formerly group VIIIb) of the periodic table. It is malleable, ductile, solid at room temperature, relatively strong, and tough. Nickel is not only a good conductor of heat and electricity, but also a quite respectable magnetic material too. Due to some of its internal characteristics, nickel is often found as one of the primary alloy materials for various appliances.

Alloys have been appealing and used massively for manufacturing technology due to the combination of strong points from each of the combined metals. Stainless steel, for example, has remarkable corrosion resistance, high temperature strength, thermal expansion and magnetic characteristics compared to the characteristics from each of the components in the alloy. Inconel, nimonic, and other nickel-based super alloys are generally heat resistant and exhibit resistance to surface degradation and mechanical strength far superior than other alloys [89]. Nickel-based, iron-based, and cobalt-based super alloys have been established to be used for many applications such as turbine manufacturing, metal processing, medical applications, heat-treating equipment, nuclear power systems, chemical and petrochemical industries, and coal gasification & liquefaction systems.

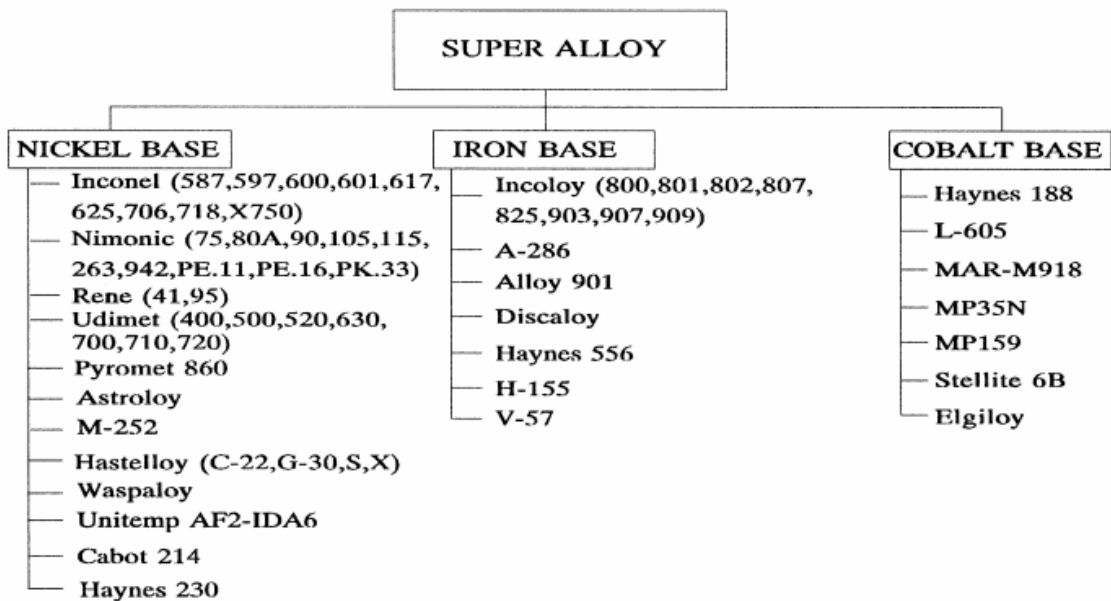


Figure 14 Classification of super alloys [89]

Ezugwu [90] explains the continuous study in nickel-based alloys and their development: The characterisation can be strengthened by improving its microstructure or phase [90] as described below:

1. Alloy Matrix (γ). The nickel-based alloy matrix is face centred cubic (FCC) in an austenitic phase. This condition usually contains a high percentage of solid solution.
2. Gamma Prime (γ'). In super alloys, a high volume fractions of FCC γ' will be precipitated coherently with the austenite using aluminium and titanium.
3. Carbides. Carbon is needed to be a small part of the composition to react with reactive and refractory elements present to form the carbides.
4. Grain boundary γ' . Optimisation of rupture properties is developed with generating a film of γ' along the grain boundaries in the heat treatment.
5. Topologically close packed (TCP) phases. Plate-like phases such as σ , μ , and Laves form will promote ductility and lower rupture strength.

2.2.2 Nickel-based alloys in SOFCs

Nickel has been used as the leading metal catalyst for internal reforming SOFC anodes in the form of Ni/YSZ. Ytria-stabilised-zirconia and NiO form a porous cermet with sufficient active area which at high temperature will be the pathway for the electron and oxygen ions to migrate within the electrode.

This cermet also gives stable performance with decent lifetime thus making it the prominent candidate to be coupled with other transition metals to form alloys. The heat that is produced by the polarisation and ohmic losses can be used in the endothermic internal reforming reaction [91]. The heat production from the fuel cell reaction is twice as much as the heat being consumed by the internal reforming reaction under typical conditions in the same study. Furthermore, they concluded that the continuation of the reforming reaction is secured from thermodynamic equilibrium as the result of continuous consumption of hydrogen.

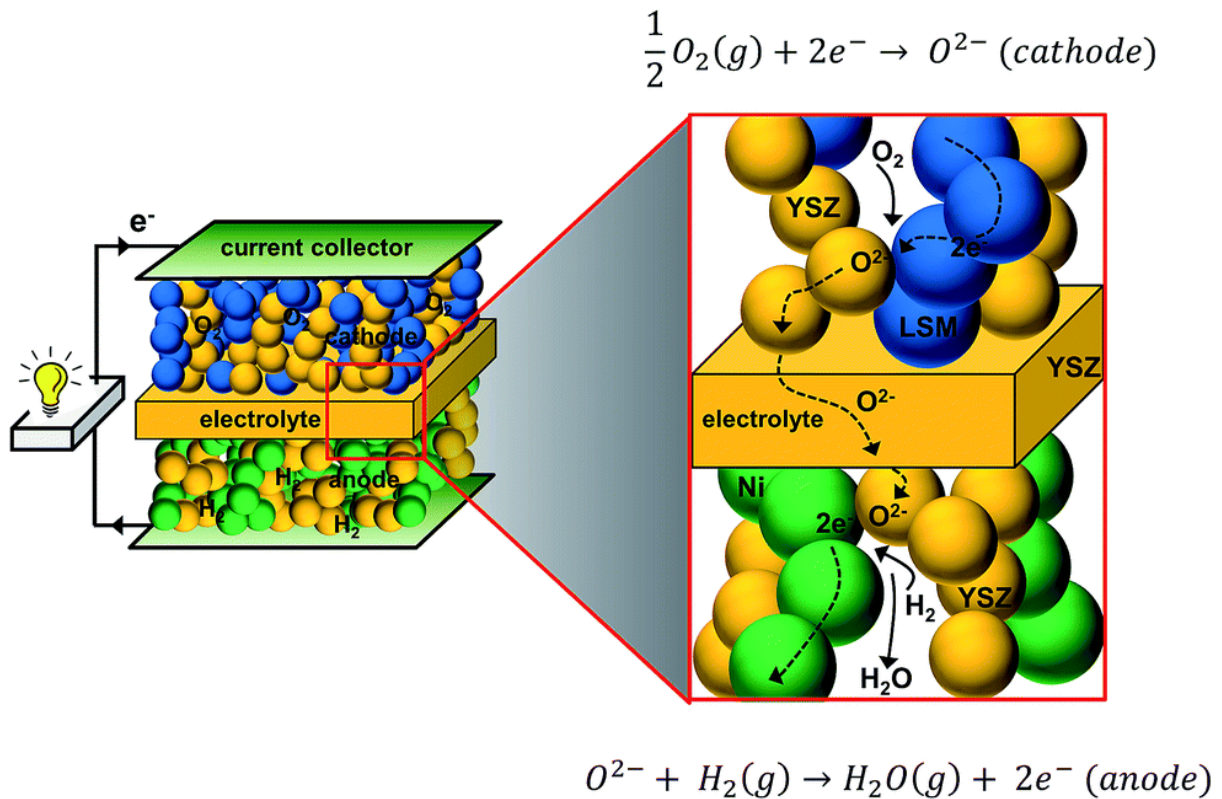
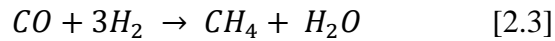


Figure 15 The electron and oxygen ions course within the solid oxide fuel cells [92]

The background idea of using nickel for SOFC catalysts comes from the use of catalysts for hydrocarbon cracking. Nickel catalysts have been used in refineries for cutting the long hydrocarbon chains into shorter ones before undergoing further processing. However, the problem with carbon filaments always occurred and led to short catalytic lifespan. Due to this reason, nickel is to be coupled with another transition metal to enhance the performance and to deal with the challenge.

In SOFC, the nickel-based alloy has many variants with transitional metal group elements, both non-noble and noble. Nickel is partially chosen specifically to be used in the internal reforming reaction on the consideration of the effectivity and great practical importance of the reactions involved. Internal reforming SOFCs need methane, steam and/or carbon dioxide with carbon monoxide and hydrogen as the primary product for the fuel cell. Moreover, nickel is also found to be the cause for methanation of carbon monoxide (2.3),

disproportionation of CO (2.4), and hydrogenation of carbon deposited on the surface catalysts (2.5) [93].



The reaction shown in (Eq. 2.3) is the methanation on the nickel catalyst under specific conditions. Araki and Ponec [93] found that the rate of hydrogenation (Eq. 2.5) is slower than the methanation of H₂/CO on the nickel surface if carbon is deposited, as opposed to the higher rate of hydrogenation on a clean nickel catalyst surface. Hydrogen and carbon monoxide compete for the same sites before hydrogen enters the reaction with carbon deposited. Dissociative chemisorption is concluded as the main condition of methanation from hydrogen and carbon monoxide mixtures [93]. The dissociative primary processes can be summarised into several steps as follows:

- Dissociation of hydrogen and carbon monoxide



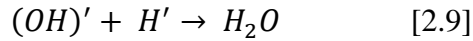
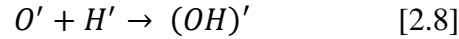
CO will hinder methanation from C' because of stronger adsorption than hydrogen thus followed by hydrogen reaction in absorbed state (Eq. 2.5)

- Reaction in absorbed state

Reaction (Eq. 2.5) shows the reaction of hydrogen in the absorbed state. This reaction can be the foundation of hydrogenation under the same operating condition.

- Oxygen interaction

Aside from hydrogen, oxygen also exists in the absorbed state and has a high probability to interact on the spot.



Therefore, the products of dissociation from reaction (Eq. 2.3) and (Eq. 2.4) with CO are CH₄, CO₂, and H₂O.

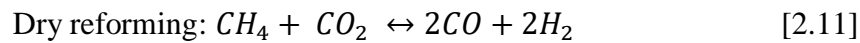
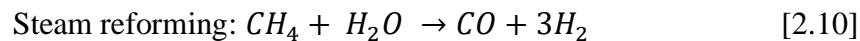
The dissociation products show that the nickel catalyst is more than capable to produce the fuel needed in SOFCs. On top of that, nickel can also, up to a certain point, reduce carbon deposition on the catalyst surface. To exploit advantages over pure monometallic nickel, nickel-based alloys can be a powerful choice for SOFCs with internal reforming since the products of dissociation on nickel are the main fuel for the SOFC. Furthermore, the carbon monoxide in the products can be oxidised (with some limitation) to produce more carbon dioxide.

2.3 Internal Reforming of Methane

The most favourable pathway to produce a hydrogen feed for SOFCs is via internal reforming of methane. This system offers several advantages compared with the pre-treatment in a separate reformer thus making SOFCs special because they do not need pure hydrogen as fuel. Another advantage is that methane and carbon dioxide can be obtained for instance from biogas after desulphurisation and pre-treatment, thus lowering the capital cost and reducing the possibility of lower efficiencies with a longer process of pre-treatment.

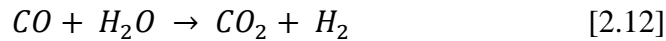
The type of oxidant in the reforming reaction will give different final results when oxidising methane to produce carbon monoxide and hydrogen. In the Autothermal Reforming System (ATR), using pure oxygen in the reaction will serve the purpose of exothermic oxidation of

methane which is thermodynamically advantageous but comes with several problems [94]. According to Lavoie [94], ATR needs to combine and utilize CO₂ and H₂O in the systems. It is an important step to obtain conversions without producing solid carbon. Steam methane reforming (SMR) is comparable to ATR but using steam as the oxidising agent and all reactions will be endothermic.

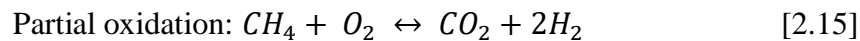
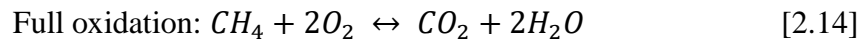


These steps are very essential for synthesis gas and hydrogen production [51] because several reactions will occur concurrently inside the system either in parallel or in series [95]. The methane dissociation on nickel as shown previously in (Eq. 2.1) indicates the start of a long chain of processes in which various studies have identified different mechanisms and operating conditions. One of the reactions that is always present in this process is the Boudouard reaction (Eq. 2.2) where the carbon formation will gradually cover the porosity of the anode support [88]. Furthermore, the fuel cell reaction produces steam and this could possibly be used for the reforming reaction, reducing the external steam feed, and even more so if anode off-gas recycle is used [88,91].

Several studies further explain that additional H₂O and CO₂ being fed with the fuel could move the reaction equilibrium to promote the water gas-shift (WGS) reaction (Eq. 2.12) and syngas reaction (Eq. 2.13). There are several reports that found carbon deposition could be reversed into carbon dioxide with enough steam (in the steam reforming reaction) [29,96] and carbon dioxide into carbon monoxide (in the dry reforming reaction) [96]. The additional H₂O and CO₂ will reduce the methane or CO concentration in the system thus encouraging the reversal of the carbon formation reactions.



As a favourable method to produce hydrogen, internal reforming consists not only of steam reforming but also of several other reactions that are important in occurrence. Internal reforming reactions for SOFC can be performed without oxygen, both the electrochemical oxidation and the hydrogen production. This method is known as dry reforming as shown in equation (2.11). Dry reforming is another alternative reaction pathway of steam reforming (Eq. 2.14 – 2.16) but using carbon dioxide as the oxidising agent for methane. The dry reforming reaction will also produce hydrogen and carbon monoxide as main products with the help of a nickel-based catalysts. The hydrogen and carbon monoxide will further electrochemically oxidize to produce electricity.



The use of the dry reforming reaction is not as favourable as ATR because of its thermodynamic disadvantages as it is endothermic (requires +247 kJ/mol)[94]. Due to the requirement of heat for the endothermic reaction in dry reforming, it is very challenging to counter the thermodynamic barrier for the reaction. Carbon dioxide is a completely oxidised and very stable form of oxidant, thus needs more energy to make this compound react with others. According to Nikoo and Amin [97], there are at least 17 reactions involved in dry reforming, depending on the temperature, based on employing equilibrium computations of R-Gibbs reactor with the Aspen Plus, Aspen TechTM. Table 8 shows the results of using the

modelling of the CO₂/CH₄ ratio 0.5 and 3, pressure range 1-25 atm, the temperature range of 300° and 1200° C and the Suave-Redlich-Kwong (SRK) model for the equation of state.

Table 8 Gas phase reactions on CO₂ reforming of methane [97]

Rxn number	Reactions	$\Delta H_{298} \left(\frac{kJ}{mol} \right)$
1	$CH_4 + CO_2 \leftrightarrow 2CO + 2H_2$	247
2	$CO_2 + H_2 \leftrightarrow CO + H_2O$	41
3	$2CH_4 + CO_2 \leftrightarrow C_2H_6 + CO + H_2O$	106
4	$2CH_4 + 2CO_2 \leftrightarrow C_2H_4 + 2CO + 2H_2O$	284
5	$C_2H_6 \leftrightarrow C_2H_4 + H_2$	136
6	$CO + 2H_2 \leftrightarrow CH_3OH$	-90.6
7	$CO_2 + 3H_2 \leftrightarrow CH_3OH + H_2O$	-49.1
8	$CH_4 \leftrightarrow C + 2H_2$	74.9
9	$2CO \leftrightarrow C + CO_2$	-172.4
10	$CO_2 + 2H_2 \leftrightarrow C + 2H_2O$	-90
11	$H_2 + CO \leftrightarrow H_2O + C$	-131.3
12	$CH_3OCH_3 + CO_2 \leftrightarrow 3CO + 3H_2$	258.4
13	$CH_3OCH_3 + 3H_2O \leftrightarrow 2CO_2 + 6H_2$	136
14	$CH_3OCH_3 + H_2O \leftrightarrow 2CO + 4H_2$	204.8
15	$2CH_3OH \leftrightarrow CH_3OCH_3 + H_2O$	-37
16	$CO_2 + 4H_2 \leftrightarrow CH_4 + 2H_2O$	-165
17	$CO + 3H_2 \leftrightarrow CH_4 + H_2O$	-206.2

The K value (Eq. 2.17) determines to what extent a reaction occurs. The reactions will be irreversible when K is much higher than 1, but for K in the vicinity of 1, the molar ratio will have a bigger role in determining the result [97].

$$K = \exp(-\Delta G_r^0/RT) \quad [2.17]$$

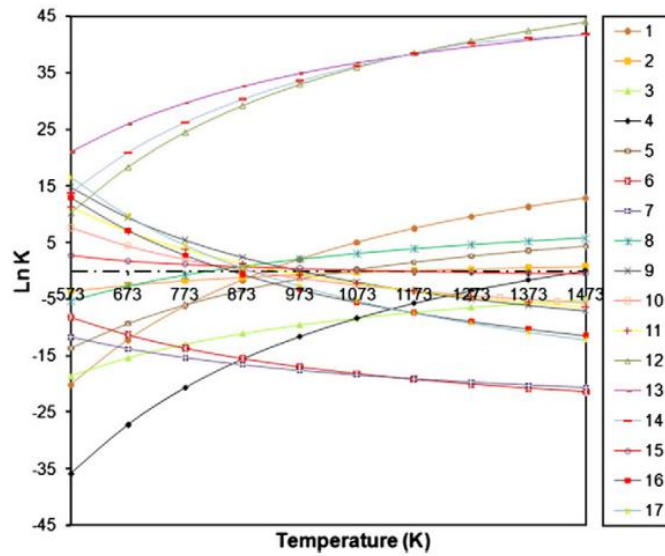


Figure 16 Equilibrium constant of reactions involved in the methane-carbon dioxide reaction at different temperatures, at atmospheric pressure [97]

If the Gibbs free energy change of reaction (ΔG_r) is negative, a larger $\text{Ln}(K)$ indicates to a higher chance of spontaneous reactions. The oxidative coupling reactions (reaction number 3 and 4) in Table 8 will not likely occur except in very high temperature condition, as with reaction number 5. When the $\text{Ln}(K)$ is negative like in reaction number 6 and 7, it would be much favourable towards the reverse side of the reactions with increasing temperatures. Reaction number 15 is influenced by equilibrium limitations, meanwhile reaction number 12-14 can be directed to move towards the right side of the reactions. When $\text{Ln}(K)$ is in the vicinity of zero (within the considered temperature range) such as reaction 16 and 17, the composition of the products may then vary due to the positive magnitude of the $\text{Ln}(K)$ but restricted at high temperature due to the negative $\text{Ln}(K)$.

Methane Conversion

According to Nikoo and Amin [97], for all CH_4/CO_2 ratios, the methane conversion will be always increasing with increasing temperature (up to 1000 K). They concluded that carbon dioxide gas must have a soft oxidant factor as a positive effect on methane conversion. This

positive effect will be more pronounced at temperatures lower than 700°C. Thus for lower temperature SOFC systems, adding more carbon dioxide offers higher activity. Nonetheless, the exothermic reactions number 16 and 17 in Table 8 hinder CH₄ conversion.

From the experimental results reported by Cosimo et.al [98] displayed in Figure 17, it can be shown that the methane to carbon dioxide ratio for different temperatures and its carbon deposition effect can be explained with the carbon-hydrogen-oxygen ternary diagram. From this knowledge, Cosimo et.al. compared the methane conversion of various CO₂:CH₄ ratios with temperature fixed at 800°C. They found that except for the case of pure methane (CO₂ = 0), the increase of reaction products is linear with methane augmentation. The relative conversion of methane (CH_{4,rel.conv}) is the ratio between the converted methane and methane in the inlet mixture. Conversion will be poor for the ratio CO₂:CH₄<1 because the CH_{4,rel.conv} is between 10-30%. It is evident that the conversion in reforming is dependent on the inlet gases ratio.

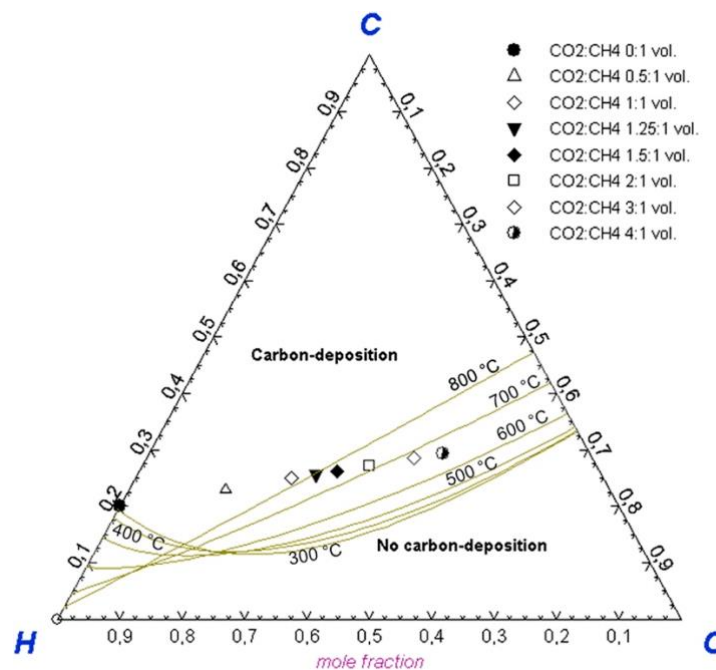


Figure 17 Position of the mixtures of inlet gases in the carbon-hydrogen-oxygen ternary diagram [98]

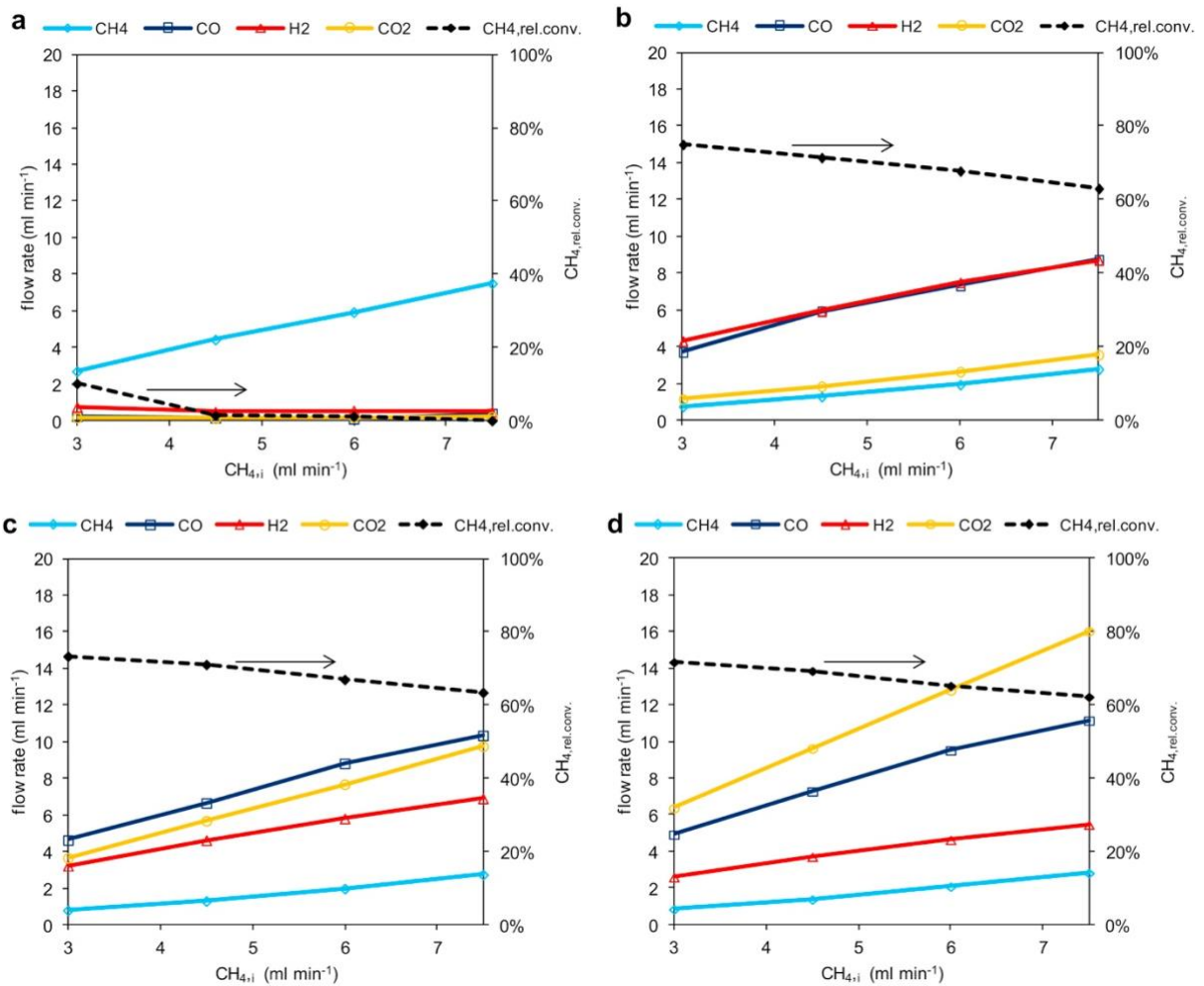
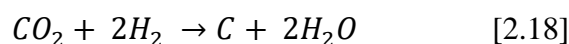


Figure 18 Comparison of the outlet gas composition at 800° (~70 mg): (a) pure methane, (b) CO₂:CH₄=1, (c) CO₂:CH₄=2, (d) CO₂:CH₄=3 [98]

Carbon Dioxide Conversion

Conversion of carbon dioxide needs to be considered since CO₂ as soft oxidant has a positive effect on methane conversion in dry reforming. According to Nikoo and Amin [97], there are two trends on CO₂ conversion versus temperature for all CO₂/CH₄ ratios. The first one is the case at lower temperatures beginning from 300°C to about 600°C when the carbon dioxide decreases gradually. This trend can be described with reaction 2.18.



The exothermic reaction 2.18 is more favourable at the lower temperature range. Meanwhile, at higher temperature starting at approximately 650°C to 1000°C, the carbon dioxide begins to enhance as endothermic reactions (reaction 1 and 2 in Table 8). This offers the theory that dry reforming reaction and WGS reaction are favourable at higher temperature.

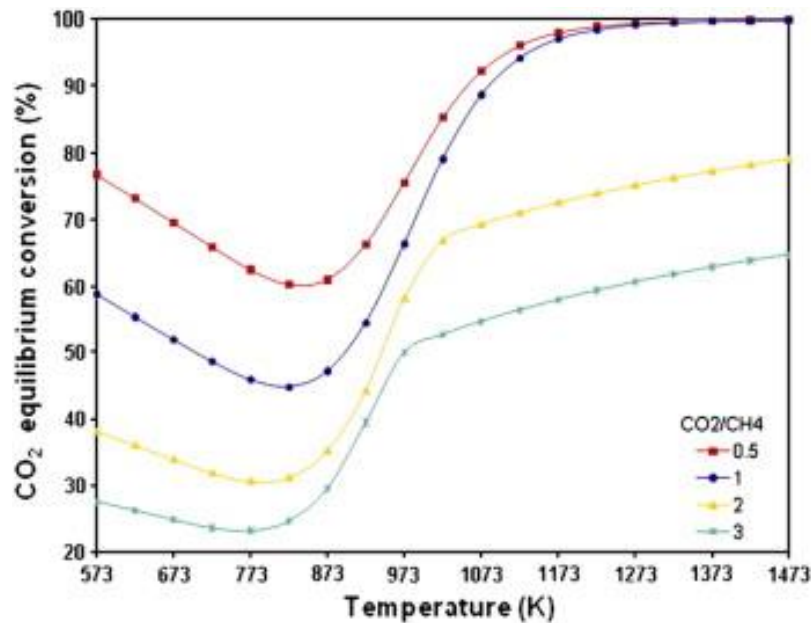


Figure 19 Carbon dioxide conversion as a function of temperature and CO_2/CH_4 ratio at 1 atm and for $n_{(\text{CH}_4+\text{CO}_2)} 2 \text{ mol}$ [97]

As shown in Figure 19, CO_2 is converted less as the CO_2/CH_4 ratio increases. Methane is the limiting reactant so that at a ratio higher than 1 when the stoichiometry is shifted to CO_2 . Figure 19 shows that CO_2 is just left over and does not react to CO. It is because on CO_2/CH_4 ratio greater than 1, carbon dioxide conversion is less thus the equilibrium conversion of carbon dioxide would be left incomplete. The explanation from [97] study is that the dissociation of CO_2 to CO is more likely to happen in dry reforming than methane decomposition by the catalyst. Furthermore, Hecht [99] showed the experiment results of CO_2 reforming that led to higher CO levels than H_2 levels in dry reforming systems.

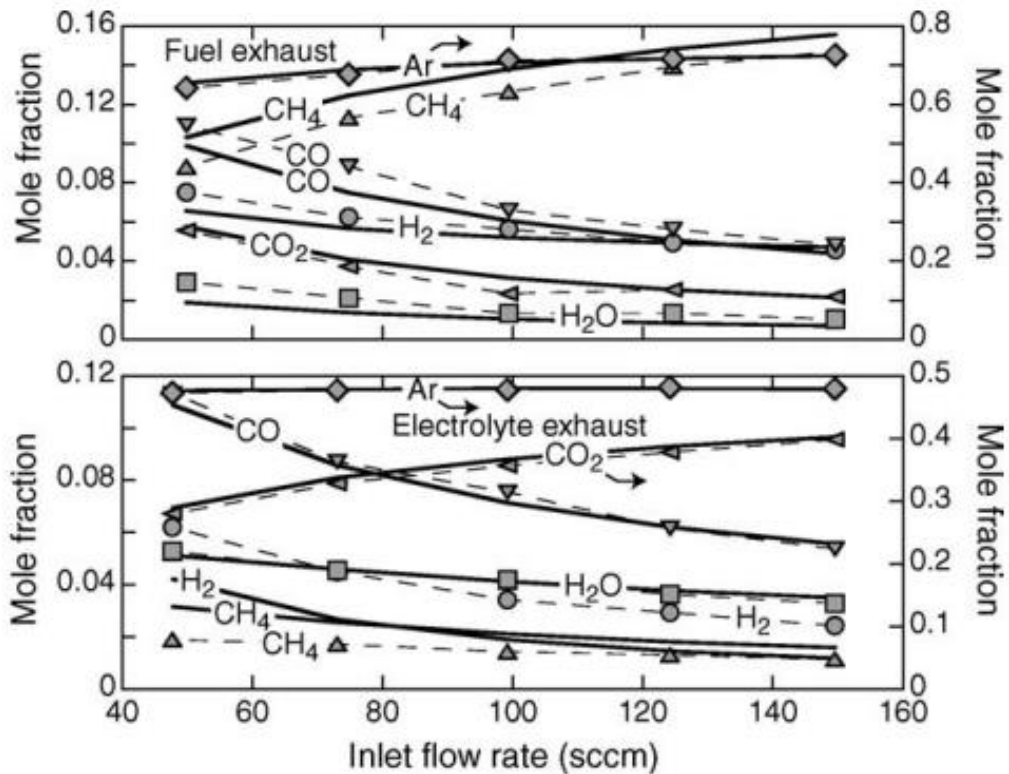


Figure 20 Comparison of measurements (symbols) and model (solid lines) for dry reforming (CO_2) within the anode ($\text{CH}_4 = 0.20$, $\text{H}_2 = 0.028$, $\text{Ar} = 0.772$, $\text{CO}_2 = 0.5$, temp 800°C) [99]

2.4 Anode Supported Utilization with Sn Dopant Addition

The Ni-YSZ cermet has found extensive use in SOFC operation because of its high flexibility in using different fuels. The material that has been used since the first generation of SOFCs is the cermet from monometallic nickel oxide with an yttria-stabilised-zirconia (YSZ) skeleton. The nickel volume fraction is typically in the range between 40 to 70% [100–102] using 8 mol% YSZ (8YSZ) to build the anode cermet. The percentage is based on the difference in thermal expansion coefficient (TEC) which is $1.69 \times 10^{-5} \text{ K}^{-1}$ and $1.05 \times 10^{-5} \text{ K}^{-1}$ for nickel and 8YSZ respectively [101]. The same observation also concluded that this discrepancy will majorly effect the microstructure and the mechanical strength of the SOFC anode cermet in thermal cycling.

This cermet also supplies high porosity, high conductivity, and high temperature resistance, aside from the mechanical strength for the cells. The high temperature resistance characteristic is especially important in SOFC systems as the typical operating condition is between 650° and 850°C. There are limited options of materials that resist high temperatures for a sufficiently long period of time with high conductivity and catalytic activity. The potential candidates aside from the SotA Ni-based cermets include cermets from Cu-based [103,104], Rh-based [105] and in some rare cases Pd-based [106] composition. Yet, other metals in the anode do not offer as high catalytic activity as nickel both in hydrogen and oxygen as shown in Figure 21 and Figure 22. Thus, Ni/YSZ needs to be observed carefully in the anode supported SOFCs, especially the relationship between the nickel and the transition metal on the surface.

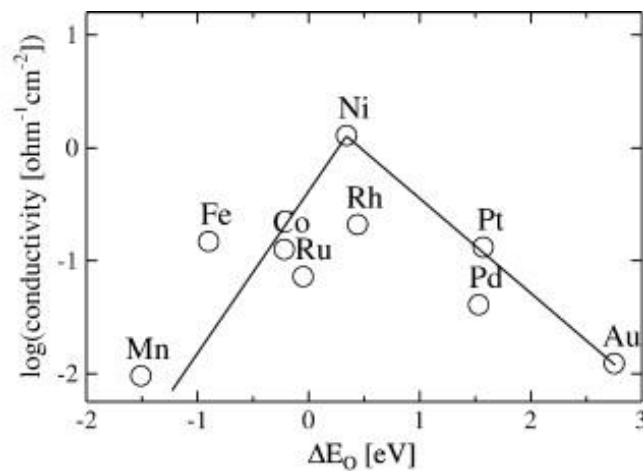


Figure 21 The measured conductivity plotted against calculated adsorption energies of oxygen on the close-packed pure metal surface [107]

The efforts to tackle the problem with nickel based catalysts in SOFCs have been ongoing for nearly three decades. It is possible to use other single based catalysts for SOFCs but the current use of other types of transition metals is not as good as nickel based catalysts [63]. Other transition metals that have been used for finding nickel based alternative catalysts include Ru [108,109], Cu [103,104,110], and various complex perovskites [111–114].

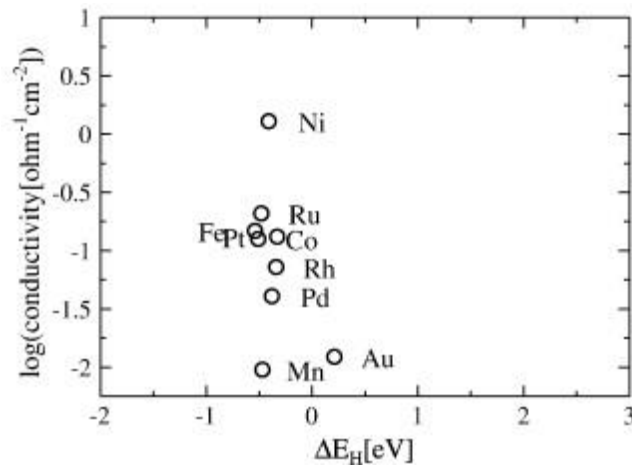


Figure 22 The measured conductivity plotted against calculated adsorption energies of hydrogen on the close-packed pure metal surface [107]

The early anode supported SOFC with dopant addition predominantly used Cu-based anodes with various dopants such as: Pd, Pt, and Rh [115]. The idea was to avoid catalysing carbon formation when using Ni-based anode SOFC. The satisfactory results of dopant addition in Cu-based anodes led to further investigations within Ni-based anodes using the dopant that previously mentioned.

There are several dopants from various transition metals that have been studied to be combined with nickel for anode supported SOFCs. According to Niakolas [59], the candidates for the dopant can be separated into the non-noble transition metals such as tin (Sn) [61,64,84,116,117], Cu [118,119], Mo [120,121], Bi [122], Fe [123–125] with the noble metals such as Au [60,62,63,126], Pt [127], Ru [128,129], Pd [130,131], Rh [132,133] and Ag [134]. From the various options of metals, tin offers quite a promising potential compared with the more expensive noble metals.

Tin has been widely accepted and known for the last ten years as one of the viable options for enhancing Ni/YSZ cermet cells in internal reforming SOFCs. Sn has been studied extensively by using Density Functional Theory (DFT) calculations and modelling [61,64,65,135]. The Sn-dopant delivers satisfactory results in reducing the amount of

filamentous carbon on the surface of the SOFC anode according to several studies [59,84,117,136]. The manufacturing method that is most popular for producing the anode supported SOFCs with Sn is via impregnation using methods such as incipient wetness, sonic immersion and pipette drop. The impregnation method introduces tin and forms an alloy with nickel with a quite homogenous dispersion of tin and possibly forms an alloy not only on the surface but also all over the anode. Study has found that using the pipette drop technique to introduce the tin dopant [116,137] can be a quite easy, cheap, and efficient way to form the required Sn-Ni alloy on the anode surface with remarkable carbon reduction in dry reforming systems.

In this study dopant addition will be defined as the added transitional metal for promoting nickel alloy catalysts on the surface of anode supported SOFCs. The dopant that being used in this study was Sn in the form of $\text{SnCl}_2 \cdot 2\text{H}_2\text{O}$, before being turned into dopant solution with ethanol (99.5%-vol). Anode supported cells can be used on SOFC internal reforming system without any dopant addition with stable performance for relatively short time before breaking down or cracking due to carbon formation, unless sufficient steam is added to the fuel.

2.5 Tin Performance on Fuel Cells

A predominant theory about Sn-Ni alloy catalysts for anode supported internal reforming SOFCs is that the cell will also be more resilient towards sulphur poisoning [59]. Future tests with internal reforming in SOFCs should be run with real biogas fuel with various degrees of impurities on optimal operation conditions which includes high temperature. If an SOFC is going to be used with real biogas fuel, sulphur will always be present as prominent impurity along with others, such as halogens and siloxanes.

The existing theory on Ni/YSZ with Sn dopant is that Sn and Ni will form an alloy on the anode surface thus giving more potential for forming thermodynamically stable states for C atoms [135]. The detailed phase transformations between Ni and Sn to form the Ni/Sn system has been studied by Schmetterer et.al. [138]. Based on [138], there are several Sn/Ni phases that exist at various composition and temperature conditions as illustrated in Figure 23.

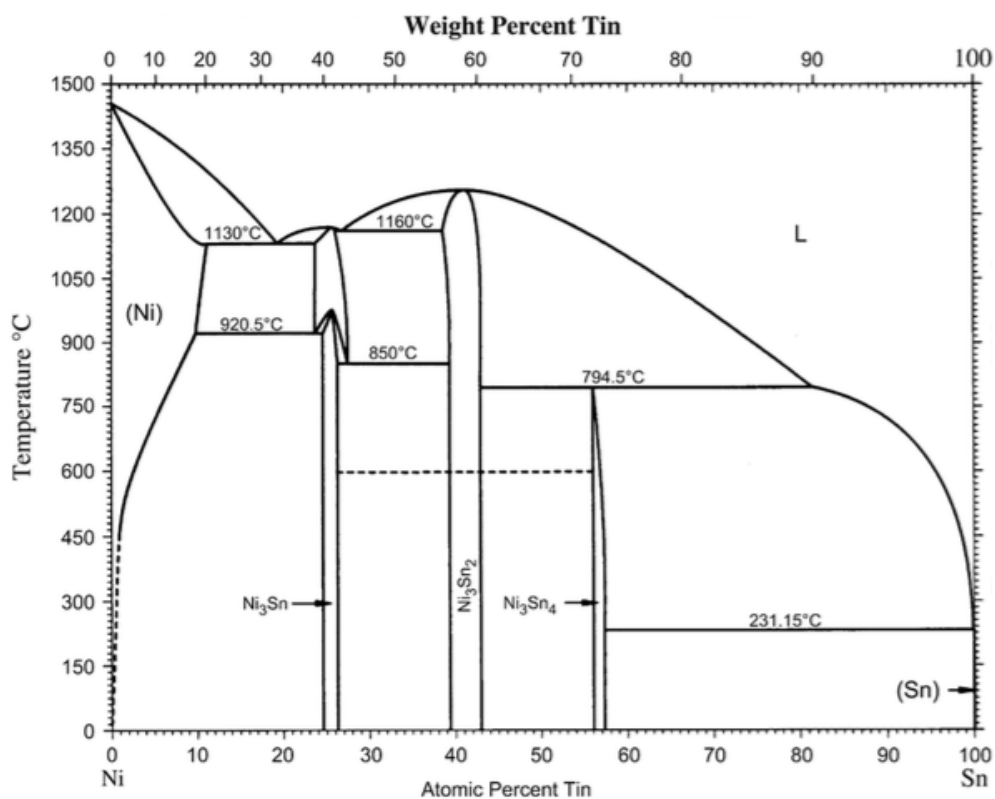


Figure 23 Ni/Sn phase diagram [138]

Nikolla's group offers elaborate explanations about Sn/Ni supported on YSZ using steam reforming reactions in several of their studies [61,64,139]. Nikolla's theory on carbon formation on the nickel surface based on DFT calculations in accordance with d-band model is that carbon tends to nucleate on the undercoordinated sites of a Ni layer and requires a number of connected Ni sites [64,140]. Furthermore, there are two stable thermodynamic state for C atoms: CO from the oxidation and C-C bonds from the extended carbon network

(graphene). By these theories, their group offers two ways of reducing the carbon formation on the nickel: 1) alloying, 2) disrupting the connectivity of the undercoordinated Ni sites.

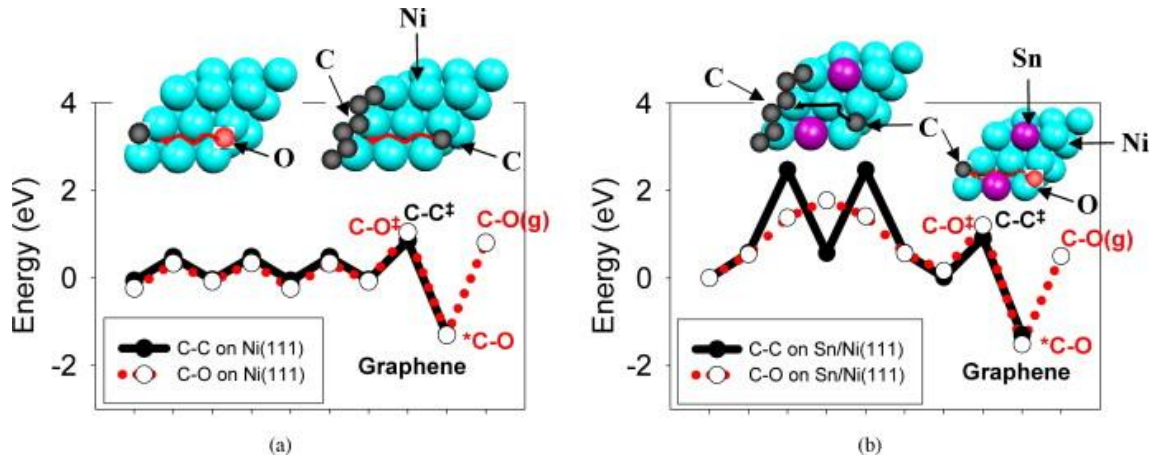


Figure 24 DFT-calculated reaction energies for C-C and C-O bond formation on a) Ni (111) and b) Sn/Ni (111) [64]

By modifying the nickel catalyst surface with Sn, the Sn atoms will replace Ni atoms on the top Ni (111) layer. This will lead to partial selectivity of C-O and C-C bond formation. As shown in Figure 24, the Sn/Ni surface alloy shows lower energy ‘barrier’ for C-O bond formation than C-C bond. Furthermore, carbon nucleation also being observed with the second theory, by disrupting the undercoordinated Ni site connectivity. It was concluded that undercoordinated Ni sites bind carbon more strongly than undercoordinated Sn/Ni sites [64].

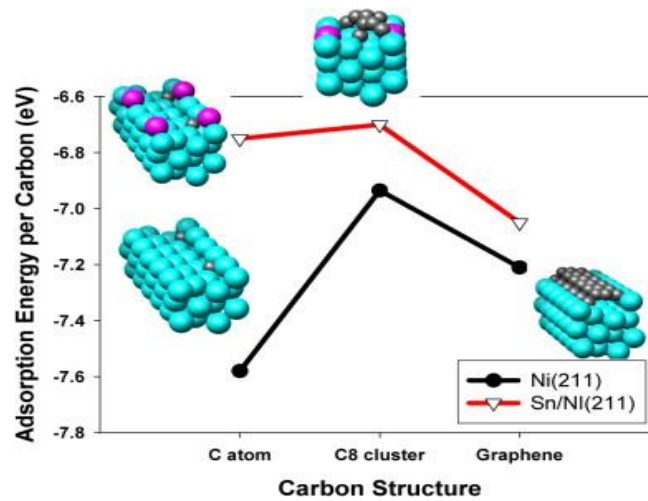


Figure 25 DFT calculated adsorption energies per carbon atom for a C atom, C₈ cluster, and a graphene chain adsorbed on Ni (211) and Sn/Ni (211) [64]

Another remarkable study from Nikolla [64] is the comparison of the Ni/YSZ and Sn/Ni/YSZ in steam reforming for methane conversion. The carbon formation was less observed in Sn/Ni/YSZ. It was also observed that more Sn loading on the Ni surface catalyst was not giving higher methane conversion, as shown in Figure 26. Nikolla's experiment observed that the Ni/YSZ lost almost 45% of its activity on steam reforming just after 2 h of operations and there was approximately 25% reduction in methane conversion when the Sn loading increased from 1 to 5 wt%.

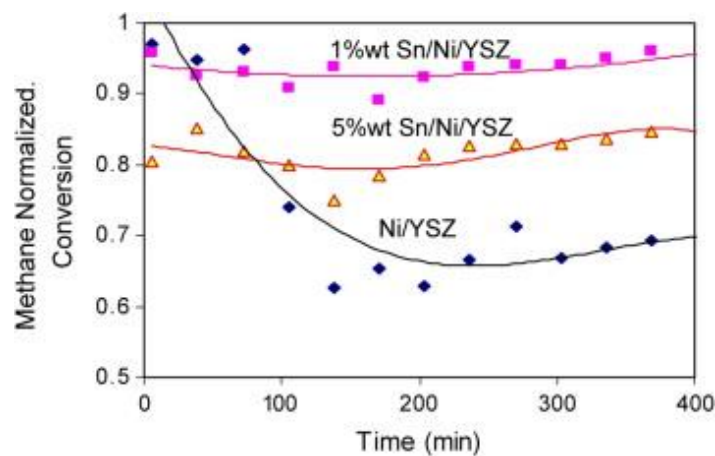


Figure 26 Normalised methane conversion as a function of the time on stream for 1 wt% Sn/Ni/YSZ, 5 wt% Sn/Ni/YSZ, and Ni/YSZ catalysts measured at the steam-to-carbon ratio of 0.5 and at 800°C [64]

The difference in chemical activities between pure Ni and Sn/Ni alloy is related to its changes in the geometric and electronic structure according to Nikolla et.al [135]. The differences can be explained, to some degree, by its geometric effect. For examples, the difference in activation barriers in C-H bonds are explained by Sn blocking the undercoordinated Ni sites which is deemed suitable for activation of C-H bonds. They also found that desorption of carbon monoxide and oxygen between Ni/YSZ and Sn/Ni/YSZ has less gap than C-H bonds. This is explained using the different electronic Ni atom structure and weaker interaction between O and CO adsorbates with Sn sites on the Sn/Ni surface alloy [135]. Their DFT calculation also point out that the chemical activities (adsorption energies on oxygen, carbon, carbon monoxide, and CH fragments) on Sn/Ni are less exothermic than on a pure Ni surface catalyst because it depends on Ni atom electronic interaction with the Sn atoms.

In our group, Troskialina [137] showed a thorough study of Sn dopant on anode supported Ni-YSZ using dry reforming both on hydrogen and biogas. The study also had been done using pipette drop as the primary choice of doping technique. There are several important finding on [137] that can be applied as the base for this study, such as:

- The amount of Sn content on the nickel surface that will give the highest performance for cell testing. As shown in Figure 27, 4D (4 drop of Sn solution) or approximately 1 wt% Sn gave the highest gain in current density at 420 A/cm².

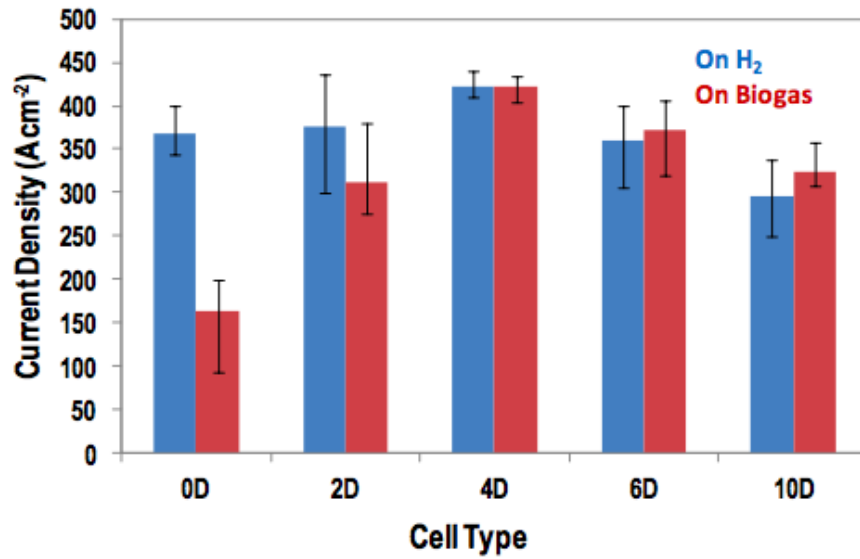


Figure 27 Comparison in current density performance between Ni-YSZ and Sn/Ni-YSZ in various Sn compositions (2 drops, 4 drops, 6 drops and 10 drops) [137]

- The proposed reaction that occurred during the calcination, reduction and alloying using SnCl₂.H₂O and ethanol solution on Ni-YSZ for SOFC. There is an interim stage at 600°C that resulted in SnO₂ when the samples were being calcined. The proposed reaction stage is shown on Table 9.

Table 9 Proposed reactions on Sn/Ni during calcination, reduction and alloying [137]

Infiltration Stage	Reactions
Drying at 70°C and 100°C (solvent evaporation)	$C_2H_5OH_{(liq)} \rightarrow C_2H_5OH_{(vap)}$ $H_2O_{(liq)} \rightarrow H_2O_{(vap)}$
First stage calcination up to 200°C (anhydrous SnCl ₂ formation)	$SnCl_2 \cdot 2H_2O \rightarrow SnCl_2 + 2H_2O_{(vap)}$
Heating to 600°C during calcination (SnCl ₂ evaporation and calcination)	$SnCl_2_{(solid)} \rightarrow SnCl_2_{(liq)}$ $Partial SnCl_2_{(liq)} \rightarrow SnCl_2_{(vap)}$ $Partial SnCl_2 + \frac{1}{2} O_{2(g)} \rightarrow SnO + Cl_{2(g)}$ $SnO + \frac{1}{2} O_{2(g)} \rightarrow SnO_2$
Reduction with H ₂ at 750°C	$SnO_2 + 2H_{2(g)} \rightarrow Sn + 2H_2O_{(vap)}$ $NiO + H_{2(g)} \rightarrow Ni + H_2O_{(vap)}$
Alloy formation at 750°C	$Ni + Sn \rightarrow Ni - Sn \text{ alloy}$

Based on the findings in the literatures study, the summaries can be outlined as follows:

The role of Sn-infiltration in dry reforming using Ni/YSZ cells need to be assessed further conforming to the previous literatures [61,64,135,139] that shows promising evidence in steam reforming operation towards carbon formation and electrical performances. Additional 1 to 5%wt of Sn into Ni/YSZ gave higher carbon and sulphur resistance results with decent lifetime, assuming that Sn and Ni formed into alloy. The Sn-Ni alloy is supposed to be the cause of higher selectivity towards C-O bonds than C-C bonds.

Dry reforming operation is expected to have even better results using Sn-Ni/YSZ because of the C-O bond selectivity which led to higher methane and carbon dioxide conversion (higher power production). Moreover, dry reforming operation using Sn-Ni/YSZ had performed as a good alternative cells in biogas operation [137]. The study reported extensive in-situ characterisations of Sn-Ni/YSZ cells and offered proposed reactions in dry reforming pursuant to the result with its pipette drop infiltration technique.

The pipette drop techniques in Troskialina [137] study require optimisation in itself to ensure that Sn can be infiltrated successfully as of the report. This will also lead to the evaluation of the performance in dry reforming operation. Ex-situ characterisation is needed to offer better understanding from within the Sn-Ni/YSZ cells towards the dry reforming using biogas.

Chapter 3 Methods and Materials

3.1 Overview

This chapter describes the materials that have been used in this study and in the second part the methods employed, ranging from the preparation of the SOFC cell up to the cell performance test. The methodology presented concentrates on what has been used for the project, along with preparation and characterisation. Laboratory methods include the outlet gas monitoring with a gas chromatograph for performance monitoring.

3.2 Materials

Commercial anode-supported cells from Ningbo SOFCMAN Technology Co. Ltd were used for the project. There are several types of SOFC cells from the same manufacturer such as anode support with anode functional layer (ASC), half-cell (HC), and full-cell (FC). Half-cell is the type of commercial cell which consists of an ASC with electrolyte added. Full-cell is the HC with cathode added. All the SOFC types from the Ningbo company were used in the characterisation analysis. The only type used for the cell testing was the FC. This is because the FC type offers repeatability and reproducibility as a prerequisite further detailed in the characterisation analysis.

The FC consisted of a 400 μm thick Ni/YSZ anode support and 10 μm of 8 mol% Ytria-Stabilized-Zirconia (8YSZ) for the electrolyte. The cathode layers in the full cells were made of lanthanum-strontium-cobalt-ferrite (LCSF) with screen-printing technique to give better electrochemical performance on the cell testing rather than using lanthanum-strontium-manganite (LSM) [141].

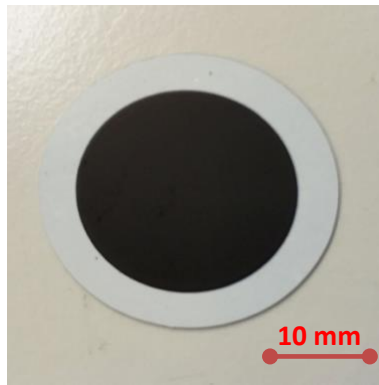


Figure 28 Full cell with LSCF cathode with 30 mm outside diameter and 22 mm inner diameter



Figure 29 Side image of the cell sample

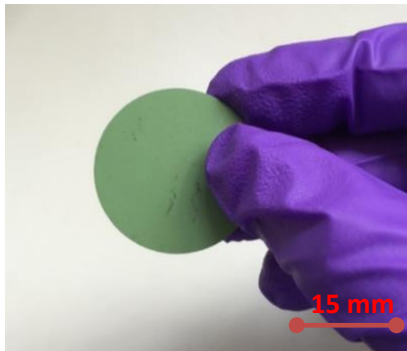


Figure 30 Anode side of the cell sample



Figure 31 Cathode side of the cell sample

Silver wire and silver paste acted as current collector on both anode and cathode surface. The cell samples were sealed using dense silver paste with sufficient thickness to ensure that there were no holes for gas leaking when the cell was tested. The cell holder for the cell testing was made from an alumina (macor) cylinder with ceramabond sealing. Tin solutions for doping were made from $\text{SnCl}_2 \cdot 2\text{H}_2\text{O}$ and pure ethanol. The details of the Sn-infiltration methods will be further described in section 3.3.1.

The images in Figure 28-31 show the display of the full cell sample for cell testing. This commercial cell is a typical button fuel cell with 30 mm diameter, 22 mm cathode diameter and approximate surface area of 20 mm^2 . The effective area of the cell is less than the whole area because of the current collector application. The current collector needs to be placed

directly onto the surface after the treatment and before mounting the cell. The list of materials used in the study is shown in Table 10.

Table 10 List of Materials

Function	Materials	Manufacturer and Product Number
Anode	Ni/YSZ	SOFC AS+AFL cells, Half-cells, and full cells from Ningbo SOFCMAN Tech. Co.
Electrolyte	YSZ	SOFC Half cells and full cells from Ningbo SOFCMAN Tech.Co
Cathode	LSCF	SOFC full cells from Ningbo SOFCMAN Tech. Co
Current collectors	Ag paste	DAD-87
	0.25 mm silver wire	Scientific Wire Company
SOFC Sealants	Ag Paste	DAD-87
	Ceramic Seal	Cerama bond 552-VFG
SOFC Cell holder	Alumina (Macor) cylinder	ALMATH ALM3023, ALM2014
Dopants	SnCl ₂ .2H ₂ O	Sigma Aldrich 431508
	Ethanol	Fischer Scientific (E/0650DF/17)
Fuel gases	Hydrogen, H ₂	BOC
	Methane, CH ₄	BOC
	Carbon Dioxide, CO ₂	BOC
	Helium, He	BOC

3.3 Methods

There are several methods to infiltrate additional catalysts into the cell such as powder blending, sonic immersion and pipette drop. The selected method for this project was via the pipette drop technique to infiltrate Sn into the anode side of the samples. The reason behind

this approach selection was that it allows facile manipulation of commercial cells. Our group has proven the reproducibility and effectivity of this method [137]. It is also comparatively cheaper and repeatable because it uses equipment that is easy to find in any laboratory.

3.3.1 SOFC Sn-infiltration method via pipette drop

The preparation for the pipette drop (doping) technique is started by preparing the dopant solution. There will be two types of samples tested in this study, undoped cell and doped cell. The ‘undoped cell’ is the term used for the standard cell without any additional Sn or without any pre-treatment prior to the test. Meanwhile, ‘doped cell’ is the term used for the sample anode supported cell with Sn-infiltration, either 4 drops or 6 drops of SnCl_2 in 95%-vol ethanol solution. One drop of the dopant solution approximately contains 1 mg of Sn prior to the calcination process.

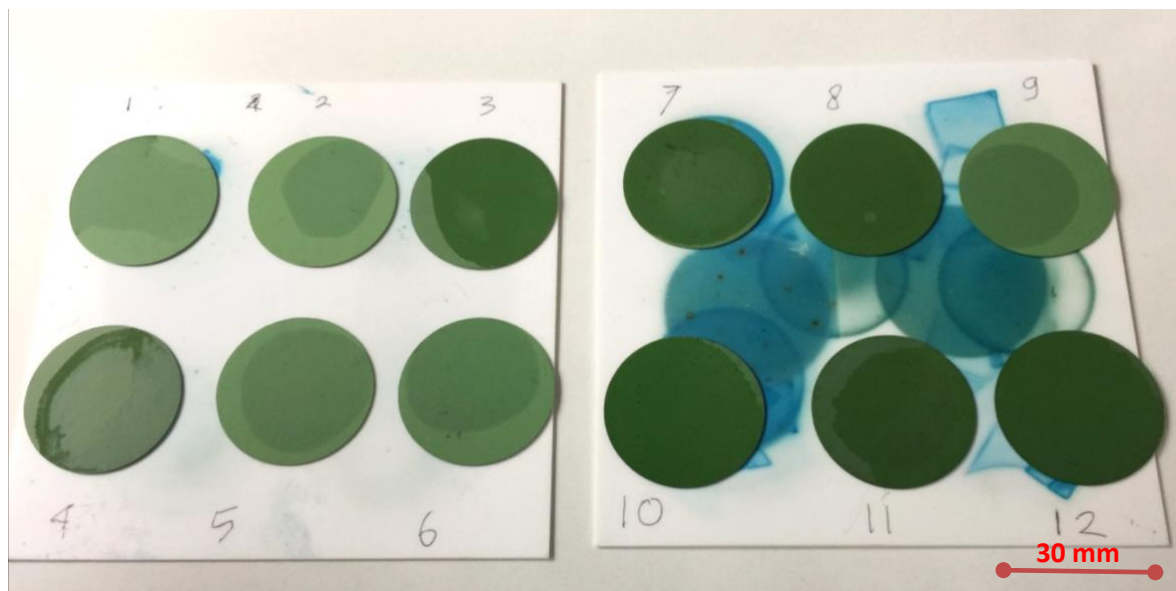


Figure 32 Sample cells when drying in air in between drops

There are three parts of Sn-infiltration method for the cell. The first one is the pre-treatment part whose purpose was to make sure that the cell was ready to be infiltrated by the Sn

solution. The pre-treatment included washing the sample with pure ethanol to clean the surface from any impurities. Ethanol easily evaporates into air. The samples were weighed one by one after being washed. The samples needed to be weighed before the preliminary drying, after the preliminary drying and after calcination. The preliminary drying was conducted at 80°C for one hour in the oven. The cells were placed on ceramic pads as seen in Figure 32.

The Sn-dopant solution was prepared by dissolving 496 mg $\text{SnCl}_2 \cdot 2\text{H}_2\text{O}$ (Sigma-Aldrich) in 95%-vol ethanol and placing it in an ultrasound bath for 30 minutes. By using a 5 ml plastic syringe, this dopant solution was dropped on to the middle part of the anode surface side. The drop was let dry in air for 30 minutes; then drying was continued by using a vacuum oven kept at 100°C for 15 minutes. This was to ensure the dopant solution could dry slowly and gradually to let the Sn infiltrate the porous Ni/YSZ.

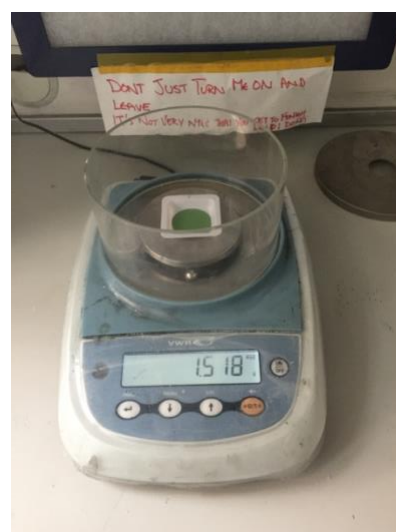


Figure 33 weighing each sample before and after treatment

Before the calcination, the sample was further dried at 100°C for 1 hour. The calcination was performed at 600°C for 2 hours in air using a Carbolite furnace. The heating and cooling rate for calcination was kept at 5°C and 3°C min^{-1} , respectively. The temperature profile for drying and calcination of the Sn-infiltration is shown in Figure 34.

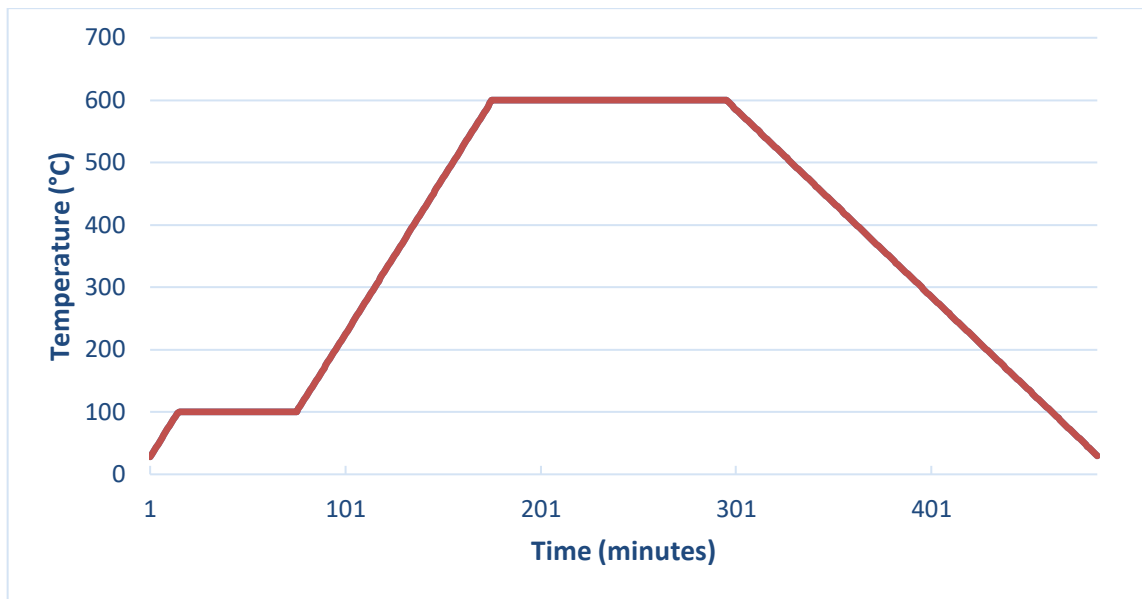


Figure 34 Temperature profile for calcination of Sn infiltrated via pipette drop

3.3.2 SOFC manufacturing steps

Following the Sn-infiltration treatment, the manufacturing steps started with painting dense silver paste onto anode and cathode surface as the place to adhere the silver wires for the electrical performance test. There are two parts of current collectors for both anode and cathode, current and voltage connector. The current connector consisted of three 0.25 mm double silver wires braided into one, approximately 17-18 cm long. Meanwhile, the voltage connector consisted of one 0.25 mm double silver wire.



Figure 35 Cell holder made from an alumina (macor) cylinder with ceramabond sealing

The 0.25 mm pure silver wire was used to make double wire collectors by braiding the wires using a cordless drill driver tool. The silver wires were cut into approximately 1 metre each and braided into double wire 50 cm long. The double wire braided silver was cut into 3 parts and would be braided together again for current connectors. Each anode and cathode surface would be silver-attached with one current connector and one voltage connector. The dense silver paste was carefully painted on to the surface by the shape of a circle with one line in the middle. Both current and voltage connector would be placed on to the line in the middle of the circle after flattening the wires using a small hammer. After that, several layers of dense silver paste were put on top of the wires on the middle line to glue them to the surface. The painted samples with the adhered wires were placed into the oven at 150°C for one hour. Repeat the steps for the other side.

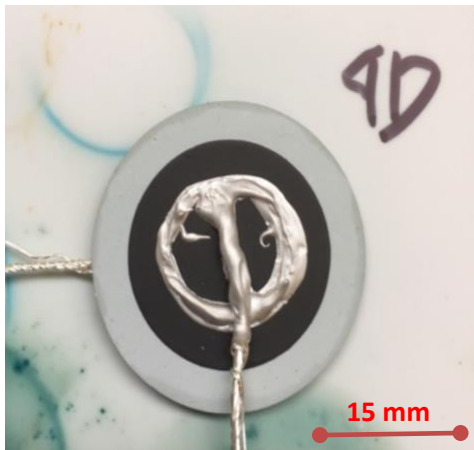


Figure 36 Silver paste application on the cathode side

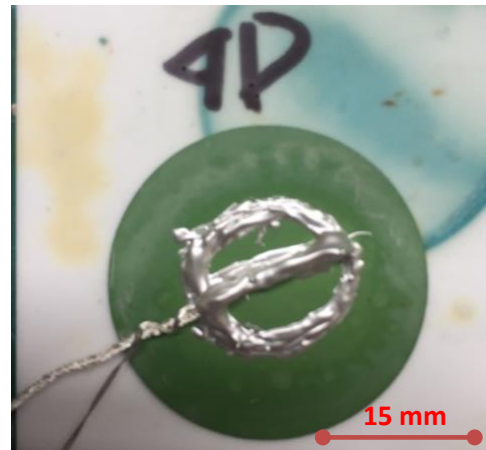


Figure 37 Silver paste application on the anode side

An alumina cylinder was used as the cell holder for the electrical performance test. The cell holder was placed in the ring stand with the help of two test tube clamps to make it stand firm. The cell holder consisted of two alumina cylinders with different size and length, being connected near the edges to give space in between the cylinders for channelling the excess fuels.



Figure 38 Cell holder preparation for mounting the SOFC sample

The SOFC samples were mounted to the cell holder after two layers of dense silver paste were painted on the rim of the cell holder. These additional two layers were applied to fill in any holes after result of mounting the SOFC cell. Thick layers of dense silver paste application were essential since the high temperature operation conditions at the range of 750-800°C for the electrical performance test could lead to delamination of the silver paste.

After the thick application on the rim, outer layer and small part of the SOFC cell edge, the mounted cell was dried in the oven at 150°C over night. To make sure that there were no micro holes on the sealing application, post-inspection of the silver paste sealing was needed. If there were holes after drying overnight, it would need another layer of dense silver paste applied for the sealing and dried for another 3 hours at 150°C.

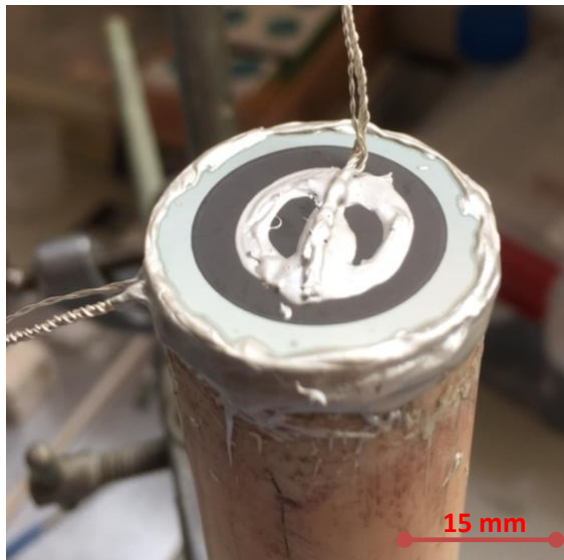


Figure 39 After 12 hours drying in 150 °C for sealing the rim
of the mounted sample

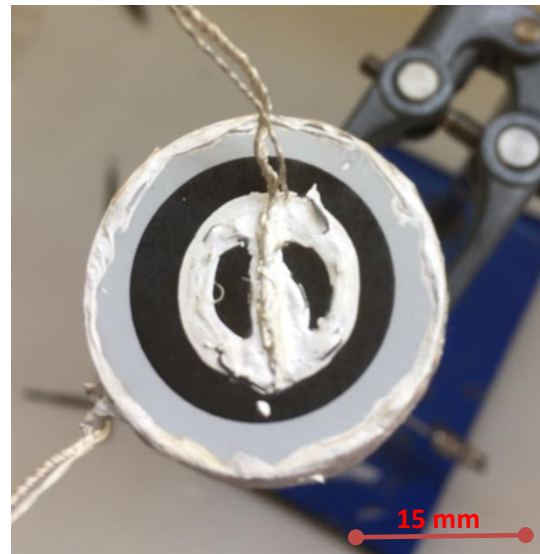


Figure 40 Close-up look of the cathode side after sealing
the sample

3.3.3 Electrical performance test

The electrical performance test was conducted using a horizontal tunnel test furnace from Vecstar. The sample was connected to a Solartron Analytical Model Number 1400A for electrical performance measurements and to a Cirrus mass spectrometer for the outlet gas composition. The mounted cell was placed in the furnace as shown in Figure 41. The cathode was exposed to ambient air and connected with the current and voltage connector to the Solartron. A thermocouple was placed carefully near the surface of the mounted cell, not touching but not too far. Both the wires to the solartron and the thermocouple were held by tube clamps to the ring stand. The cell holder system was connected to four gas feeds; helium (He), hydrogen (H₂), methane (CH₄), and carbon dioxide (CO₂).

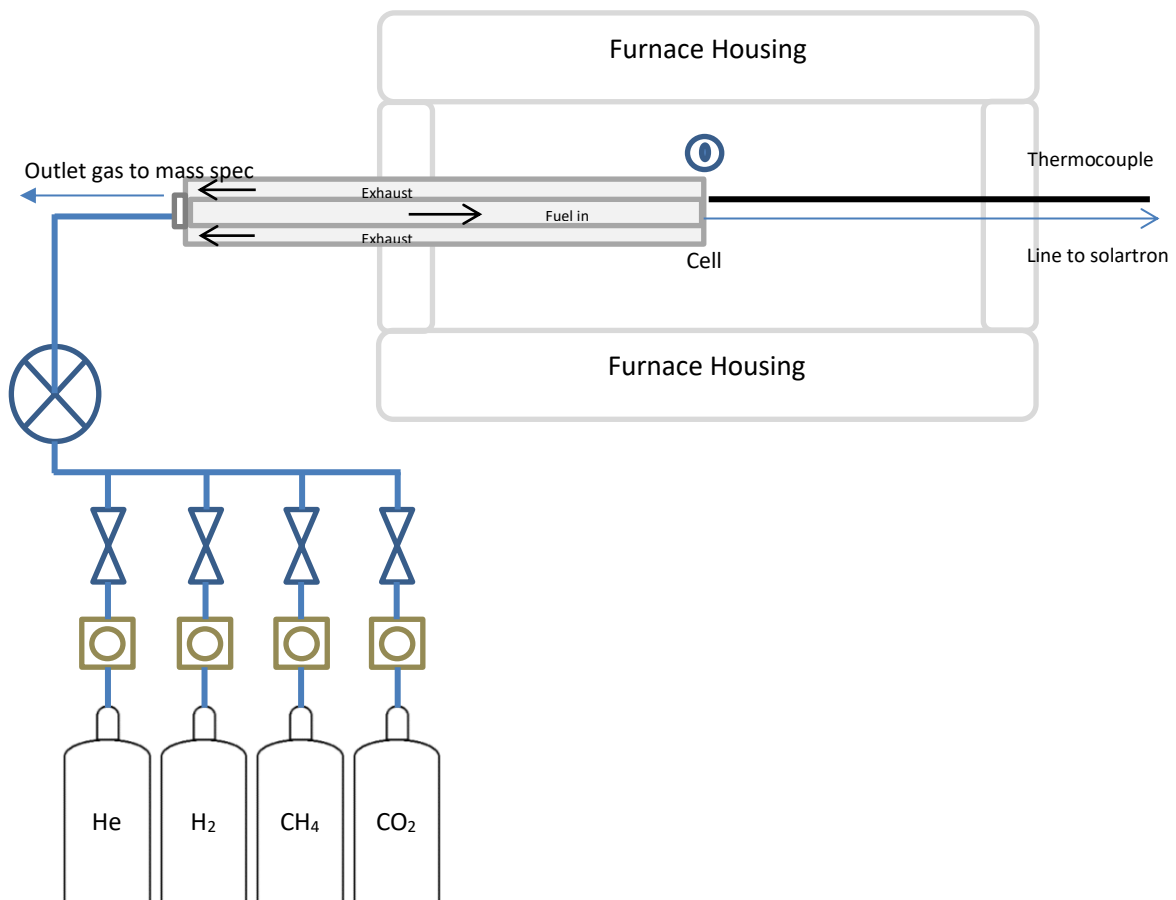


Figure 41 Schematic diagram of the test rig *drawn not to scale

The electrical performance test used four gases in total for the whole run. There were three main parts of the electrical performance test. The first one was the test run on hydrogen with a little bit of helium. The hydrogen test used the flow rate of 21 ml/min for H₂ and 7 ml/min for He. The second part was the biogas testing with a flow rate of 14 ml/min for CH₄, 7 ml/min for CO₂, and 7 ml/min for He. The last part was the hydrogen-post-biogas testing where the ratio for the hydrogen and helium was the same as in the first part. All tests were performed at 750°C. This will be discussed in more depth in Chapter 4.

3.3.4 SOFC outlet gas monitoring

A Cirrus Mass Spectrometer was used to monitor the outlet gas of the electrical performance test. Outlet gas monitoring served several purposes:

- Giving data for output gas comparison with the input gas in real-time,
- Useful for checking for leakage in the silver sealing around the mounted cell,
- Giving the signal if there was any unusual activity with the input gas flow.

The first use for the mass spec was to check if the sealing on the cell holder was satisfactory or needed another layer of silver paste application at low temperature and low gas flow rate. After connecting all the wires to the solartron, placing the thermocouple, and connecting the cell with the gas line, it was important to check the connection of the gas line with soap water for any leakage. The second step of leakage checking was by using a bubble test meter at least twice, right after the start of heating up the furnace (room temperature) and after the furnace had reached the operating temperature for hydrogen reduction (750°C).

The bubble test used the flow rate of 20 ml/min of He into the system. If after reaching high temperature condition the flow at the outlet gas reached 20 ml/min \pm 2 ml, it would be appropriate to continue the procedure of cell testing. If the bubble flow test showed wide

range of differences especially at high temperature, the cell testing could be continued but with notes on the flow rate on the outlet gas line from the cell holder. Some cases even showed undesirable results if there was any leakage on the sealing.

3.4 Imaging and Characterisation

For this study, characterisation of the cell was the primary collectible data for the analysis on the role of Sn in the anode supported cell. Scanning Electron Microscope (SEM) with the help of built-in Energy Dispersive X-Ray Spectroscopy (EDX) was performed with a Hitachi TM3030 Tabletop Electron Microscope. SEM analysis provided the data for the topography and EDX elucidated the elemental composition up to a certain point with maximum 15,000 magnification on one spot. SEM-EDX was used to observe both the surface and the cross-sectional area of the samples. The observation on the surface gave the understanding of the dopant solution spread, thus Sn distribution could be explained. The cross-sectional area observations would define the Sn penetration inside the anode cell to give more understanding about the Sn dopant behaviour.

The surface composition data was investigated further by using X-ray Fluorescence Spectroscopy (XRF), X-Ray Powder Diffraction (XRD), and X-ray Photoelectron Spectroscopy (XPS). XRF measurements were carried out with a Bruker S8 Tiger Wavelength Dispersive X-Ray Fluorescence (WDXRF). XRF can show the qualitative and quantitative composition of the surface, and thickness of the coatings, and coating systems. These XRF capabilities offer great insight for more understanding towards the anode supported cells. Samples were analysed using a Rhodium tube with a voltage of 60 kV, a current of 67 mA with crystal LiF220 and 0.23° collimator.

XRD measurements were carried out with a Bruker D2 Phaser X-Ray Diffractometer with a high-speed LYNXEYE linear detector and cobalt (Co) radiation (1.79 \AA). The XRD patterns have been taken by scanning in the area $2\theta = 30^\circ\text{-}110^\circ$. XRD will elucidate the phase identification of the crystalline compound inside the cell thus explaining the Sn and other elements transformation at molecular level. DIFFRAC.SUITE EVA software was used for qualitative analysis for the XRD scan.

XRF results concentrate on the elemental contents of the cell for the surface analysis. Each element is scanned with different depth results from the surface depending on its differences of energy between the orbital electron shells. The XRF X-ray beam will interact with the atoms inside each element and affect the inner orbital by displacing the electrons from the shells. Figure 42 illustrates An electron from a higher orbital replace the vacant sites on the lower orbital shells nearer to the nucleus, to stabilise the atom again (fluorescence).

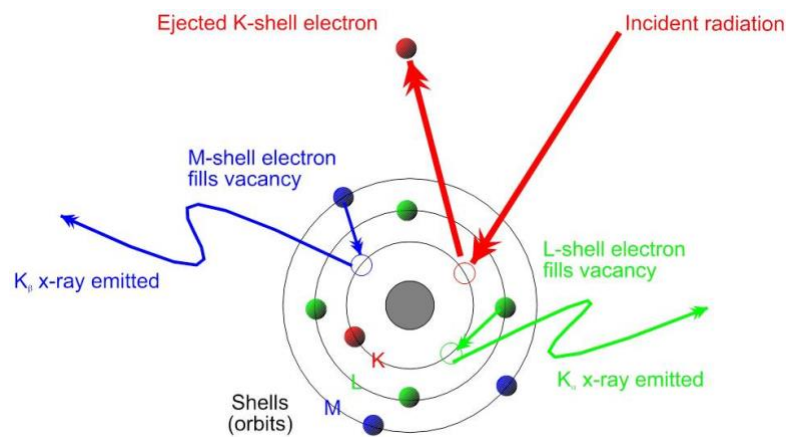


Figure 42 The image model of fluorescence occurrence [<https://www.bruker.com/products/x-ray-diffraction-and-elemental-analysis/handheld-xrf/how-xrf-works.html>, accessed on 22 August 2017]

The displacement can happen because the x-ray beam energy is higher than the binding energy of the electrons. When the displacement happens, the electron that moved to lower orbital shells near the nucleus will lose the energy equivalent of the energy difference

between the two shells. These differences are specific for each element and are used to identify the element and the depth of the scan.

XPS is a surface analysis instrument that is essential for a qualitative and quantitative purposes. Some of the advantages XPS offers include identification of elements present at the surface, concentration of elements at the surface, chemical bonding state of elements, the distribution of elements across the surface and change in composition with depth from the (original) surface [142]. XPS analysis is commonly based on the high spectra results. The spectra result is based on the principle of photoelectron peaks, usually over binding energy or kinetic energy in the spectra diagrams. Each element has specific binding energy pertaining to its electron configuration and spectroscopic rotation. Binding energy is what is being measured in XPS. Meanwhile, kinetic energy is the energy that is released from the atoms when the electrons come out after being shot by the soft x-ray. For example, the two 2p orbital shell is split into two different shells which have different energy, as shown in Figure 43. The same concept is applicable to the outer orbital shells (orbital d and f) of the atoms. The core levels of solids are similar to atomic orbitals although their binding energies will be different (used for making molecules). The number of electrons detected is measured as a function of their kinetic energy which is then converted into binding energy.

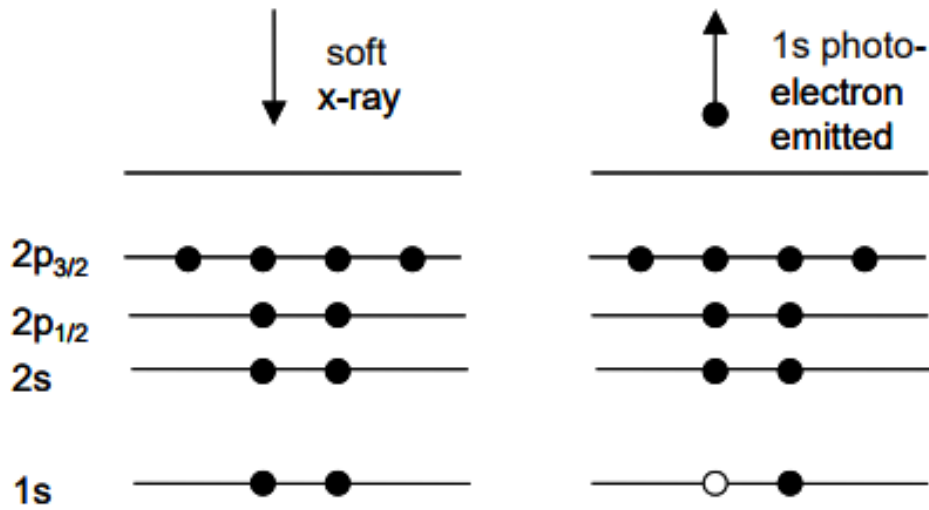


Figure 43 Photoelectron process in XPS [142]

XPS will give back-up data for XRD results on the elemental transformation based on photoelectron energies and Auger-electron spectral line results. XPS measurements were carried out using the Kratos AXIS ULTRA with a mono-chromated Al $K\alpha$ X-ray source (1486.6 eV) operated at 10 mA emissions current and 12 kV anode potential (120 W). A wide scan at low resolution (1400 eV, 5 eV binding energy range, pass energy 80 eV, step 0.5 eV, sweep time 20 minutes) was used to estimate the total atomic % of the detected elements. High resolution spectra at pass energy 20 eV with step of 0.1 eV, sweep times of 10 minutes each were also acquired for photoelectron peaks from the detected elements and these were used to model the chemical composition. The high-resolution spectra were charge corrected to the C 1s peak set to 285 eV. Casaxps software was used for quantification and spectral modelling.

Chapter 4 Cell Testing

4.1 Overview

This chapter presents the results and analysis for each step in this project to give more explanation on the role of Sn within Ni/YSZ cermet anode supported cells, both with hydrogen and with biogas fuel in dry reforming operations. The discussion will start with the preparation and the analysis before covering the actual doping process, the cell testing, and the post-test analysis.

4.2 Preparation of the Cell

Preparation and analysis prior to the doping process provides information on molecular and compositional content of the cells used in this study. It will also to some degree offer insight on Sn distribution before the cell is reduced and tested. Anode-supported full cells Ni/YSZ from the Ningbo Co. were characterised using SEM-EDX on several points to give the understanding of surface composition and topography. Before the analysis, the cell was prepared using a two-step method.

- Clean the cell samples with water
- After using water, clean the sample using ethanol solvent

Several types of cells from Ningbo Co. were used for preliminary observation of the anode surface: LSM full-cells; LCSF full-cells; half-cells (consisting of anode substrate, anode functional layer, and electrolyte); and anode support (consisting of anode support and anode functional layer). This was done to determine which cell will be used further in the study and to identify any differences on topographical and molecular level.

As shown in Figure 44 below, there were not many differences between the four types of cell regarding the topography. All the cell types have quite similar surfaces. Anode supported cells generally are quite porous to accommodate the fuel gas flow to the triple

phase boundaries near the electrolyte. The cell from Ningbo Co. has a relatively low porosity compared to commercial cells in general, since the cell has not been reduced yet. Another theory is also probably because the company did not use pore former in the manufacturing process thus lowering the overall porosity of the cells.

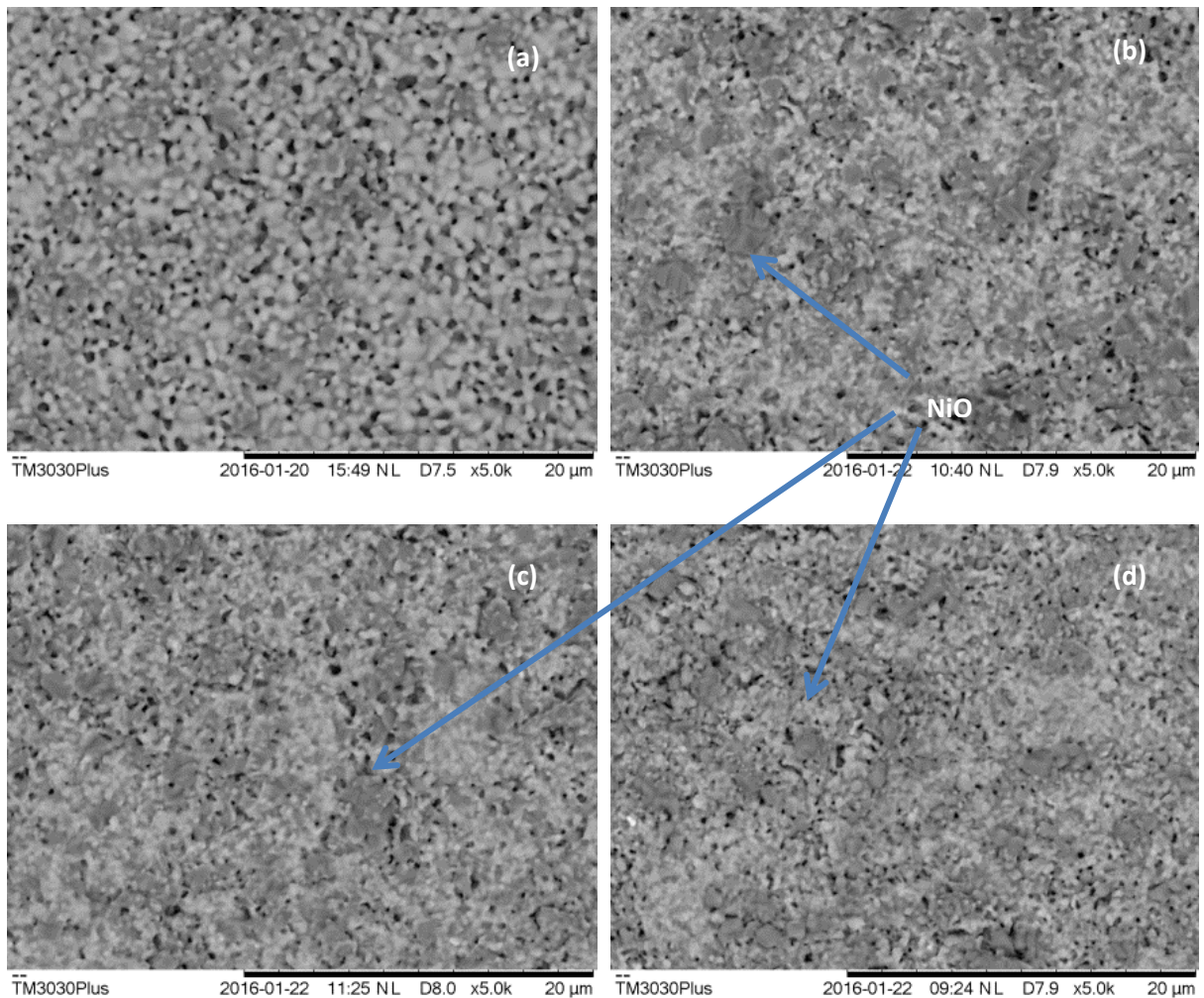


Figure 44 SEM images anode surface with 5000x magnification of a) AS+AFL, b) Half-cell, c) LSM Full-cell, d) LSCF Full-cell

NiO sites are represented in scattered bulk across the whole surface of the anode side, relatively in bigger size than the YSZ sites (Figure 44). Meanwhile, YSZ sites are represented with the brighter colour all over the images. It is a common result because standard Ni-YSZ anode supported cells are made of around 30%-55%-vol NiO powders [143]. Based on the SEM images, Ningbo cells are predominantly covered in Ni sites and

the YSZ sites are distributed around those. According to [143], NiO has the tendency to cluster in Ni-YSZ cermet anode and lead to exceed the percolation threshold of 33% (typical of random distributed three-dimensional space spheres). Ni and pores need to exceed the percolation threshold as it is important to create continuous pores and continuous Ni phase for better performance. There would be some possibilities of Ni sites being electronically isolated and attract Sn and oxygen atoms after doping treatment if the Ni sites are bigger than the YSZ sites. Sn phase that attached to the isolated nickel is proposed to increase the percolation threshold the same as manipulating the distribution of each phase. Higher excess over the threshold of Ni and pores because of additional Sn is expected to leave smaller chance of YSZ phase variation sites, leading to higher overall performance of the cells.

The lack of differences between each cell can be further proven with the XRD analysis. The peaks found on all four of the cells are arguably similar to each other. For this preliminary characterization, a Bruker D8 Advance X-Ray Diffractometer with Cu radiation of 1.541 Å in the area of $2\theta = 10^\circ$ to 80° was used. The instrument being used here was different for the real imaging data because at this stage, the most important thing was to get a glimpse of the contained elements inside different types of fuel cell. The preliminary XRD scanning also helped to determine the 2θ area for further use. The lower and upper limit degree 2θ area for the preliminary XRD scan was 10 to 80° . It seems that the preliminary XRD scan result as shown in Figure 45 was not the complete peaks reading of the cells thus newer range of 2θ area was needed.

The actual imaging data gathering range used for the 2θ area was 30° to 110° , as there were no peaks shown before 30° and some unfinished peaks near 80° (need longer range). Upper limit of 110° was chosen because the limit of the XRD instrument was 120° . The range for

the 2θ area is important to be decided early on as it will further influence the imaging observations and the overall time length for each XRD analysis. If all the peaks of the XRD are included in the scan, it will suffice the purpose of the analysis.

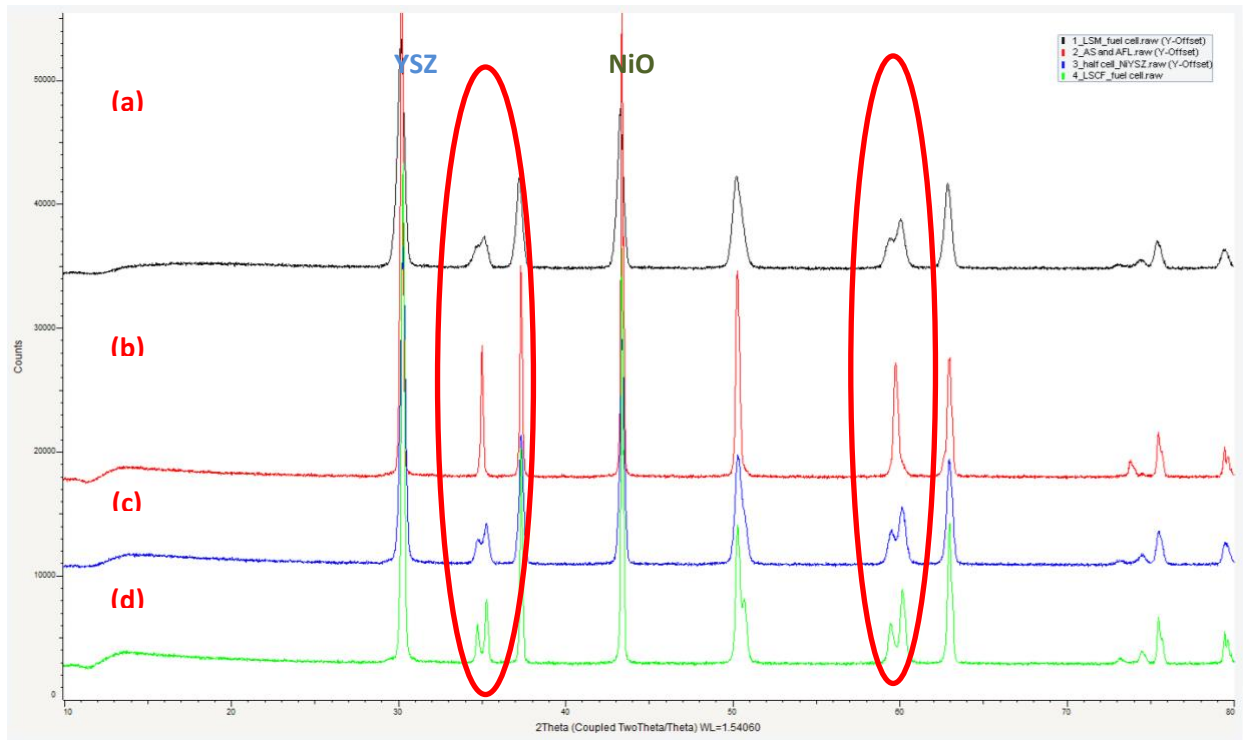


Figure 45 XRD analysis on anode surface a) LSM Full-cell, b) AS+AFL, c) Half-cell, and d) LSCF Full-cell (as supplied)

Based on the XRF results for the different cell types as supplied, the components inside each type shows little differences, especially between the full cell and anode support cell. The full cell (shown in Figure 45 as (a) and (d)) and even half cell (shown in Figure 45 as (c)) have double peaks on 35° and 50° , pointing to different phase of NiO (might be some Ni). The anode support (shown in Figure 45 as (b)) shows one taller peaks compare to the others on the same angle. This is because the anode support had not received further treatment such as adding electrolyte layer and cathode layer like the others. Additional layer means there are some heating up process along the way. It can reduce some of the NiO into different NiO phase or even Ni to some degree. However, the cell relatively has the same

elements with little variation in composition. Thus, it is better to see the differences on the cathode side of the cells to decide which one was going to be used in this study. There are two types of full cell that had been considered at the preliminary stage: Lanthanum Strontium Manganite (LSM) and Lanthanum Strontium Cobalt Ferrite (LSCF).

According to Blum et.al. [144], the LSCF cathode gives better performance at lower operating temperature. Figure 46 displays that at the temperature 750°C, the LSCF cathode gave better performance than the LSM cathode in the same size single SOFC cell. This study will dominantly use 750°C for the operating temperature. Moreover, there is a considerable amount of research using Sn/Ni in anode supported SOFCs using LSM for their cathode side. Yet, there is less observations made on using LSCF combined with Sn/Ni anode catalysts. Thus, it was decided to use the LSCF full cell type for further examining the role of Sn in this study.

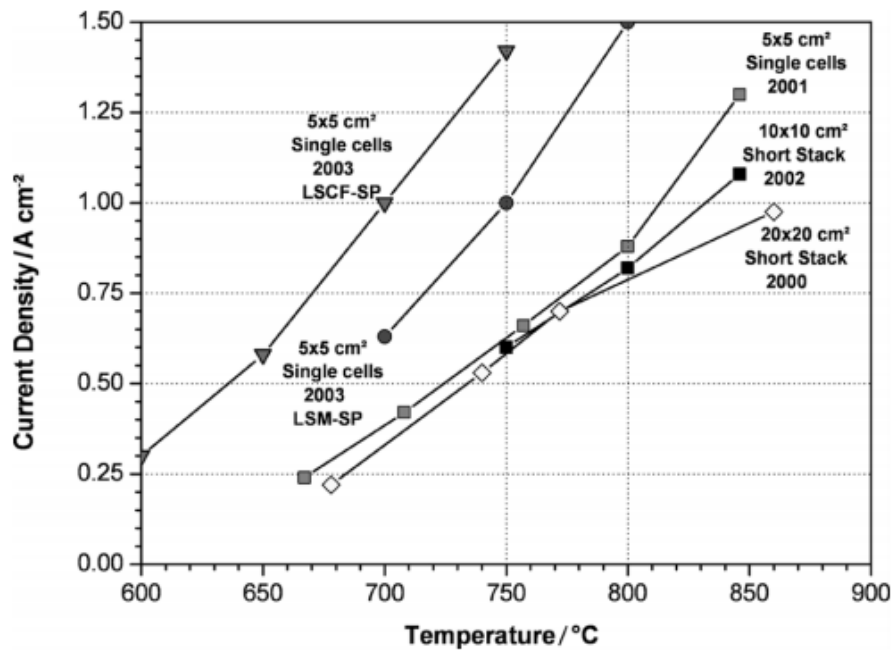


Figure 46 Improvement in cathode screen printing (SP) performance and improved LSCF cathodes by standard Juelich cells [144]

As shown in Table 11, there is less than 5% differences of the main element composition (Ni, Y, and Zr) in all those cell types. Based on the depth of analysed layer for each sample in Table 12, the sample cells are quite like one another. On the other hand, there are massive differences in impurities content between non-full cell (AS+AFL, Half Cell) and full cell types. The impurities are more prominent in the non-full cell type of fuel cells. This is because there would be additional redistribution of molecular phases as non-full cell types would undergo such as electrolyte sintering stage (for AS+AFL) and application of cathode (for AS+AFL and Half Cell).

There are several impurities detected from the raw XRF scans such as: Si, As, Zn, Fe, Cu, S, Nb, and P. The XRF raw scans usually contain less than 0.5% of impurities. Generally, impurities that have less than 0.5% detection on the results need to be checked by their peak result to establish whether they are present or false detection. After comparing the qualitative results with each peak element result, the impurities of the Ningbo cells consist of Hf, Si, Zn, Fe and As. Other impurity scan results from the XRF scan like Cu, Nb, S, and P are always false detection as there were no peaks found on the elements. This is possibly because those elements are close in atomic number thus have slight differences in $K\alpha$ values. The XRF software from Bruker S8 Tiger usually shows the most possible options pertaining to the elements present. Another important observation from XRF results is the depth of impurities from the samples. Table 12 shows that only Hf, Si and Zn can be found on the surface of the samples. Impurities like Fe and As are often too small (in ppm or ppb) in comparison with the Hf, Si and Zn thus they are not being represented in Table 11 and Table 12.

Table 11 XRF composition results on various types of fuel cells (representative for the 95% confidence interval)

Cell Type	Calculated Concentrations (wt%)					
	Ni	Y	Zr	Hf	Si	Zn
AS +AFL	50.66	3.72	43.70	0.47	0.50	-
Half-Cell	50.07	2.27	46.98	0.37	0.52	0.26
LSM Full Cell	48.91	3.84	45.39	0.09	0.66	-
LSCF Full Cell	49.23	2.01	47.98	0.37	0.07	0.03

Table 12 The depth of the XRF scan results for each element

Cell Type	Analysed Layer (μm)					
	Ni	Y	Zr	Hf	Si	Zn
AS +AFL	19.70	45	52	22.80	1.04	-
Half-Cell	16.80	38	45	19.50	0.89	11
LSM Full Cell	17.40	41	47	20.20	0.95	11.40
LSCF Full Cell	16.70	39	45	19.40	0.90	9

The XRF scan results always gave a hafnium (Hf) outcome in quite significant amount for impurities and considerable deep detection in every single cell. As shown in Figure 47, the Hf peak is right on the spot for $L\alpha_1$ energy Hf 7.899 KeV. This peak shows that Hf is a noticeable impurity for the cells from Ningbo company. In nature, hafnium is always found in zirconium ore to form minerals¹². As the SOFC cells contain zirconium in the cermet compound, hafnium is one of the impurities that has higher probability to be present inside the cells. Silicon impurities might come from the pore former used in the manufacturing

¹² http://www.softschools.com/facts/periodic_table/hafnium_facts/344/ [accessed on 16 July 2017]

process and Zn might come from solid state powder synthesis used by the company, either from sol-gel method or precipitation method.

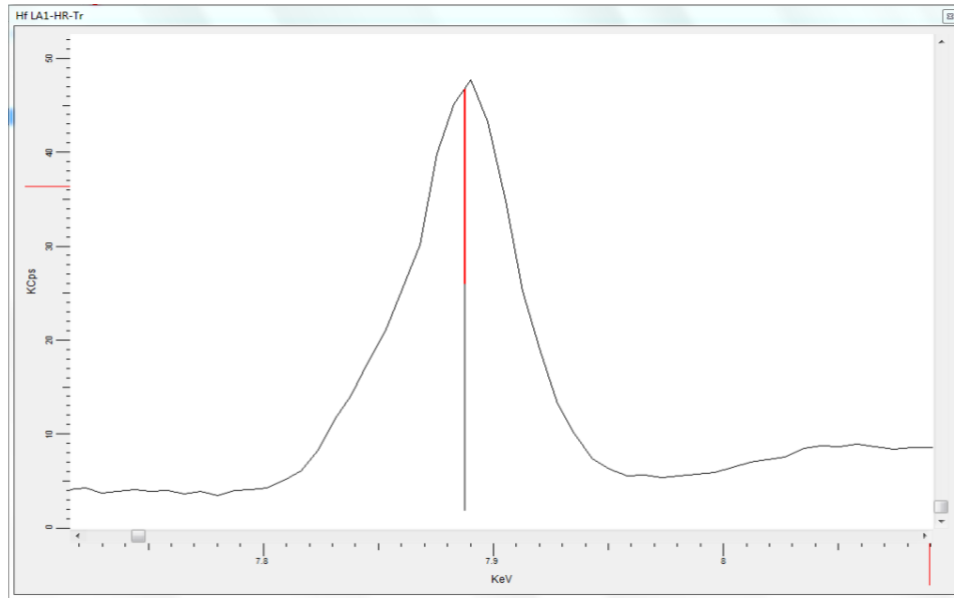


Figure 47 Hf peak scan from XRF analysis

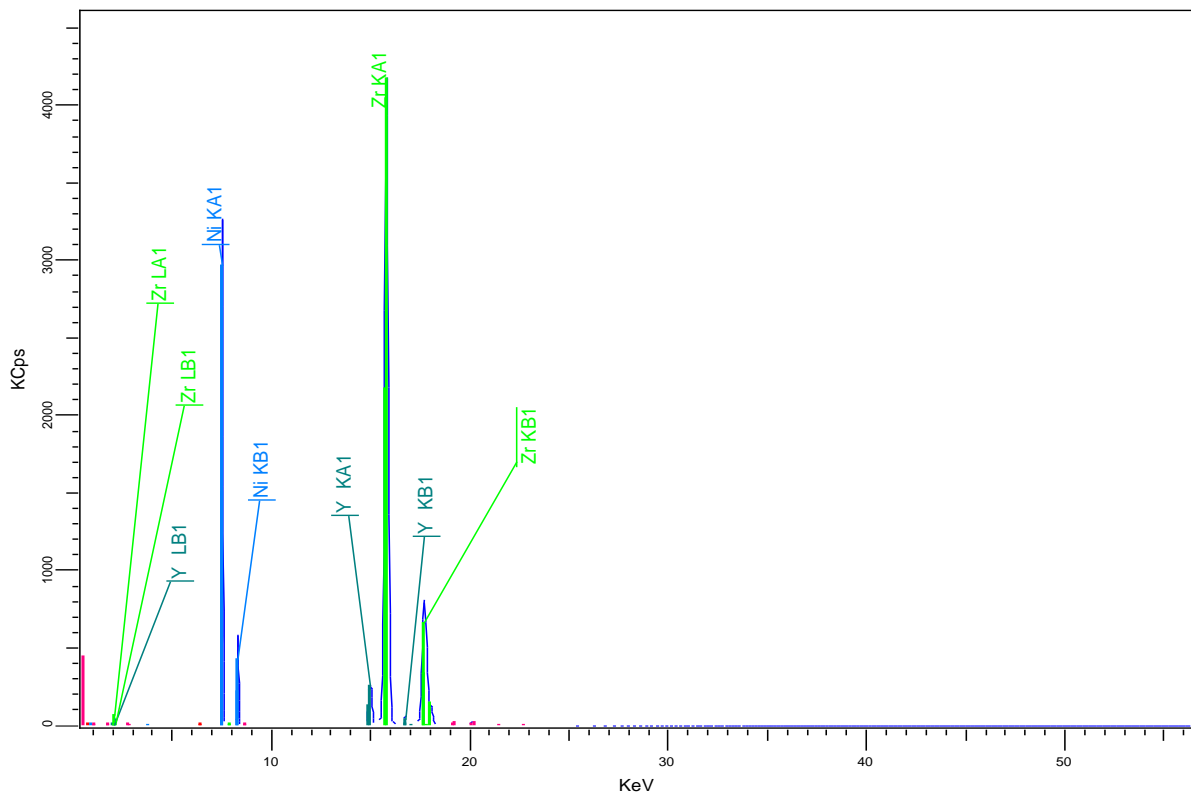


Figure 48 Typical XRF scan result for LSCF type (impurities label removed)

Another characterisation by using the XPS delivered more accurate information about the surface consistency of the samples. XPS is a very surface sensitive instrument and perfect for this study to show whether the theory of developing Sn/Ni alloy on the sample surface can be backed up by the peak results and binding energy found on the cells. Due to the materials used for producing the fuel cells, it was expected that on the reference sample (LSCF full cell) peaks of Ni, O, Y, Zr, and C would be detected. Figure 49 shows the principle photoelectron peaks after charge correction to C 1s at 285 eV on the reference sample.

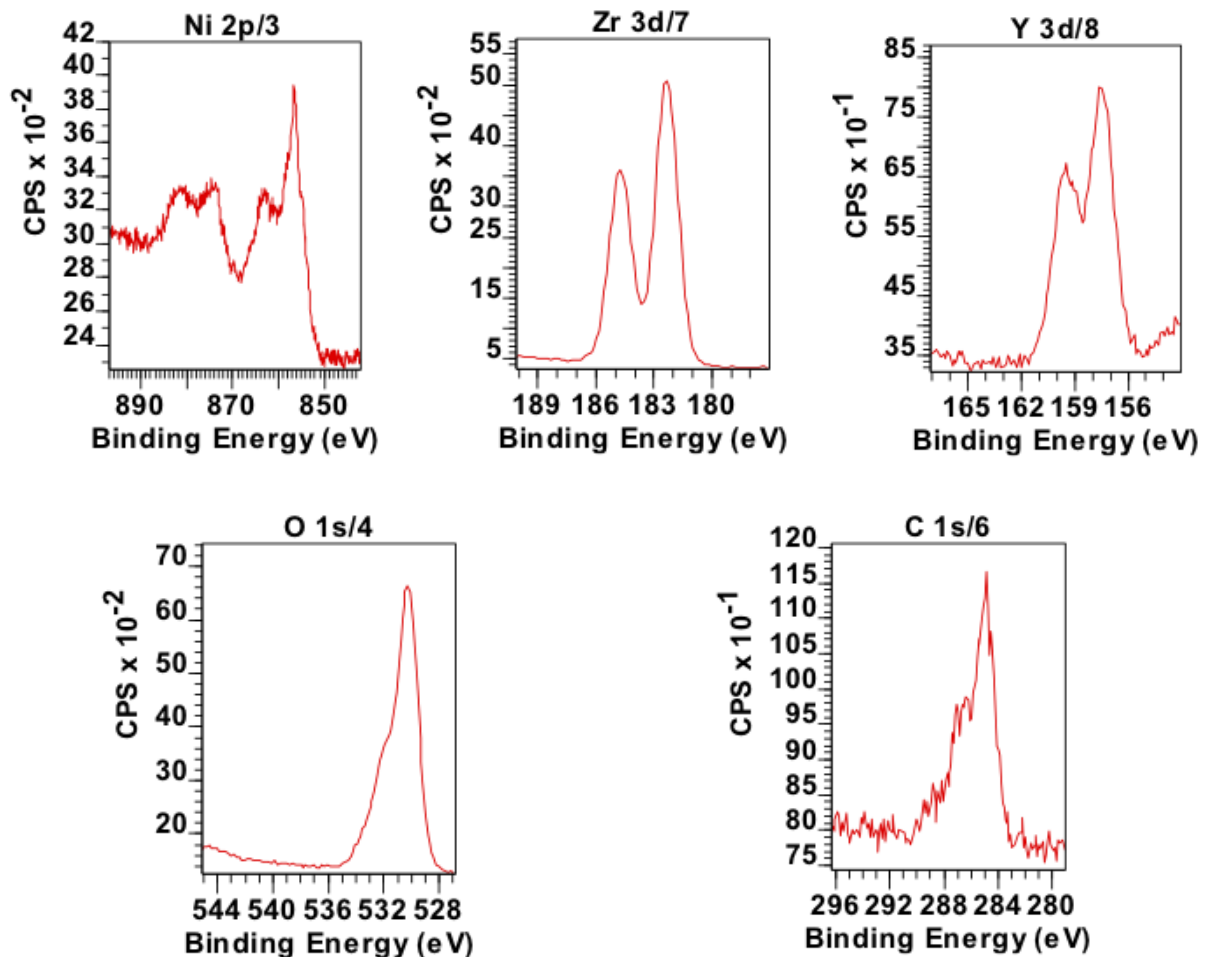


Figure 49 Principle photoelectron peaks of undoped LSCF Full-cell sample (reference for the XPS analysis) from the anode surface

According to the peak positions, Ni 2p is the commonly used split spin orbit component to determine the chemical state of nickel content in XPS. Ni 2p has complex multiplet-split

peaks which contains Ni 2p_{3/2} and Ni 2p_{1/2}. It is also common to contain the satellite for each spin orbit. However, the pure Ni satellite peaks is hard to differentiate with its oxidation state. To analyse the peaks on the reference samples, there are several options that could be taken. The first analysis can be done by comparing the result with the typical image of both pure nickel metal peaks and nickel oxidation state in XPS. There are a few online sources that are recommended by surface analysis experts¹³ aside from the XPS Handbook such as [145,146].

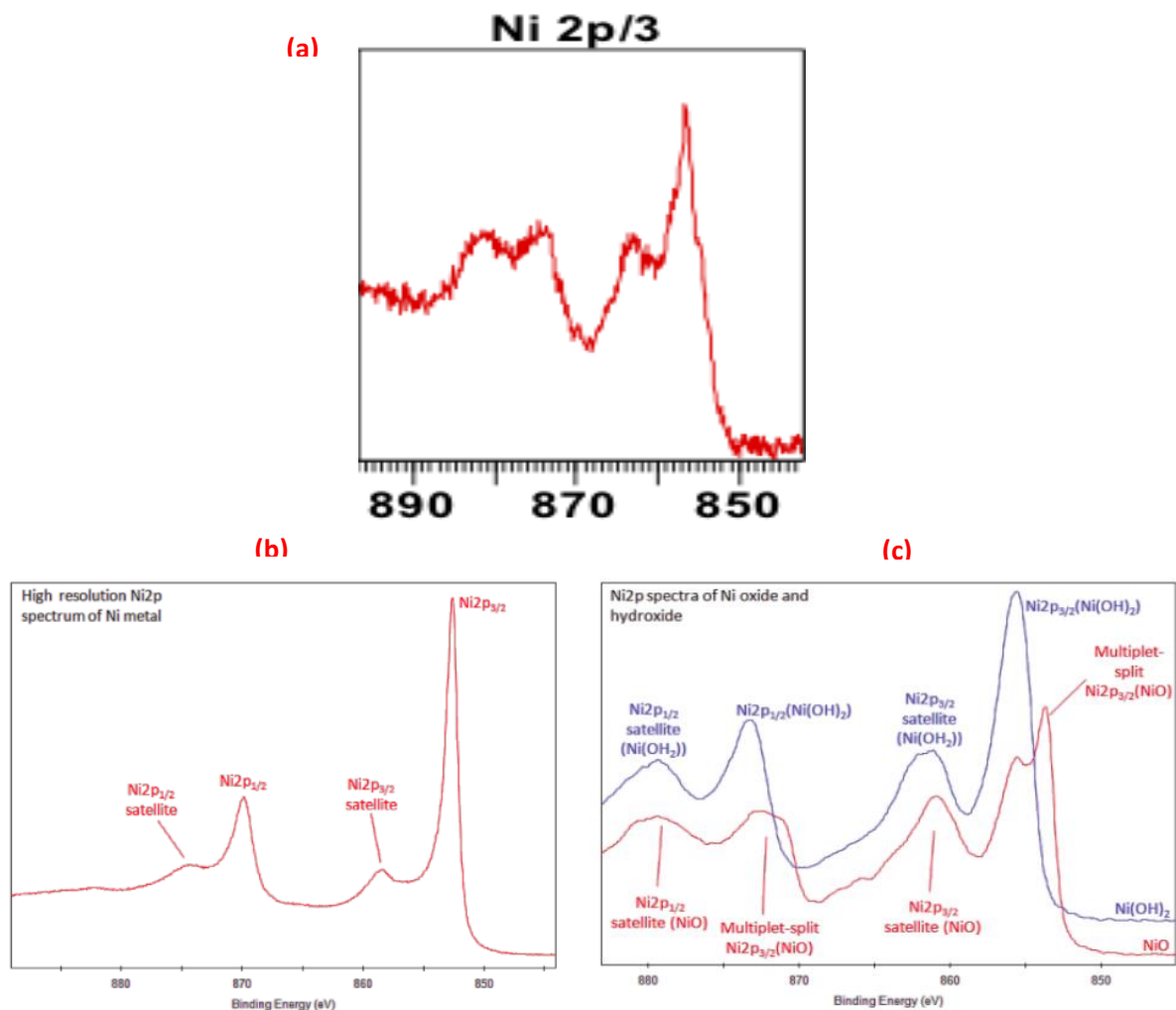


Figure 50 Comparison XPS spectra for one element a) Ni 2p spectrum of Undoped cell, b) High resolution Ni 2p spectrum of pure Ni metal [<http://xpssimplified.com/elements/nickel.php>], and c) Ni2p spectra of Ni oxide and hydroxide [<http://xpssimplified.com/elements/nickel.php>]

¹³ John Grant in XPS Analysis Workshop 2016

As shown in Figure 50, the reference sample for Ni 2p_{3/2} peaks is closer to the oxidation state spectra with the highest peaks at 856.4 eV. To determine the nickel oxidation state, the peak position of Ni 2p_{3/2} will be compared with the data from [146] for nickel on Figure 51. Based on the data value, the nickel oxidation state is mostly NiO with the highest peak around 853 eV binding energy. More in-depth analysis on the XPS results will be discussed in section 5.1.4 and 5.2.4.

Compound	Peak 1 (eV) a)	%	Peak 1, FWHM, 10 eV Pass Energy	Peak 1, FWHM, 20 eV Pass Energy	Peak 2 (eV)	Δ Peak2 - Peak1 (eV) a)	%	Peak 2, FWHM, 10 eV Pass Energy	Peak 2, FWHM, 20 eV Pass Energy	Peak 3 (eV)	Δ Peak3 - Peak2 (eV)	%	Peak 3, FWHM, 10 eV Pass Energy	Peak 3, FWHM, 20 eV Pass Energy	Peak 4 (eV)	Δ Peak4 - Peak3 (eV)	%	Peak 4, FWHM, 10 eV Pass Energy	Peak 4, FWHM, 20 eV Pass Energy
Ni Metal from [1]	852.6	79.6	1.00	1.02	856.3	3.65	5.6	2.48	2.48	858.7	2.38	14.8	2.48	2.48					
Ni Metal - New Line Shape	852.6	81.2	0.94	0.95	856.3	3.65	6.3	2.70	2.70	858.7	2.38	12.5	2.70	2.70					
NiO	853.7	14.3	0.98	1.02	855.4	1.71	44.2	3.20	3.25	860.9	5.44	34.0	3.85	3.76	864.0	3.10	3.6	1.97	2.04
Ni(OH) ₂	854.9	7.4	1.12	1.16	855.7	0.77	45.3	2.25	2.29	857.7	2.02	3.0	1.59	1.59	860.5	2.79	1.4	1.06	1.06
Gamma NiOOH	854.6	13.8	1.40		855.3	0.70	12.4	1.50		855.7	0.36	9.7	1.40		856.5	0.78	20.7	1.40	
Beta NiOOH (3+ Portion)	854.6	9.2	1.40		855.3	0.70	8.3	1.50		855.7	0.36	6.4	1.40		856.5	0.78	13.8	1.40	
Beta NiOOH (2+ Portion)	854.9	2.5	1.12		855.7	0.77	15.1	2.25		857.7	2.02	1.0	1.59		860.5	2.79	0.5	1.06	
NiCr ₂ O ₄	853.8	7.0	1.22	1.30	855.8	1.95	20.5	1.82	1.86	856.5	0.71	24.7	3.91	3.81	861.0	4.50	2.3	1.27	1.33
NiFe ₂ O ₄	854.5	17.3	1.35	1.36	856.0	1.52	38.2	3.03	2.98	861.4	5.41	38.5	4.49	4.50	864.7	3.29	2.8	3.04	3.01

Compound	Peak 5 (eV)	Δ Peak5 - Peak4 (eV)	%	Peak 5, FWHM, 10 eV Pass Energy	Peak 5, FWHM, 20 eV Pass Energy	Peak 6 (eV)	Δ Peak6 - Peak5 (eV)	%	Peak 6, FWHM, 10 eV Pass Energy	Peak 6, FWHM, 20 eV Pass Energy	Peak 7 (eV)	Δ Peak7 - Peak6 (eV)	%	Peak 7, FWHM, 10 eV Pass Energy	Peak 7, FWHM, 20 eV Pass Energy
Ni Metal from [5]															
Ni Metal - New Line Shape															
NiO	866.3	2.38	3.9	2.60	2.44										
Ni(OH) ₂	861.5	1.00	39.2	4.64	4.65	866.5	4.96	3.7	3.08	3.01					
Gamma NiOOH	857.8	1.33	8.7	1.90		861.0	3.20	23.3	4.00		864.4	3.38	11.4	4.40	
Beta NiOOH (3+ Portion)	857.8	1.33	5.8	1.90		861.0	3.20	15.6	4.00		864.4	3.38	7.6	4.40	
Beta NiOOH (2+ Portion)	861.5	1.00	13.1	4.64		866.5	4.96	1.2	3.08						
NiCr ₂ O ₄	861.3	0.26	39.4	4.34	4.31	866.0	4.73	6.1	2.07	2.13					
NiFe ₂ O ₄	867.0	2.27	3.2	2.61	2.66										

a) Binding energies are significant to 0.1eV but an additional figure is added because energy splittings are much more accurate than the absolute binding energies.
b) Assymetric peakshape for peak 1 defined by standard nickel metal sample, CasaXPS peakshape parameter = A(0.4,0.55,10)GL(30)
c) Assymetric peakshape for peak 1 defined by standard nickel metal sample, CasaXPS peakshape parameter = LA(1,1.2,2,10)
d) Metal peak is corrected to Au 4f_{7/2} set to 83.95 eV. All other peaks are charge corrected to C 1s (C-C, C-H, adventitious carbon) set to 284.8eV.
e) Beta NiOOH has a ratio of 2:1 Ni(III):Ni(II). Peak percentages for the 3+ and 2+ portions for Beta NiOOH total 100%.

Figure 51 Ni 2p_{3/2} spectral fitting parameter: binding energy (eV), percentage of total area, FWHM value (eV) for each pass energy, and spectral component separation (eV)[147,148]

4.2.1 Undoped Cell

Undoped cell preparation is not as rigorous as the selection of sample cells to be doped with Sn solution. As mentioned in section 4.1, all the samples would go into a two-step cleaning method before given any further treatment or processing. The two-step preparation was needed to remove dirt on the surface of the cells. The water would act as the preliminary cleaning agent for the dirt, and ethanol solvent would further clean the dirt that could not be removed using water. The samples would be left to dry in air at room temperature for 30 minutes. After the cells dried, they would be weighed to give the base data of the cell before any further doping or additional treatment was performed. As for the selected “undoped” cells for cell testing, the cell would be ready to be mounted to the cell holder after the cleaning steps.

4.2.2 Doped Cell

For doped cells, Sn solution was applied to the cells after the series of cleaning and drying steps. The sample cells were prepared on a ceramic plate for easier treatment and observations. It would be best to use fresh Sn solution for doping the sample and because there was limited amount of solution (around 5 ml), the doped cells were made in batches. To ensure that each batch had received the same amount of solution, the preparation for the Sn solution was done in utmost care and with the same amount of chemical materials up to the fourth decimal (0.0001).

In each drop of Sn solution, there was approximately 1 ± 0.005 mg of pure Sn, with 6 ± 0.0297 mg and 8 ± 0.0275 mg, for 4D and 6D respectively. This analysis will mainly study 4-drop (4D) and 6-drop (6D) dopant solution infiltration inside the samples. According to Troskialina [137], as illustrated in Figure 27, the 4D and 6D Sn dopant using pipette drop

will give the highest performance in dry reforming reaction both using hydrogen and biogas as the fuel. These two will be expected to give the Sn/Ni alloy around 1%wt which concur with Nikolla's [64] results as the highest performance of Sn/Ni-YSZ in steam reforming condition. Moreover, with the pipette drop technique there is a need to calcine every 4 to 6 drops of solution to give the best possible result for the alloying process. A higher number of infiltration drops will cause repeated calcination process before reduction. This might result in a more thorough calcination on the samples or decrease the performance of the alloy as the microstructures are rearranged too much. There is a lack of studies about re-calcination using Sn (except from [137]) for different infiltration compositions, thus this area will need more research for better understanding.

Table 13 Typical base weight for each type of fuel cell, before and after doping

Cell Type	Average weight before doping (gram)	After doping for 4D (gram)	After doping for 6D (gram)
AS + AFL	1.590 ± 0.0202	-	-
Half-Cell	1.589 ± 0.0166	-	-
LSM Full Cell	1.592 ± 0.0358	-	-
LSCF Full Cell*	1.555 ± 0.0276	1.561 ± 0.0279	1.563 ± 0.0275

*used in this study

4.3 Cell Testing

The cell testing is an important stage before continuing with the characterisation of the samples. The cell testing was needed to determine whether the pipette drop technique application in this study for doping Sn solutions gave the expected results. The testing was also to ensure that the infiltration technique is reproducible. If the pipette drop infiltration process was done incorrectly, the cell testing would not have shown the expected results. It would be expected that the Sn/Ni-YSZ cells have higher performance both on using hydrogen and biogas as fuel in 750°C in comparison with the undoped Ni-YSZ cells.

4.3.1 Preparation Before the Cell Testing

The preparation before the cell testing mainly consisted of checking the system, programming the solartron software, and troubleshooting for the rig system. The doped cells were mounted into the cell holder before being fixed inside the fuel cell rig systems. Mounting the cell into the cell holder usually took 1 to 2 days to ensure that there were no micro holes for the prospect of air and fuel leaking from and into the cell holder. Troubleshooting for the leakage was done by using neutral helium gas and a bubble test flow meter. At room temperature, the helium was set to flow into the system at 20 ml/s before heating up the test rig. During the heating up, all the gas flow was turned off and the connection between the test rig and the mass spectrometer was left open. This was to ensure that the silver paste would form a dense silver seal around the cell. The heating rate was 5°C/min from room temperature up to 750°C. This heating rate was chosen based on [137] and the research reported therein about the effect of heating rate on the SOFC performance. The ideal technique according to [137] is using a rapid heating rate to simulate the test as similar as the real SOFC system applications. Yet, if the heating rate was too fast, there would be a higher chance of cell and seal cracks during the test. A slower heating rate would result in inefficient operation. Thus, to compromise the minimum cell and seal cracking possibility with efficiency, 5°C/min was deemed to be the optimum rate.

After reaching the temperature of 750°C, another bubble flow test was to be done before connecting the gas line into the mass spectrometer line. If the bubble test results at operating temperature had less than 20 ml/s, the cell was identified as leaking. It is not recommended to cool down the SOFC system (to apply another silver seal paste) after the first heating up process in the rig because it would result in worse cell condition and performance than

continuing the leaking cell testing. Even if the performance from the leaking cell did not deliver the optimum result, it was still better than to redo the process by cooling down first.

Another problem that possibly occurred during the heating up stage was seal delamination. The silver seal for mounting the cell experienced “thinning” occurrence during the heating process to reach the operating temperature at 750°C. Despite silver having a high melting point at 962°C, the thinning period during heating was often found when the silver sealant did not have sufficient thickness, especially for relatively long hours of usage. This was the main reason for applying 2-3 layers of silver sealant applications during the preparation period.

Stevenson [149] reported that silver seals were unstable especially in a dual atmosphere of H₂-3% H₂O on one side and air on the other side at 700° C. He also reported that silver was stable in an air-on-air configuration on both sides for 100 h at 700°C. The operating condition in this study did not use steam on either side of the electrodes because of the dry reforming system. If there was any H₂O formed during the operation, it would be much less than 5%. The possibilities for the cause of the silver sealant thinning are due to its high vapour pressure and high thermal expansion (CTE $\approx 20 \times 10^{-6} \text{ K}^{-1}$) [143].

Aside from the possible thinning condition, silver is the best option for metal sealant. The reason behind choosing silver as the conductor is because this metal will not corrode in air. Silver has a high melting point, high conductivity, resistance to atmospheric oxidation, and is cheaper than gold (Au) or platinum (Pt). Even if gold and platinum have melting points of 1063°C and 1774°C respectively, both metals are inherently much more expensive and not suitable for mass production. Silver will not contaminate the reaction inside the cell rig chamber with silver gas as it has a higher melting point than the operating temperature.

After the heating period to 750°C in air, hydrogen was introduced gradually for the reduction stage and starting the process of cell testing. The gradual introduction of hydrogen was done after introducing the neutral gas into the system. The temperature was held at 750° until the required time needed before the variation cycle began. Helium was chosen as the neutral gas for this study. The flow rates for the reduction period were 21 ml/s and 7 ml/s for hydrogen and helium respectively. The reason behind introducing hydrogen at 750°C is because it will result in higher conductivity for the Ni-YSZ compared to introducing the hydrogen from room temperature during the heating up process [143]. According to the study on different anode reduction condition, introducing the hydrogen at 750°C will result in formation of continuous network of the nickel phase [143]. Meanwhile, the same study also reported that anode reduction during the heating process formed isolated and spherical Ni grains.

A Solartron 1247 was used for measuring the electrical performance of the samples. It is important to set the programme on the software first before turning on the cell rig for the heating process. The solartron programme would then be started at the same time the fuel was flowed into the system (reduction stage). The reduction would be recorded during the Open Circuit Voltage (OCV) period of the cell testing.

4.3.2 Cell Testing Results

The cell testing process was needed to establish several purposes in this study, such as:

- Checking the performance of the doped cell samples to convey the repeatability and reproducibility of our group's infiltration method by pipette drop technique
- Checking the performance of the doped cell samples in comparison with undoped cells (commercial cells), and

- Determine which Sn content would bring the highest performance in the dry reforming reaction

There were several tests being applied to the samples during the cell testing process such as:

- OCV: Open circuit voltage is an important stage in cell testing as the base condition of the cell when there is no current flow into or out of the fuel cell system. The OCV was deemed acceptable when $OCV = 1.1 \pm 0.1$ V and would be expected to reach stable performance after 5 hours or more. If the OCV was unstable after 5 hours, the cell test was terminated. Stable OCV performance indicated good overall conditions. Meanwhile, unstable OCV was related with cell cracks and bad current collector fittings. In this study, the OCV was set for 6 hours at the beginning before continuing with other subsequent test sequences of electrochemical characterisation techniques. A final OCV under hydrogen fuel was needed to determine whether there were cell cracks or not.

- Polarisation Curve (I-V curve) test

The polarisation curve measurements (potentio-dynamic) were performed to obtain the current density of the cell. The voltage was set to reduce incrementally by 25 mV from OCV down to 0.4 V and back again to OCV. The I-V curve measurements also produced the power density (in W/cm^2) measurements of the SOFC cells.

- Electrochemical Impedance Spectroscopy (EIS)

EIS is a critical technique that can distinguish each loss that possibly happens in the fuel cell: ohmic, activation, and concentration losses. In this study, EIS measurements were carried out at 0.7 V and OCV with a frequency sweep from 1 MHz to 0.1 Hz. In this dynamic technique, the amplitude and phase shift were measured from current response over a wide range of frequencies and thus resulting

in an impedance spectrum. The impedance spectrum results would be shown in Nyquist plots.

- Potentiostatic

Potentiostatic measurements were carried out to see the current response when the voltage was set constant over a period of time. In this study, the voltage was set at 0.7 V for about one hour to see the current yield in steady-state potential condition.

All the in-situ characterisations were applied on every cell that was being tested. Even if there were some problems that caused perturbations of the data gathering, the test sequences were usually repeated three times for each test. These data can be used to interpret the performance both for undoped and doped samples. The following in-situ characterisation was chosen to represent the needed information for ex-situ characterisation from the various calculations and interpretations possibilities.

All samples for the cell testing underwent same treatment sequences with the Solartron program. Yet, there would be seemed to show some variations because the nature of fuel cell operations. There were several possible outcomes from the cell testing stages such as:

- Stable run from start to finish. Contains the full results of the testing performance
- Safety shutdown in the middle of the test. Possible to continue with missing results in some area
- Safety shutdown without the possibility to continue. Little to no data obtained

There were two types of fuel being tested in this study, hydrogen and biogas. Hydrogen test would be implemented first for every cell testing runs. This is because the reduction stage occurred at the beginning of the cell testing also used hydrogen gas. The reduction was set

on the OCV stage as it was important not to put any load on the cell before they were completely reduced.

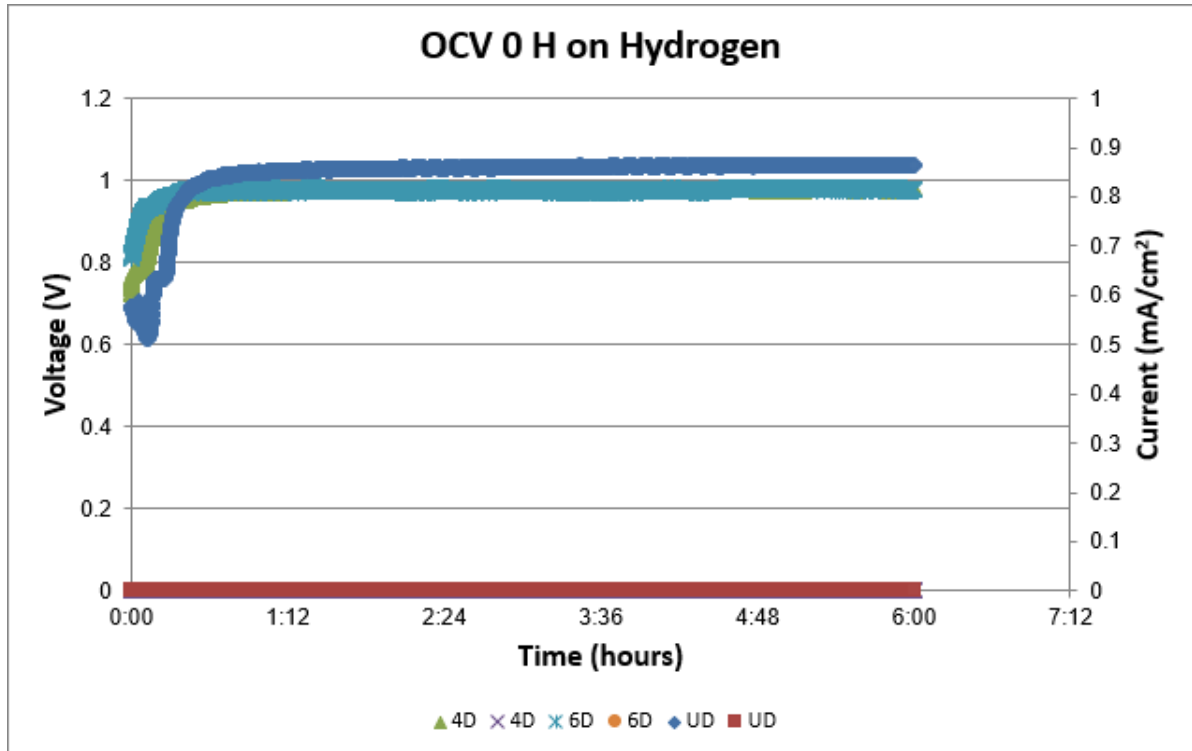


Figure 52 OCV at the starting cell testing in hydrogen fuel between UD, 4D, and 6D cells

Figure 52 and Figure 53 display the OCV states in the beginning of the cell testing in hydrogen and biogas. It immediately shows the differences in voltage between OCV on H₂ and biogas. The fluctuation at the beginning of the cell testing in hydrogen fuel was gradually stabilised after 6 hours. It shows that the undoped cell has higher OCV states in hydrogen fuel. Both 4D and 6D were around the range of 0.99 V to 1.00 V. This lower potential than expected at OCV was due to the reduction stage on the anode surface. All the samples were not completely reduced at this period thus lowering the potential gain.

The cell testing in biogas condition occurred after operation in hydrogen fuel. OCV in biogas was immediately performed after the last OCV step in hydrogen testing. The OCV decreased from around 1.20 ± 0.05 V in hydrogen to approximately 1.06 ± 0.05 V in biogas

for the undoped cell (shown in Figure 53). The doped cells also got lower OCV value, especially on the 6D cell, from around 1.08 ± 0.05 V in hydrogen to 1.03 ± 0.05 V in stable OCV on biogas. This is because the H_2 partial pressure was lower due to the conversion in the biogas reforming. They also show higher OCV at the end of the hydrogen operation (23 hours or more) compared to the beginning of the test.

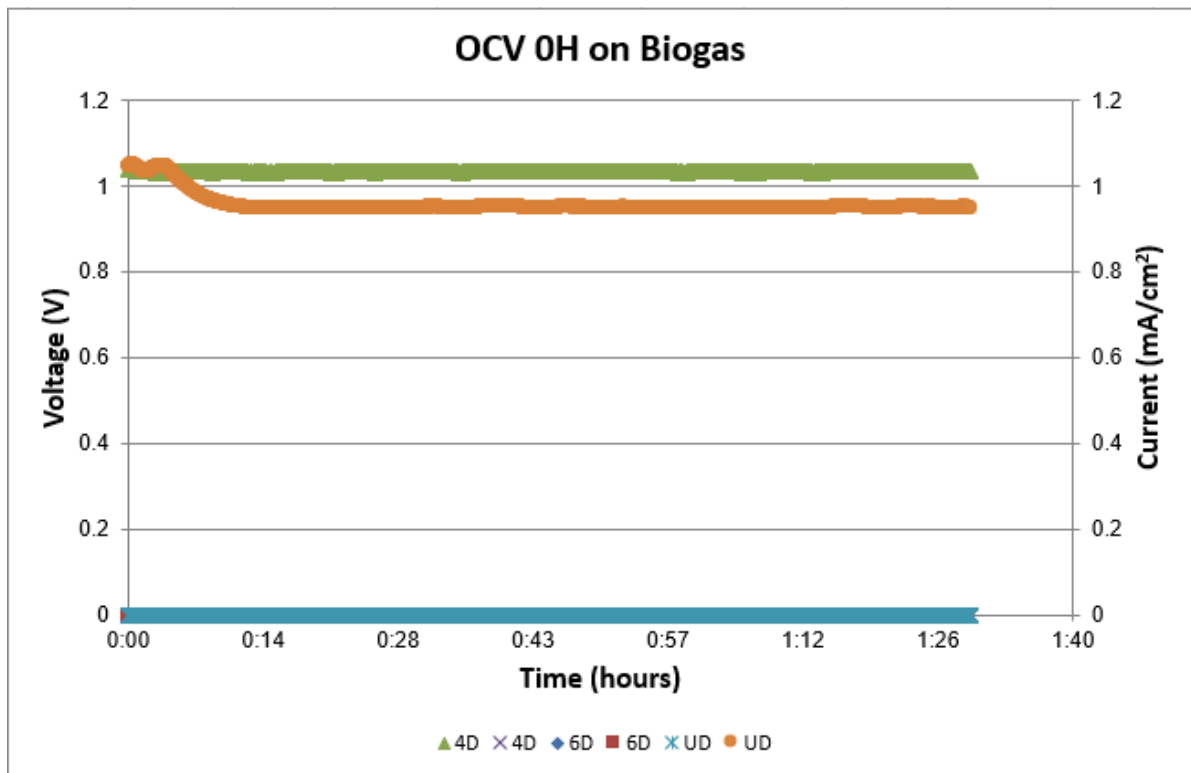


Figure 53 OCV at the starting cell testing in biogas fuel between UD, 4D and 6D cells

In order to see the change in OCV over time, the comparison on OCV in hydrogen at 13 hours of operation is displayed in Figure 54. It can be seen that in general, the OCV has higher voltage in the UD cell compared to doped cells. Referring to the OCV states at the beginning of the biogas operation, all the cells showed higher OCV than during the interim OCV stage in between the polarisation and potentiostatic tests. Considering changing fuel gas flow after hydrogen operation was finished, it might be accounted because at some point

the H₂ partial pressure was higher than during each operation (because the hydrogen and methane gas were present at the same time).

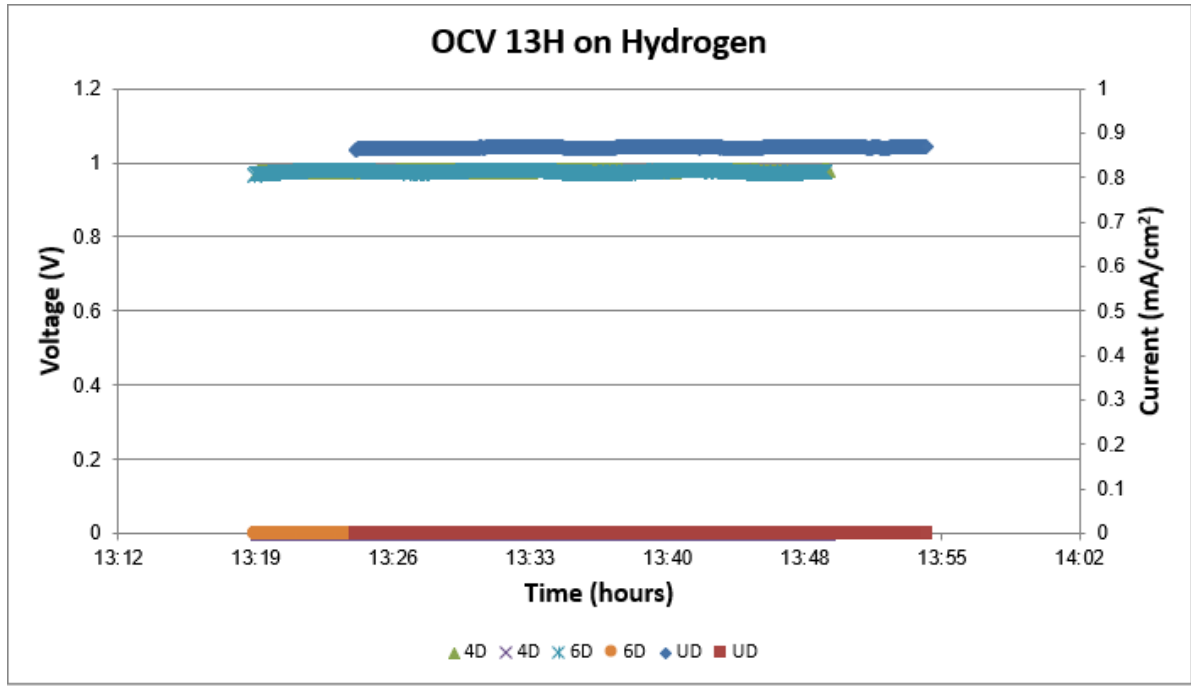


Figure 54 OCV states comparison at 13 hours operation in hydrogen fuel between UD, 4D, and 6D cells

To get more understanding, the OCV in biogas at 23 hours operation is shown on Figure 55. As explained before, the operation between each cell were unique. The 23 hours mark in biogas is selected to show the differences in the durability of the cells after some period and also to see the OCV state near the end of the cell testing in biogas. The OCV state for all the samples were slightly reduced than the OCV state at the beginning of the biogas operation. This is because of the carbon formation on the anode surface especially in the undoped cell case. The doped cells were able to reduce the formation of carbon but not completely diminished the possibility, thus the reduction is not as prominent as the undoped cell.

Figure 55 clearly shows that both UD and 4D were still stable at 23 hours. Meanwhile, 6D cell exhibited a little bit fluctuation at this point. Another interesting fact is also being shown on Figure 55. The OCV voltage on doped cells (4D and 6D) was higher than the

voltage of the UD cells. UD cells had higher OCV voltage in hydrogen fuels but in biogas it was reduced sharply to around 0.96 ± 0.05 V. Sn-infiltrated cells were showing stronger performance and durability when the fuel was changed. The doped cells were showed OCV pass over 1.00 V even after 23 hours operation on biogas.

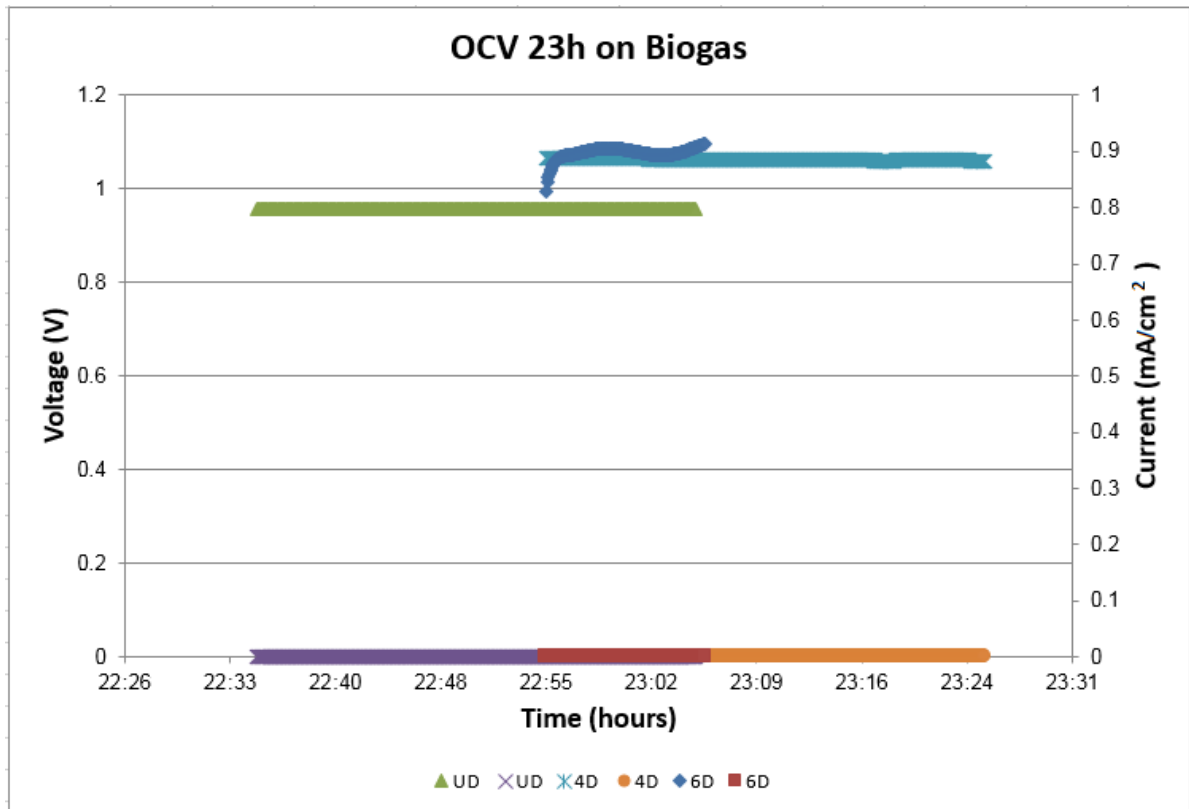


Figure 55 OCV states comparison at 23 hours operation in biogas fuel between UD, 4D, and 6D cells

The IV curve comparison results are shown in Figure 56 for hydrogen operation and Figure 57 for biogas operation. The 4D samples showed the highest performance on both fuels operation. It is worth to note that UD cell underwent a rapid decreased performance in biogas due to the uncontrollable carbon formation on the anode surface. In hydrogen fuel operation, both undoped and doped cells arguably had similar performance regarding the resistance and gas transport losses. Only the 6D cells had slightly higher transport limitation, probably due to blocked porosity.

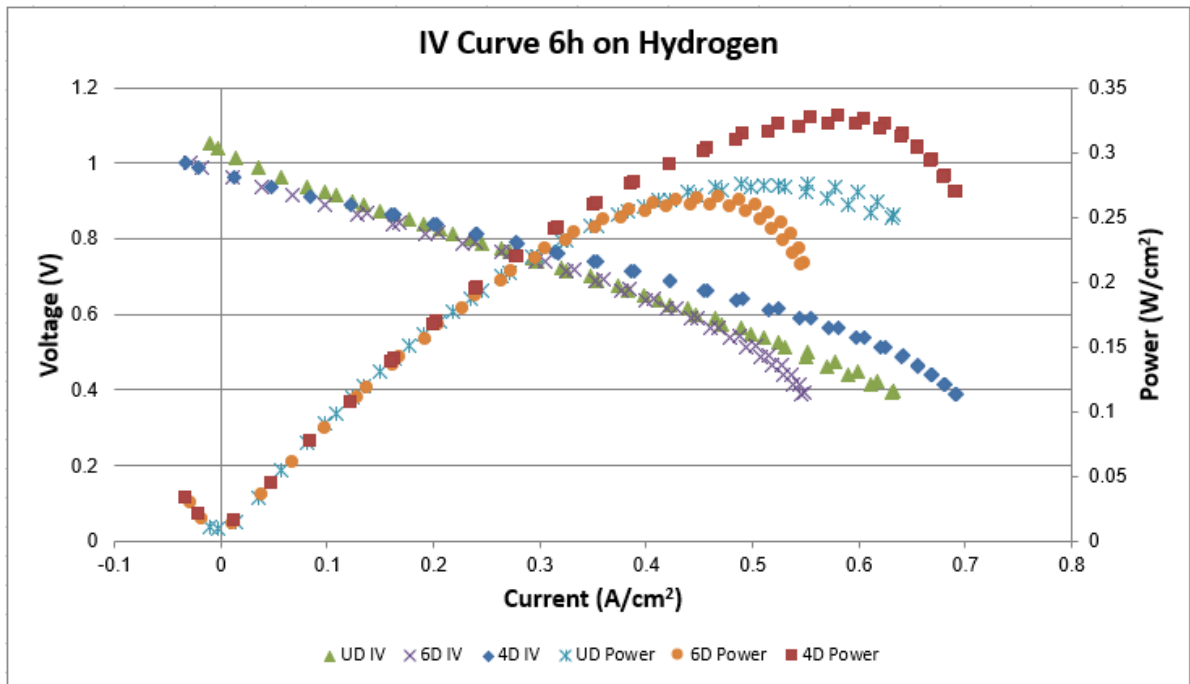


Figure 56 IV curves at 6 hours operation on hydrogen fuel

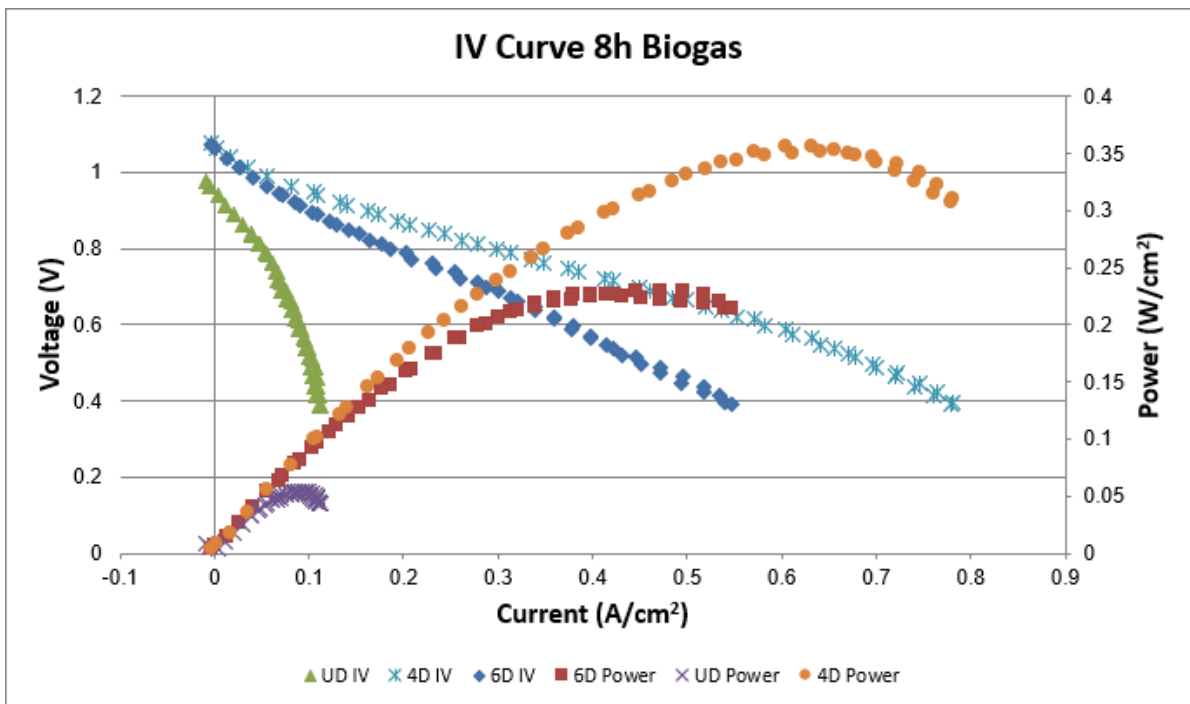


Figure 57 IV curves at 8 hours operation on biogas fuel

However, based on observation in biogas operation the UD cell had carbon covering the anode surface thus making it harder for fuel gas to access the TPB. The carbon formation in the UD cell led to the lowest current density at around $0.10 \pm 0.05 \text{ A/cm}^2$, at the point of

maximum power density. The 4D cell got the highest current density at approximately $0.65 \pm 0.05 \text{ A/cm}^2$ with corresponding power density of 0.38 W/cm^2 . The 6D cell had the highest current density at around $0.48 \pm 0.05 \text{ A/cm}^2$ with the corresponding power density at approximately $0.23 \pm 0.05 \text{ W/cm}^2$.

Because there was a relatively large gap between the 4D and 6D results, another type of doped cell was tested to elucidate the performance differences with different Sn-content. There was a decrease in performance from 4D to 6D thus it gave little to no value to test the 5D cell. Yet, the 3D cell was expected to give better understanding towards the option of Sn-infiltration content on Ni/YSZ. The IV curve on biogas comparison between UD, 3D, 4D, and 6D is presented on Figure 58.

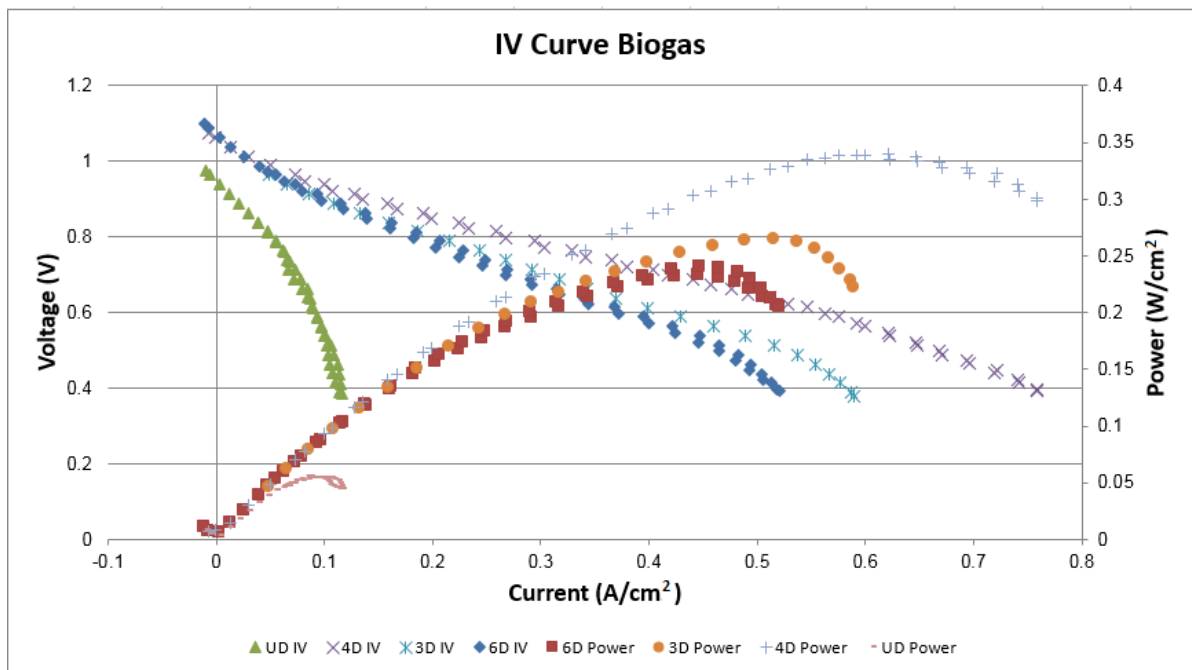


Figure 58 IV curves comparison on biogas operation with the additional 3D cell testing

Figure 58 shows that the 3D cell performance was still better than the UD but lower than the 4D cell. It is therefore safe to conclude that the 4D cell would give the highest performance

in Sn/Ni-YSZ both in hydrogen and biogas fuel. The detailed Sn content characterisation pertaining 4D and 6D cells is discussed in chapter 5.

Figure 59 presents the samples of EIS spectra obtained from the 4D sample. The ohmic resistance of the 4D sample was relatively similar on hydrogen and biogas fuel. The lack of differences in ohmic resistance offers the possibility of stable anode microstructure during the operation of the SOFC, both in hydrogen and biogas fuel. However, there is a significant increase in polarisation resistance observed in biogas operation. This is probably due to the fact that there was poor mass transfer in biogas operation [137]. The increase in polarisation resistance is because of a lower than necessary supply of hydrogen and carbon monoxide present for electrochemical oxidation. This could also be due to slower kinetics for CO oxidation.

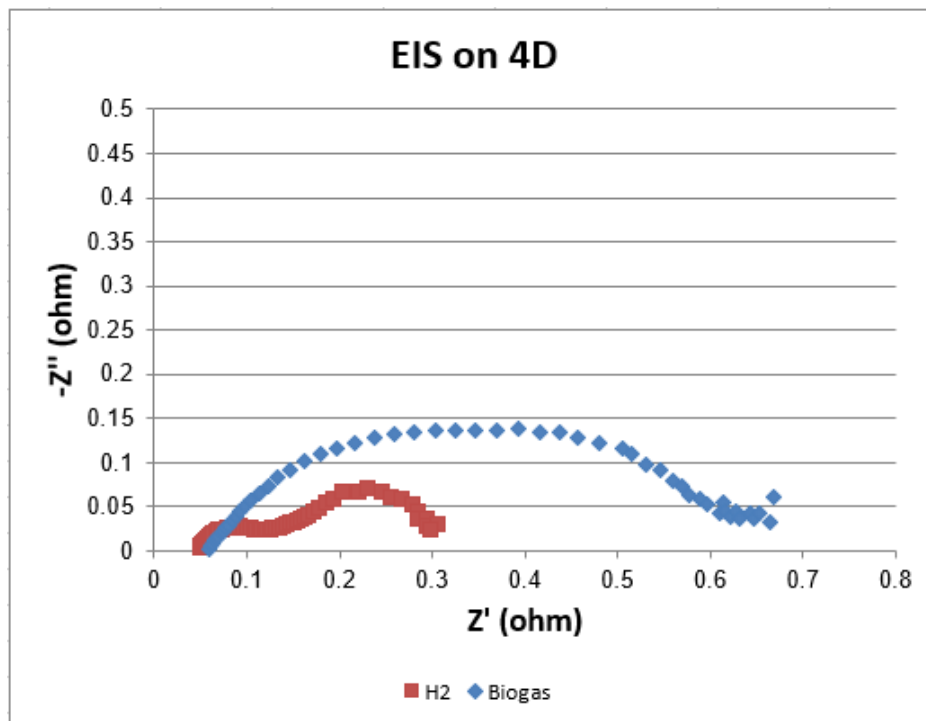


Figure 59 EIS spectra of Sn-infiltrated SOFCs comparison between hydrogen and biogas fuel

The average potentiostatic measurements of the tested cells is presented in Table 14. The undoped cells underwent a massive decrease in current density. The Ni-YSZ without Sn-infiltration showed the effect of carbon formation on the anode surface. Carbon would rapidly form thus penetrating the pores and covering the pathway for the gas fuel to reach the TPB region.

In the case of the doped cells, the additional Sn on the anode surface gives a positive effect for the Ni-YSZ on both hydrogen and biogas fuel. It is proposed that the additional Sn is actually making a “highway” for the gas fuel after the complete reduction. The Sn offers the increased possibility to electrically connect more Ni sites (on the surface and inside the pores) more fuel gas directly contacts both the nickel and Sn catalysts. This condition leads to higher electrochemical oxidation rates which eventually resulted in higher current and power density.

Table 14 Potentiostatic average measurements between UD, 4D, and 6D samples

Potentiostatic		
(A/cm²)		
	H ₂	Biogas
UD	0.344	0.080
4D	0.405	0.445
6D	0.335	0.285

The typical mass spectrometer diagram on biogas operation for both with and without Sn-infiltrated Ni-YSZ are shown in Figure 60 and Figure 61. The diagram shows the relative concentration over time during biogas operation to presents the differences between undoped and doped samples. During the I-V curve and EIS test, hydrogen concentration was

responding accordingly to the current density changes. The electrochemical oxidation of hydrogen happened during the I-V curve measurements thus lowering the partial pressure as the current increased

At the start of the biogas operation, the hydrogen relative concentration for doped cells was decreased from 0.7 to 0.25 at OCV. The hydrogen feed was 21 ml/min with 7 ml/min which accounted with the ratio 0.7:0.3 for H₂ and He, respectively. The biogas feed was 14 ml/min CH₄, 7 ml/min CO₂, and 7 ml/min He which corresponded to the partial pressure of CH₄, CO₂, He of 0.25:0.5:0.25 respectively. The change in hydrogen partial pressure in biogas was due to the supply for hydrogen just coming from methane conversion.

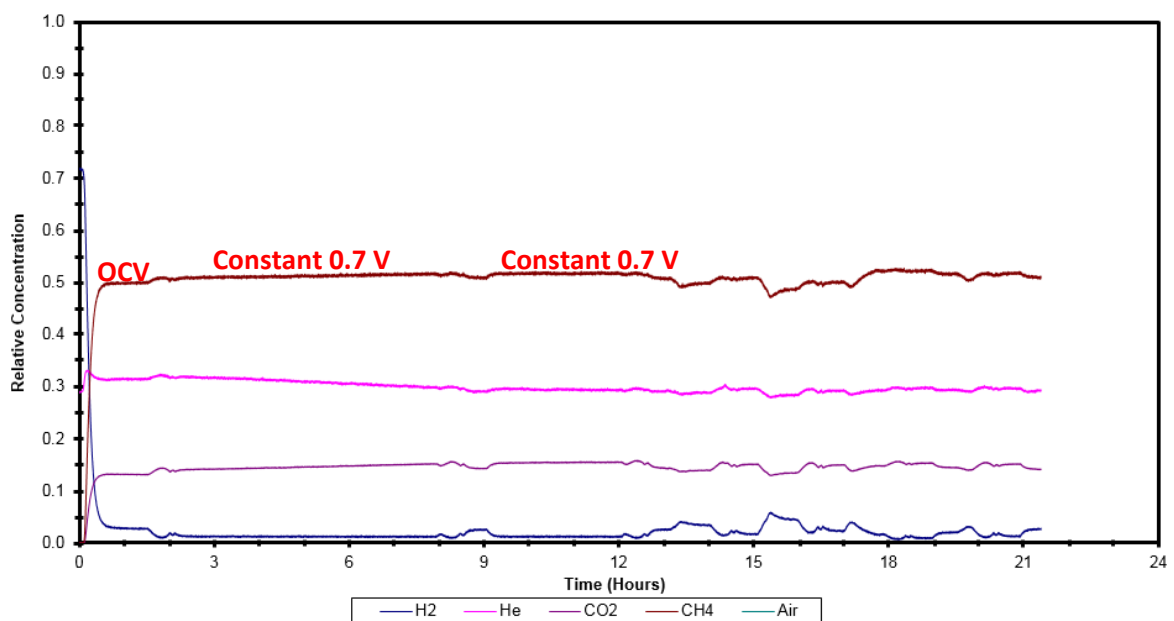


Figure 60 Typical mass spectra of outlet gases of an undoped samples on biogas operation

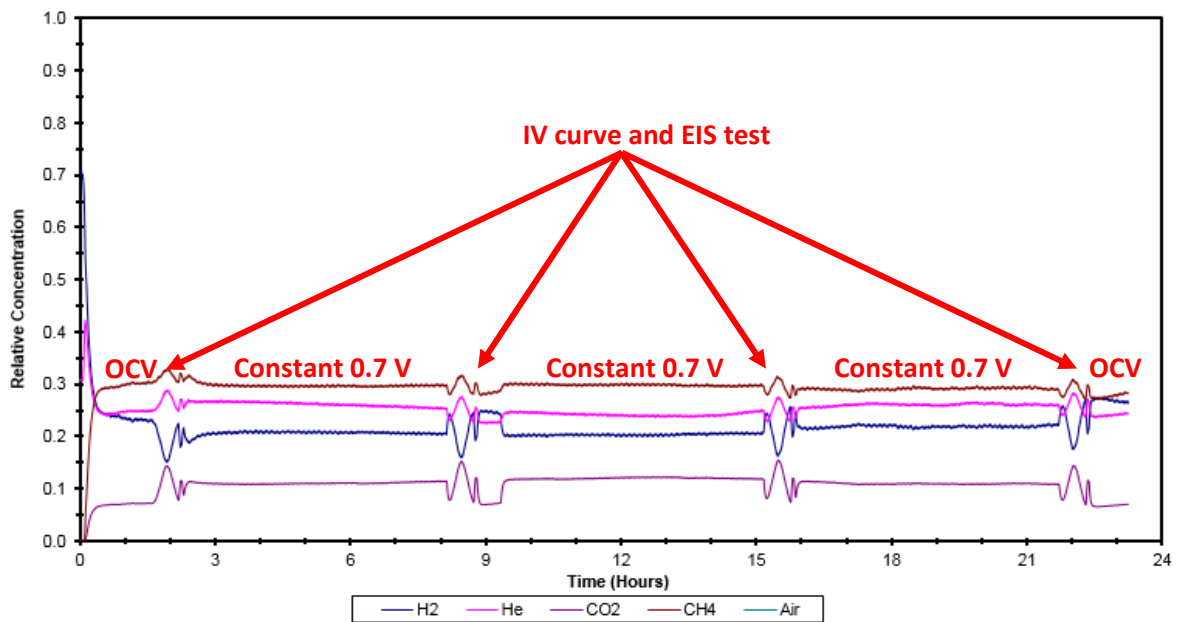


Figure 61 Typical mass spectra of outlet gases of a doped samples on biogas operation

Different hydrogen partial pressure in Figure 60 and Figure 61 shows the differences between undoped cells and doped cells in methane reforming on biogas fuel. The amount of hydrogen partial pressure is highly related with the current gain through the hydrogen electrochemical oxidation. This means that more biogas is converted to CO and H₂ in doped cells than that in undoped cells.

Chapter 5 Cell Characterisation

5.1 Overview

The cell characterisation in a fuel cell can be divided into two major types: Electrochemical Characterisation (In-Situ) and Ex-Situ Characterisation techniques. While the in-situ techniques focus on the measurement of current and voltage, the ex-situ characterisation discusses the cells using structure determination, chemical determination, gas permeability, porosity determination, and Brumauer-Emmet-Teller (BET) surface area measurement. Structure and chemical determination are especially critical in studying new developments of catalysts, electrodes, or electrolytes. According to O'Hayre [150], the structure of the fuel cell materials can be investigated using a wide variety of microscopy and diffraction techniques. Meanwhile chemical composition characterisation of the fuel cell materials can help understanding the physical structure for further analysis.

In this study, the ex-situ characterisation will consist of SEM-EDX, XRD, XRF, and XPS analysis. While the in-situ analysis with the cell electrochemical performance in the previous section gave the background conclusion that introducing Sn on the anode surface helps immensely with the cell performance, the ex-situ characterisation helped understanding the reason behind the improved performance of Sn-infiltrated anode supported SOFC. The samples were characterised both before and after the reduction to elucidate the change in physical and chemical determinations.

There were three types of SOFCs predominantly in the focus of the study: undoped, 4D cells, and 6D cells. All three types were measured carefully to gain significant information about microstructures and percolation using SEM-EDX and XRD. To determine the chemical materials inside the SOFCs, XPS and XRF were used. The impurities inside the samples would be deducted after gathering all the results from various instrumentation.

5.2 Before Reduction

Before reduction (BR) was the stage where the samples had undergone the calcination after the infiltration process but before being reduced by hydrogen for cell testing. For undoped samples, before reduction was the stage after cleaning and mounting the cell into the system. The comparison between before and after reduction is important especially for the change in chemical connections and microstructures.

5.2.1 SEM-EDX

Firstly, the samples went through the SEM-EDX scan to receive some basic data and information on the anode surface morphology and topography. The Hitachi TM3030 Tabletop Electron Microscope that was used in this study had built-in software with three beam observation modes: 5 kV, 15 kV, and EDX. These differences in accelerating voltage focused on various needs for the imaging results. An accelerating voltage of 5 kV does not penetrate too deeply into the sample thus is best used for surface detail imaging. At 15 kV, the electron beams will give the best image resolution and thus this is the most common used observation mode. EDX observation mode is usually used for low contrast specimen and for elemental analysis. EDX can be used as the first attempt to understand the composition of the chemical compounds of the samples. Meanwhile, the SEM can give the image of the interconnected microstructures between NiO and YSZ (undoped) and further on the Sn position on the doped samples.

There were three detectors that could be used for different purposes: back-scattered electrons (BSE), secondary electrons (SE), and a mixed detector. The BSE detector was mainly used for elastic scattering to reflect the scattered beam electrons from the samples. The kinetic energy of the beam electrons would not undergo significant alteration if using the elastic scattering to change its trajectory. The SE detector uses inelastic scattered

electrons for high resolution topography images by using the detector near the sample surface. While BSE images could show the differences in qualitative compositional material, the SE images were used for topographical purposes. EDX images would then back the qualitative images from BSE and SE with quantitative image analysis.

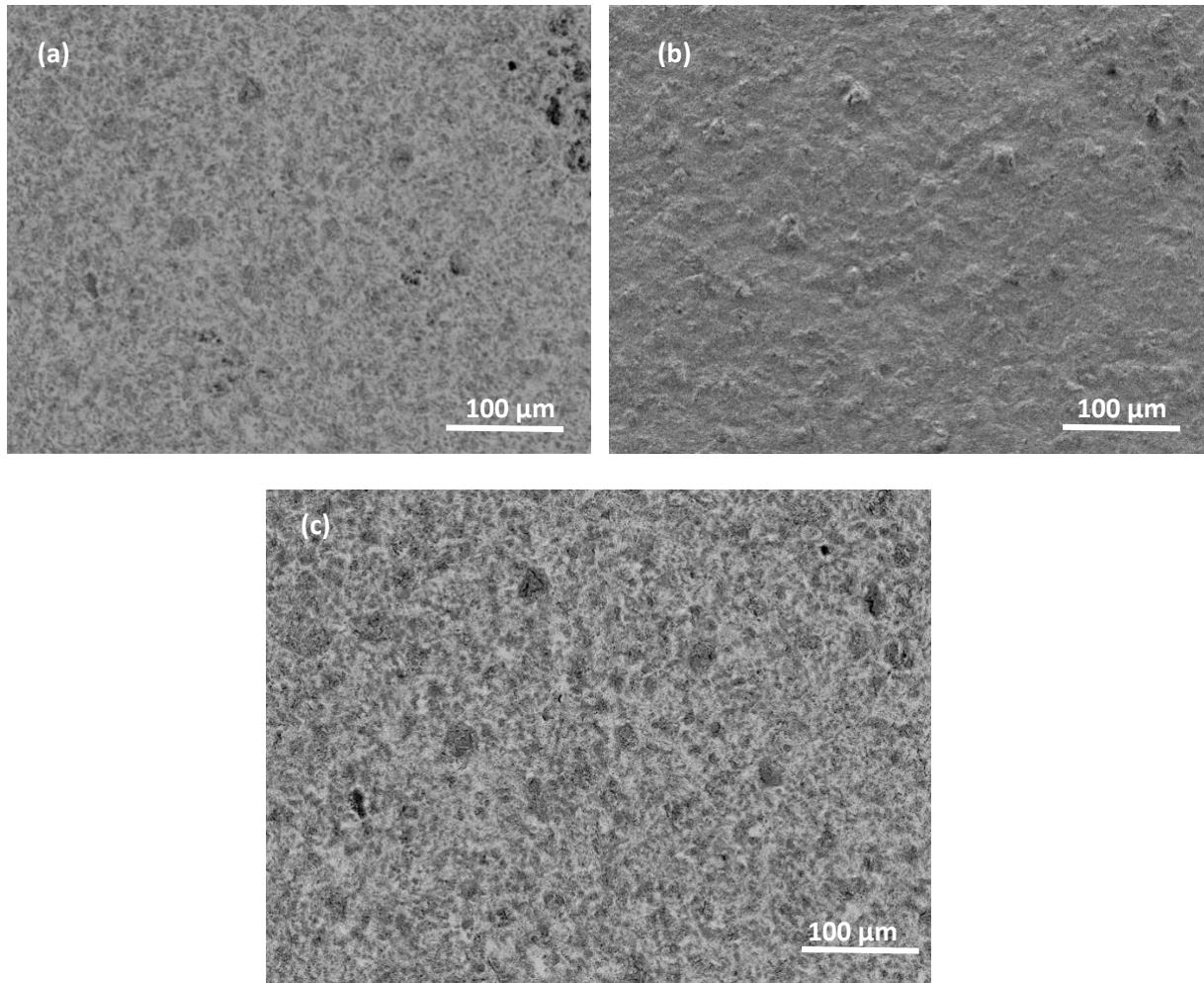


Figure 62 SEM images for an undoped cell using three different detectors in 500x magnification for the same area, (a) BSE, (b) SE, and (c) EDX

Figure 62 shows the different image results for the same area of undoped cell in 500x magnification using the three detectors. As shown on the figure, the BSE image was better in displaying the morphology of the sample surface. It shows the porosity of the sample surface with the different sites as indicated with different shades of grey, expected to be NiO and YSZ sites. The SE image shows the actual topography of the sample surface. It

would help to define the sites for further observation as the undoped cell also could act as the reference. There is some clearly contoured surface on the SE image that might be due to different sites of NiO and YSZ. To differentiate the sites with morphology and topography images, EDX area mapping scan results for the 500x magnification are displayed in Figure 63.

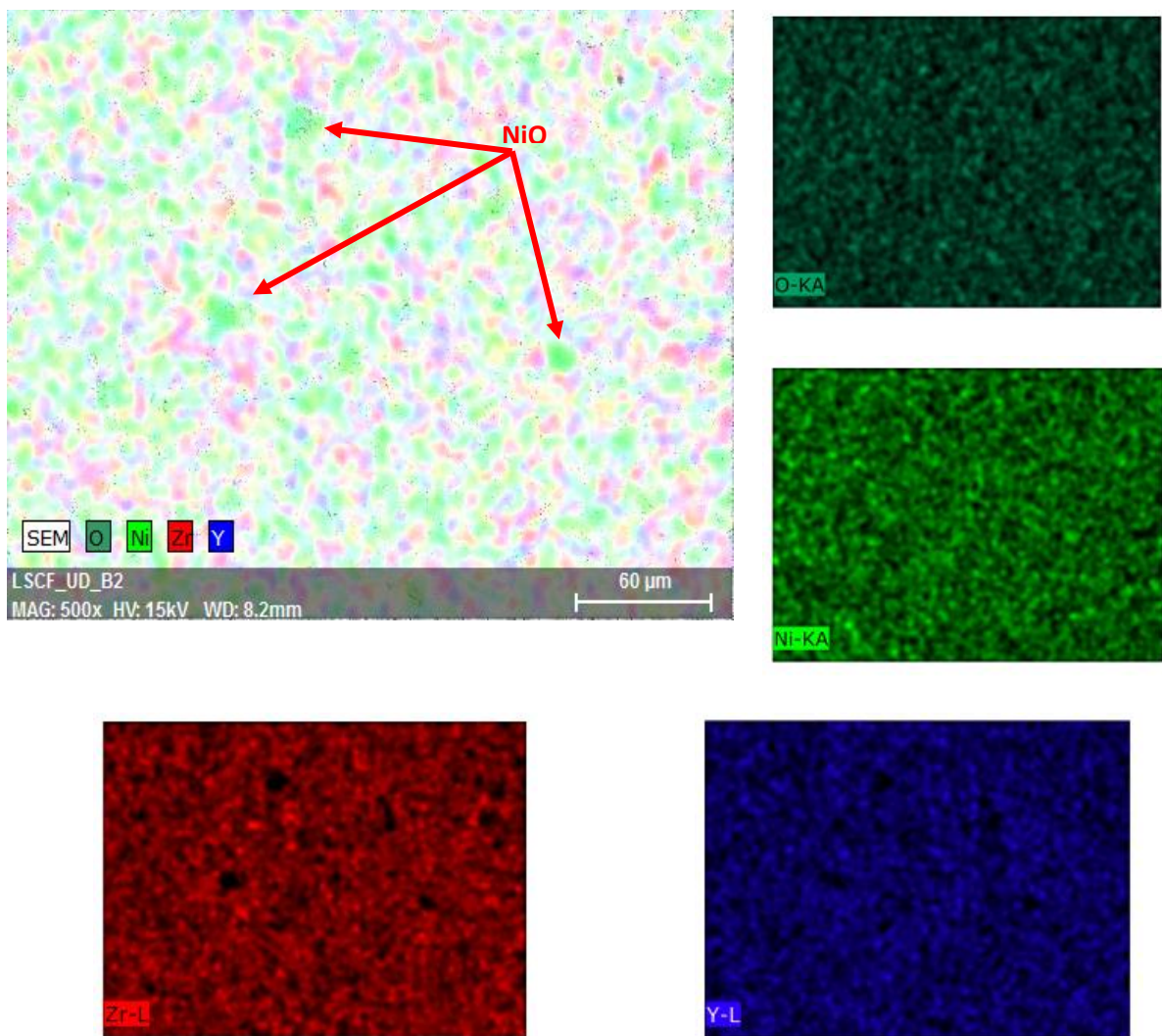


Figure 63 EDX area scan at 500x magnification and 15 kV for undoped cell

The EDX area mapping is the best way to study the distribution of NiO and YSZ sites. As displayed in Figure 63, the EDX scan results are divided into the whole scan and specific element scans. Based on the images, it can be observed that the undoped cell (commercial anode supported SOFC from Ningbo Co.) has relatively homogenous distribution of NiO

and YSZ. It has been established earlier in section 4.1 that the Ningbo cells have a low porosity. Also, the earlier assumption of NiO sites that has the tendency to form bulk sites is confirmed with the EDX analysis. Considering the SE images, it can be deduced that there is the possibility of NiO sites to form small agglomerate sites that make the rough surface.

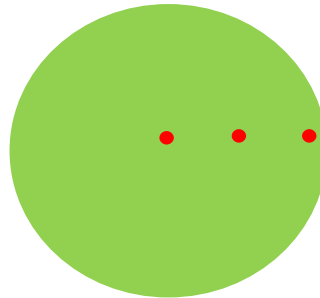


Figure 64 SEM imaging spots

To some extent, the EDX also can give some ideas on the surface elemental analysis. The area mapping scan comes with the ability to calculate the quantitative chemical composition, specific to that area. Observations were made with several undoped samples with each sample being scanned in three random different areas of the cell surface, mainly the centre, the edge, and a random point between the centre and the edge. This was done to get the average distribution of the chemical contents. The average elemental content of the undoped cell in the three spots is shown in Table 15.

Table 15 Undoped cell typical chemical contents for 500x magnification areas

	Atomic Number	Normalised Calc. (wt%)	Atomic Calc. (at%)	Error
Nickel	28	8.950	5.166	0.233
Yttrium	39	16.770	6.930	0.367
Zirconium	40	35.103	11.893	0.800
Oxygen	8	37.713	71.860	2.030

To get the average value of chemical element materials on the surface using the EDX imaging scan was not the most precise way to get the whole quantification results from the samples. SEM-EDX has a limited resolution due to its magnification and the specific area being scanned. The 500x magnification area was selected for the quantification of the

chemical elements because it was deemed being representative of the surface without high error values (can be seen on Table 15).

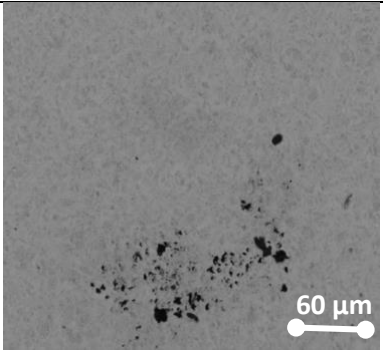
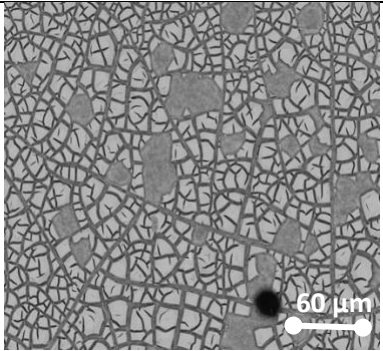
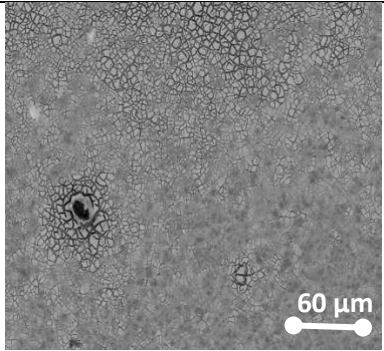
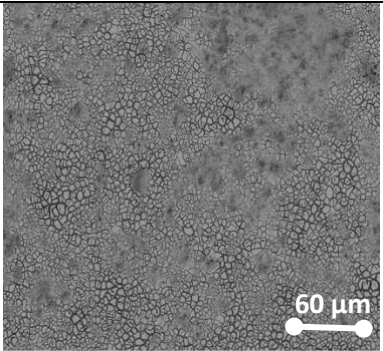
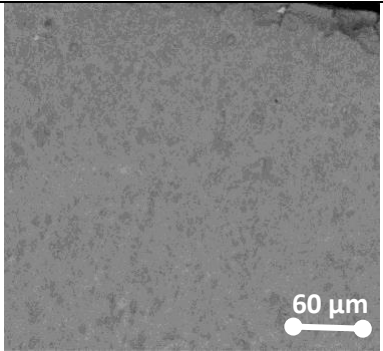
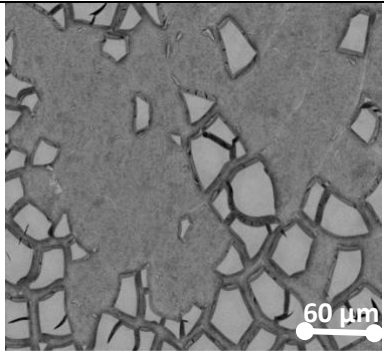
According to Table 15, the nickel content inside the undoped sample is just around 9 wt%. Yet, the NiO content of the sample according to the manufacturer is around 45 wt% and the YSZ content is about 55 wt%. This fulfilled the standard ratio of commercial anode supported SOFC with Ni-YSZ cermet. Thus, the quantification method with 500x magnification area with several spots can be considered acceptable to some extent but cannot be used solely to discuss the chemical elements of the cells.

The next type of samples being observed with SEM-EDX method were the 4D and 6D samples. Table 16 shows the various BSE images for the doped cell in three different spots. The doped samples showed quite some differences in topography and the textures of the surface in comparison with the undoped samples. The BSE images clearly showed some heavy dried bulk sites on the surface close to the edge. The centre spot of the sample showed not much differences on both 4D and 6D compared to the undoped sample. The various state of doped samples after calcination and before the reduction hints at a unique condition of Sn-infiltration using the pipette drop technique.

The pipette drop technique of Sn-infiltration in this study was done by gradually dropping the dopant solution onto the centre spot of the samples surface. The solution would spread out on the sample surface in random, depending on the porosity and the external conditions around the process. Higher humidity and lower room temperature conditions might give different results regarding this process. However, one unique condition for this technique is the pattern of the spread-out solution or better known as surface tension phenomenon. Figure 65 shows how the phenomenon was established during the doping process. This

phenomenon led to the “cracked” sites of what would be expected as Sn oxide sites on top of the anode surface.

Table 16 Various BSE images on anode surface with 500x magnification and 15 kV

4D		
Centre	Edge	Random
		
6D		
Centre	Edge	Random
		

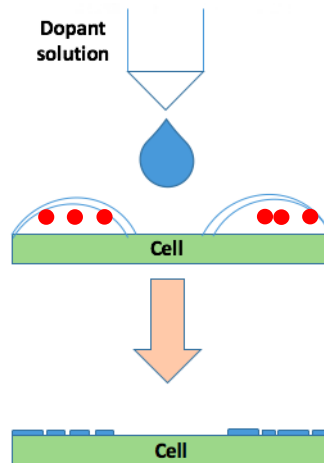


Figure 65 The formation of surface tension phenomenon on Sn-infiltration with pipette drop technique

The surface tension phenomenon that happened on the doped cell can be explained as follow:

- The first Sn-infiltration stage happened directly after the drop of the dopant solution fell on the surface.
- Two things happened at the same time after that, the solution infiltrated vertically through the pores and distributed horizontally on the surface from the drop zone towards the edge of the samples.
- Eventually, the pores which were located in the drop zone could not take up more solution (vertical infiltration) after several drops of solution thus leading the excess solution to move more into horizontal infiltration.
- The ethanol solvent that had been used for the dopant solution evaporated before it could reach the edge of the samples and cover the whole anode surface (ref. Figure 32 in chapter 3). This led to some “layered” half-dried SnCl_2 outspread near the edge of the samples.
- The samples went through the calcination process and formed the “cracked” appearance on top of the anode surface.

EDX imaging confirmed the results of the surface tension phenomenon as the NiO and SnO sites, the same expectation given in study [137], as displayed in Figure 66. This EDX scan clearly shows that Sn is more attracted towards NiO sites after doping and calcination. There were no Sn found on the YSZ sites as shown on the figure below. The oxygen scan can be found all over the surface due to contact with air.

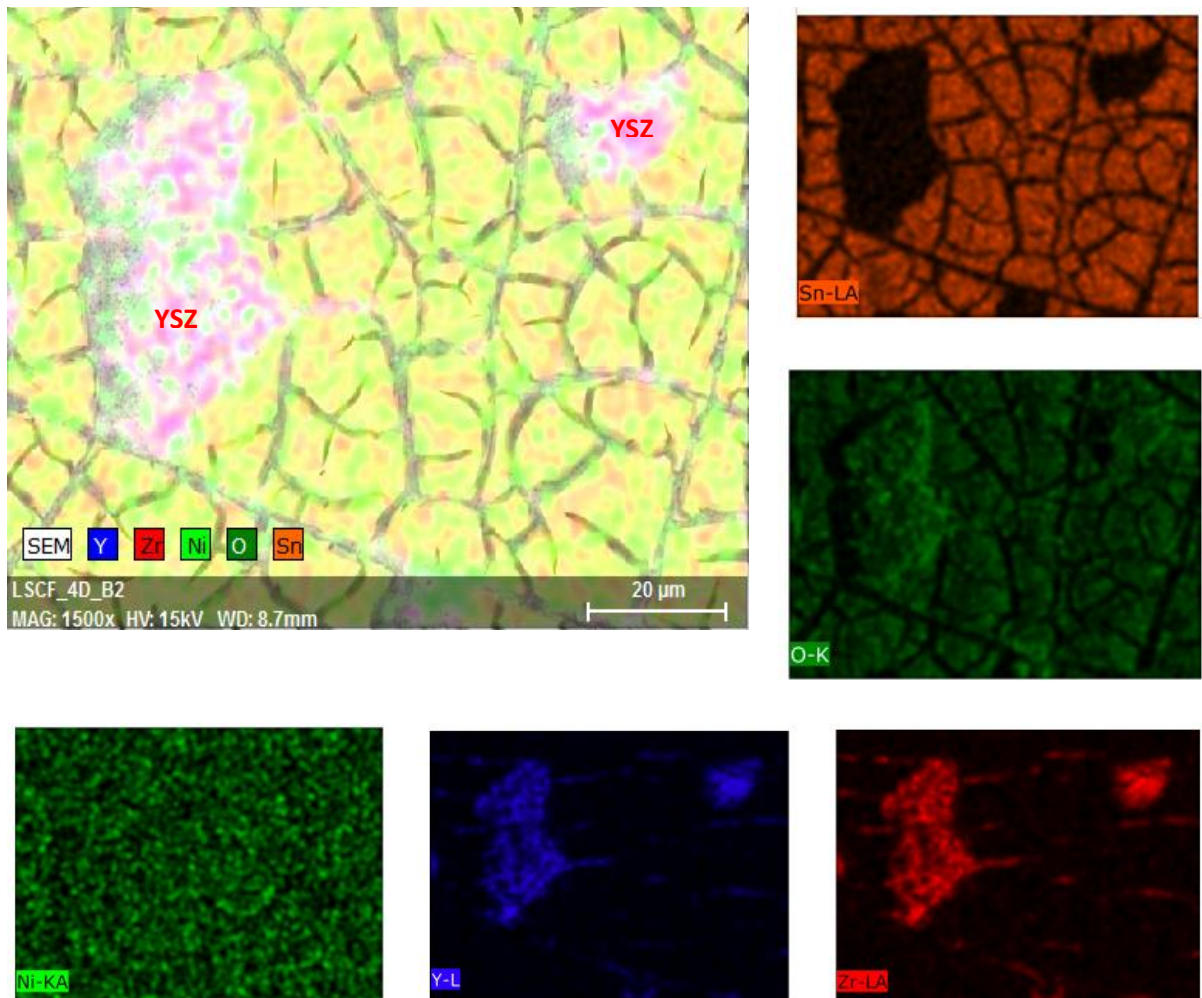


Figure 66 EDX scan of surface area phenomenon and SnO sites on the surface of the anode

The typical quantitative compositions of the doped cell after doping and before reduction is shown on Table 18 and Table 18 for 4D and 6D, respectively. The average calculation was calculated using the same method as the undoped samples. Due to the limited resolution and surface area phenomenon, the chemical compositions of the anode surface from EDX results

were quite different from the theoretical analysis. The SnO bulk sites on top of the surface was decreasing the precision of the EDX analysis and led to the values ranging from 13-wt% to 25-wt% or around 4-at% to 8-at% of tin content for the doped cells. This value is not representing the correct composition of tin on the whole anode surface of the doped cells. Thus, it is necessary to compare this data with the results from XRF and XRD.

Table 17 4D cell chemical compositions of anode surface for 500x magnification areas

	Atomic Number	Normalised Calc. (wt%)	Atomic Calc. (at%)	Error
Nickel	28	0.55	0.34	0.01
Yttrium	39	40.01	16.44	0.80
Zirconium	40	14.08	5.64	0.30
Tin	50	13.16	4.05	0.20
Oxygen	8	32.20	73.53	1.90

Table 18 6D cell chemical compositions of anode surface for 500x magnification area

	Atomic Number	Normalised Calc. (wt%)	Atomic Calc. (at%)	Error
Nickel	28	0.43	0.28	0.01
Yttrium	39	31.40	13.27	0.80
Zirconium	40	11.03	4.54	0.30
Tin	50	25.72	8.14	0.50
Oxygen	8	31.42	73.77	2.20

SEM-EDX can show the chemical content for the first stage of ex-situ characterisation for anode surface analysis. SEM-EDX has the advantage of showing the elemental imaging as to determine the distribution together with understanding the topography and morphology of its microstructures. However, this method needs to be used with other characterisation such as XRF, XRD and XPS to get more precise and accurate data.

5.2.2 XRF

Table 19 and Table 20 display the XRF results on UD, 4D and 6D samples. The content of different samples of the same type were corresponded to each other thus the tables represent

the typical values found on each type. The calculated statistical errors are lower than 0.5% for the main elements (Ni, Y, Zr) and lower than 5% for representative impurities (Hf, Si, Zn). For Sn, the calculated statistical error is ranging from 0.5-2%.

Table 19 Comparison of elements concentration before reduction

Cell Type	Calculated Concentrations (wt%)						
	Ni	Y	Zr	Sn	Hf	Si	Zn
UD	49.180	2.080	48.030	-	0.609	0.051	0.026
4D	50.190	1.990	46.190	0.905	0.687	-	0.029
6D	47.660	2.057	47.650	1.240	0.76	-	0.027

Table 20 Comparison of analysed layer for the elements before reduction

Cell Type	Analysed Layer (μm)						
	Ni	Y	Zr	Sn	Hf	Si	Zn
UD	19.4	45	52	-	22.5	1.05	10.5
4D	19.3	44	51	78	22.4	-	10.3
6D	18.8	45	52	78	21.8	-	10.6

Table 19 displays the comparison of calculated concentrations between the three types of samples in LSCF full-cell. Apart from Sn, the chemical concentration of elements of each type was comparable with each other. The slight shift between each concentration for the doped cells was expected from the calcination and Sn loading effects. The x-ray beam would replace the electron in the orbital shells that is not connected with other elements.

Table 20 displays the XRF analysed layer of LSCF full-cell in several doped variations before reduction. Different from previous Table 12 (in section 4.2) that shows four types of

SOFC planar cells, Table 20 is used to compare different dopant loading from the same type of SOFC. Thus, it elucidates the slight change of the analysis depth more clearly.

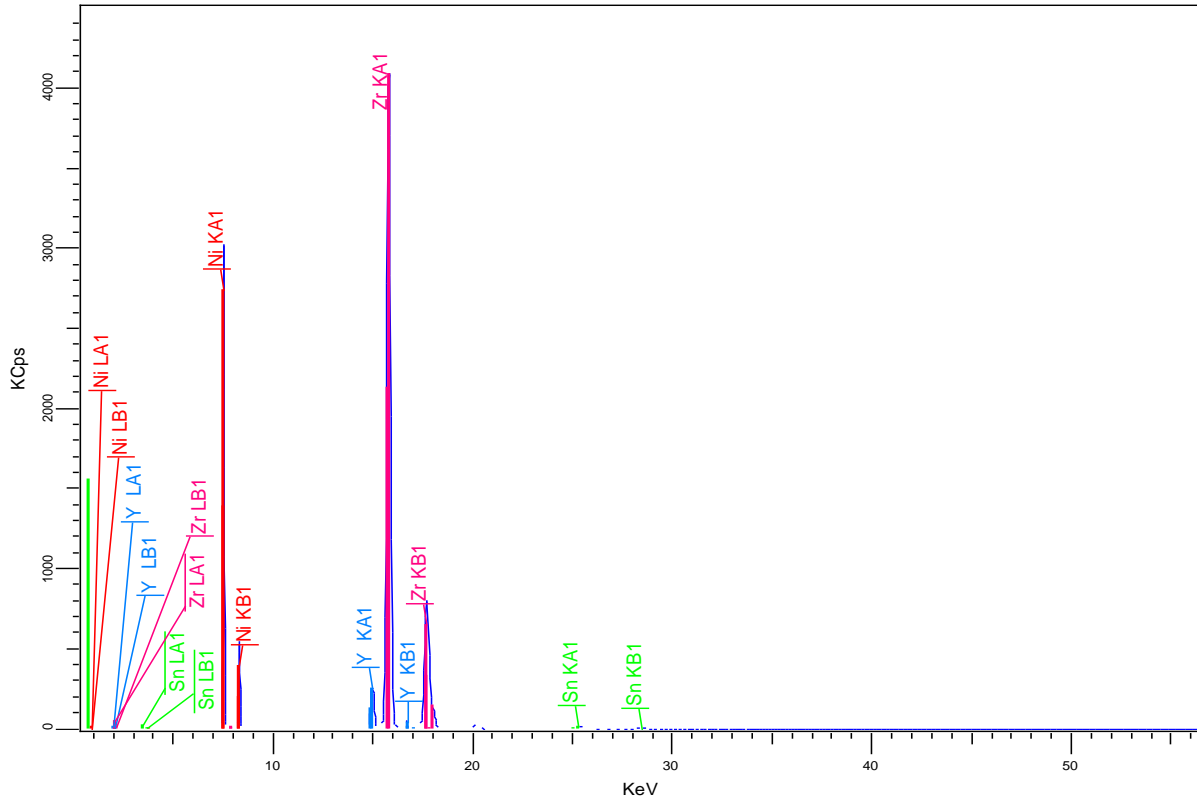


Figure 67 4D sample XRF scan result (impurities label removed)

The tin content (in SnO condition) for the 4D type was around 1 wt% which aligned with the best performance cell testing results (section 4.3.2). Furthermore, this finding also aligned with the literatures [64,137] for the best Sn-dopant performance both in steam and dry reforming which used the same amount of Sn. The 6D concentration according to the XRF was approximately 1.8 wt%, corresponding to the additional two drops of Sn solution. Based on the Figure 57 in section 4.3.2, the 6D cell had better performance than the undoped cell but not as high as the 4D cell performance. This was also agreed with study [64] study that claimed about decreasing nature of methane conversion as the Sn loading increased from 1 to 5 wt%.

In general, there are no obvious differences for the depth of the analysed layer. This is associated with the fluorescence concept of the XRF and can be considered also as the depth of the coating layer on the anode surface. XRF could scan the whole anode surface thus making this instrument an important analysis tool for the ex-situ characterisation. Considering the surface area phenomenon that happened on the doped cells and the low porosity of the Ningbo cells, it was safe to assume that the pipette drop infiltration had sufficient ability to penetrate the cell up to 78 μm from the anode surface. It would be expected to be able to penetrate deeper if the porosity of the cells was higher. This is fulfilling the purpose of loading the Sn dopant just onto the anode surface to get better performance and minimise the carbon formation of dry reforming operating in biogas.

5.2.3 XRD

XRD is a powerful instrument to analyse the chemical connections and interactions between the elements inside the samples. In this study, XRD was used for determining the change on NiO and SnO interactions. Furthermore, XRD was also used for defining the change in YSZ connections within the sample. According to [137], the NiO and SnO sites eventually would transform into Ni and Sn metal. Furthermore, the Ni and Sn metal would form a Ni-Sn alloy that is theoretically the cause of better performance in dry reforming on biogas operation.

XRD produces electrons by heating a filament in a cathode ray tube and shoot the accelerated electrons (by applying a specific voltage) towards a target material. When the electrons have sufficient energy to displace the electrons inside the material inner shells, specific x-ray spectra form. The spectra patterns would then be compared with the database from the software.

To prove the theoretical understanding from DFT calculations [61,64] about Sn/Ni and the proposed reactions [137] in Table 9 in section 2.5, various XRD results are shown below.

Figure 68 displays the undoped cell peak analysis. It was clear that the UD cell consisted of NiO and YSZ (in yttrium zirconium oxide phase) chemical connections. This was expected as the undoped cell compositions before reduction. The XRD spectrum result of the commercial cell of anode support SOFCs before reduction is typical of NiO-YSZ sites.

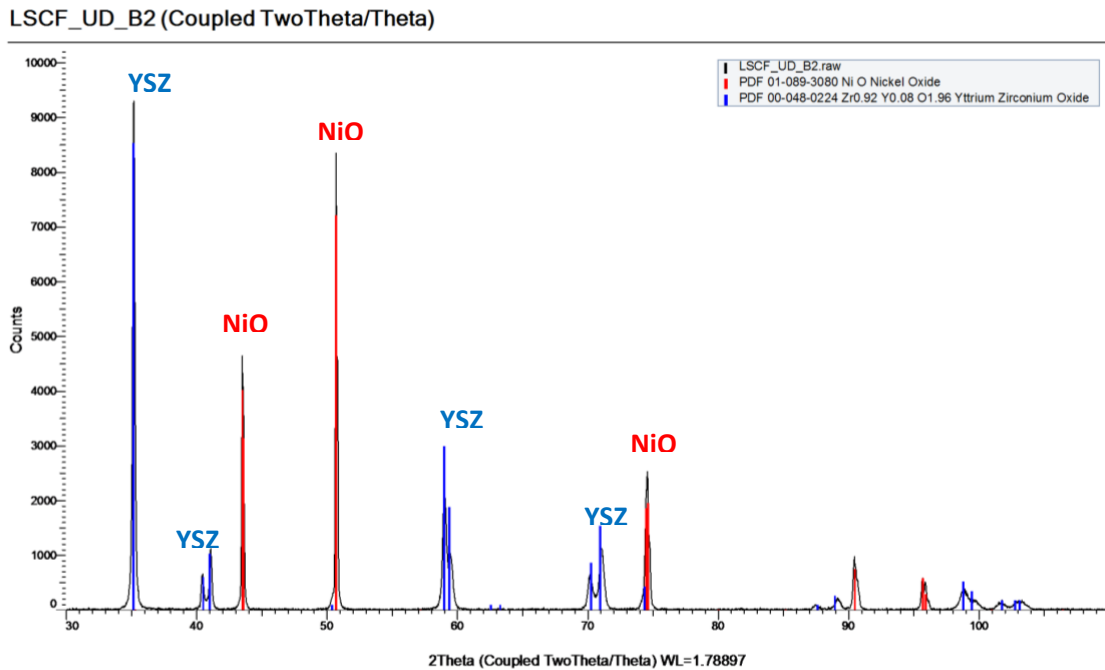


Figure 68 XRD analysis for undoped cells

The XRD imaging for 4D and 6D is displayed in Figure 69 and Figure 70, respectively. The phase matched analysis results clearly show the additional Sn oxidation state on the doped cells compared to the undoped cell. Sn was found in the state of Nickel Tin (IV) Niobium Oxide on the doped cells (according to the DIFFRAC.EVA software). Yet, the spectrum pattern found in the doped cells is proposed to be NiSnO_2 . This conclusion was drawn because niobium was not used in this study and could not be found in SEM, EDX, XRF or XPS results (even as impurities).

The pattern analysis was based on the database of Powder Diffraction Files (PDF), PDF-2 Cards software, whichever had similarities with the samples spectra patterns on the

database. The proposed NiSnO₂ is yet to be added to the database thus made it be recognised as (Ni_{0.1} Sn_{0.7} Nb_{0.2}) O₂.

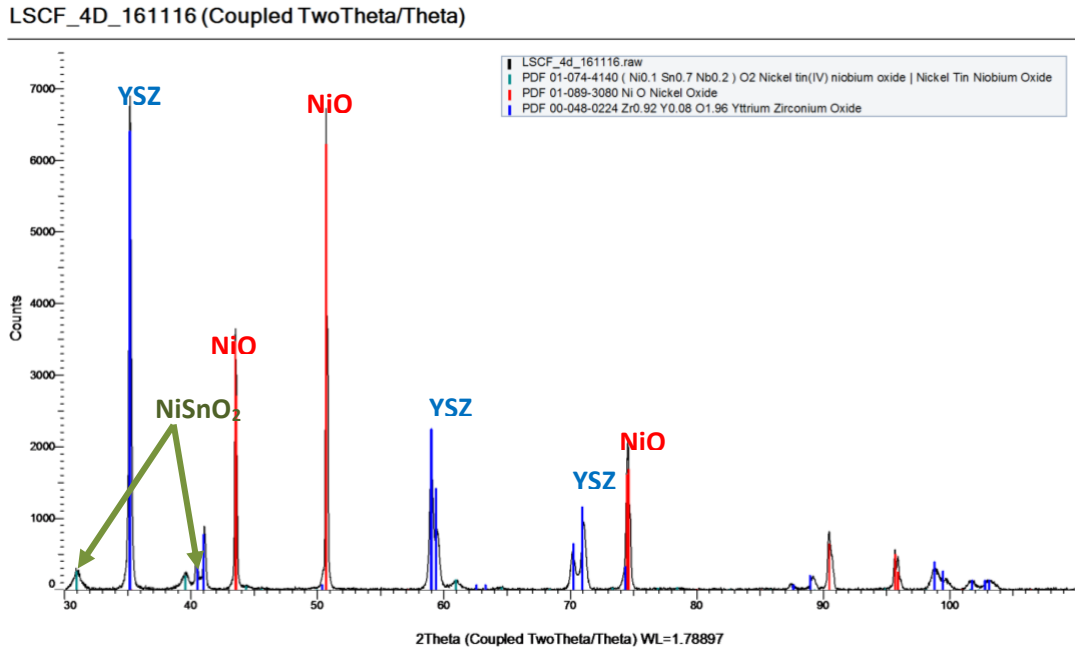


Figure 69 XRD spectrum analysis for 4D samples

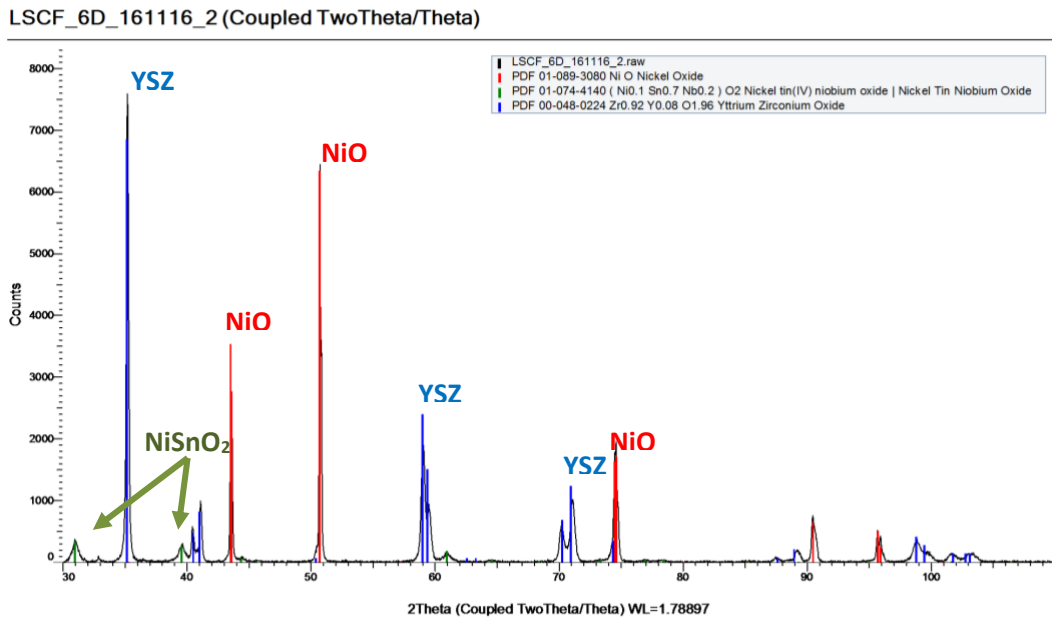


Figure 70 XRD spectrum analysis for 6D samples

To see the additional Sn more clearly, Figure 71 shows the superimposed 4D and 6D spectra on UD. At 31° and 39° of 2θ , both 4D and 6D spectra shows peaks which correspond to the Sn dopant on the sample surface. Another peak of Sn was found at 61° but this peak was not as prominent as the previous peaks. XRD analysis is usually based on the three highest peaks basis to recognise the phase spectrum thus the NiSnO_2 is at 31° , 39° and 61° on the 2θ area.

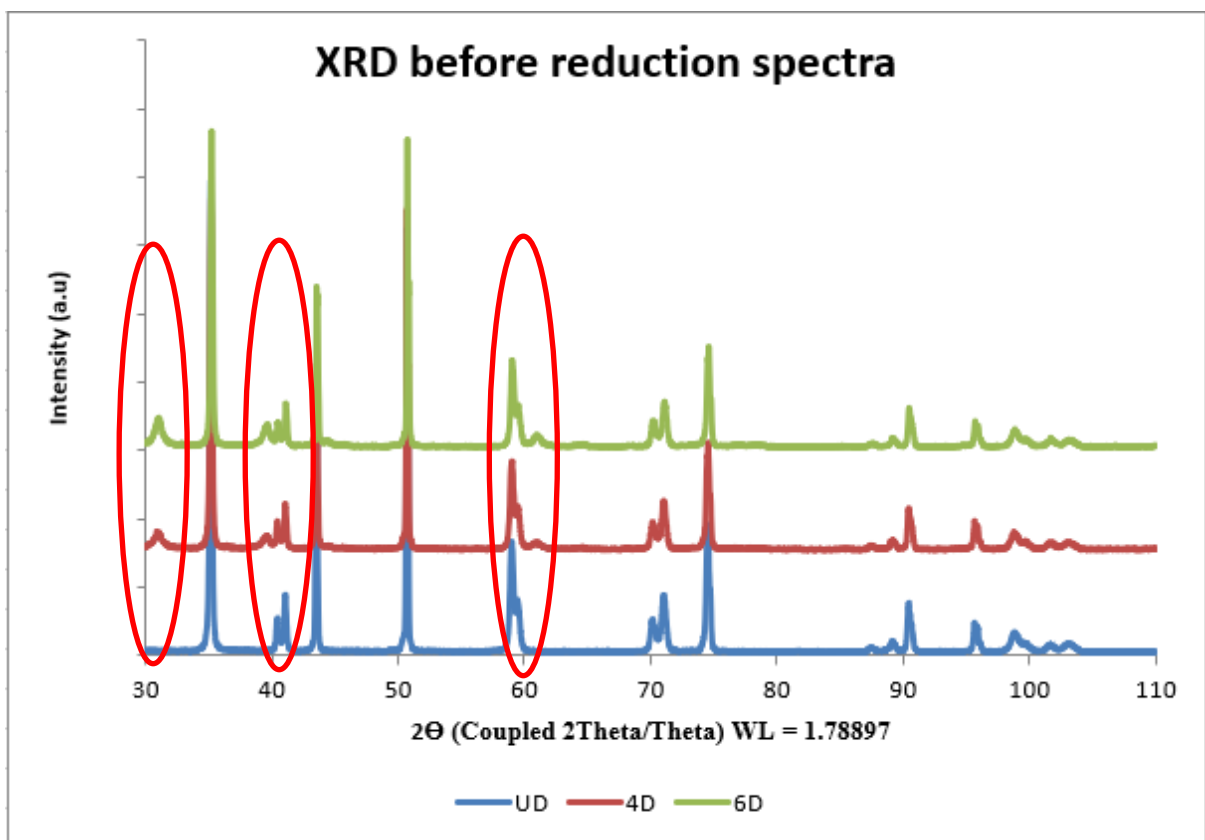


Figure 71 Superimposed XRD spectra of UD, 4D and 6D

The Sn dopant (in SnO state) was found to be more aligned to connect with the NiO sites based on the XRD results confirmation. To strengthen this proposed conclusion, another sample from our group's in-house Ni-YSZ anode support cells were doped with the same procedures as in this study. These samples were infiltrated with 4D of Sn dopant solution and tested with XRD. This was done to compare the Sn adsorption tendency on the anode

surface both in low porosity commercial cells (used in this study from Ningbo Co.) and high porosity cells (our group's in-house cells).

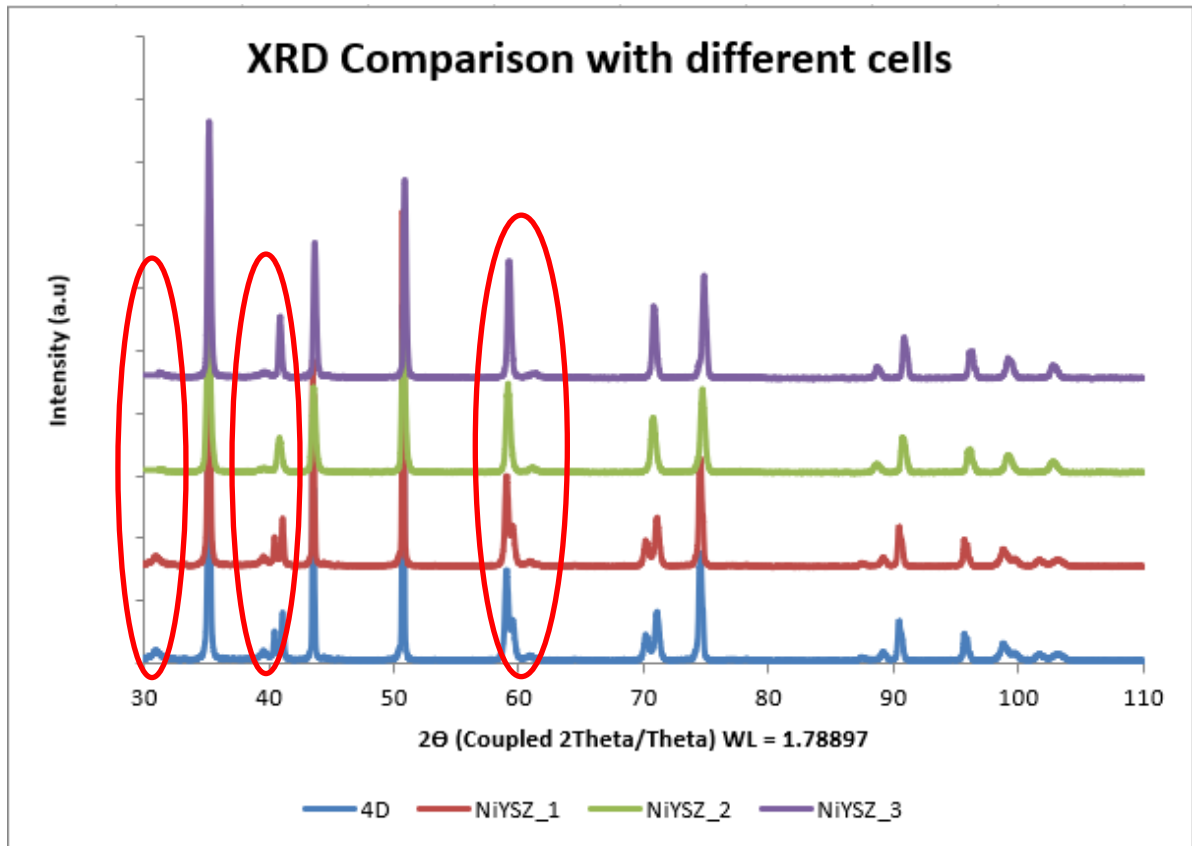


Figure 72 XRD spectra comparison of 4D cell with three in-house cells: NiYSZ_1, NiYSZ_2, and NiYSZ_3

Based on Figure 72, the additional Sn was found to be present in all the in-house cells but with lower peaks (in 31°, 39°, and 61°) compared with the 4D cell spectrum (less concentration of SnO on the surface). Due to the much higher porosity of the cells, the dopant will penetrate deeper into the substrate and be more equally distributed throughout the volume. Also, there is no immediate difference with YSZ sites on both the 4D and in-house cells. This proves the theory that SnO from the dopant solution will be more inclined to attach to the Ni sites rather than YSZ sites. Further evidence of this theory was expected to show on the after-reduction results.

5.2.4 XPS

XPS was used to calculate the atomic percentage of the elements in this study. The quantification results for the before-reduction of UD, 4D and 6D samples is presented in Table 21. For each sample, there were also three different spots that were observed which was the same technique used in SEM-EDX (centre, edge, and random). The results on Table 21 is the average calculation of the three spots that being studied in the samples.

According to the data from Table 21, the 4D and 6D cells contained around 1-at% on Sn 3d. The quantification analysis from the EDX in section 5.2.1 on the Sn content is between 4-at% to 8-at%. There is a significant gap in the results between EDX and XPS quantification. EDX offers information on concentration of elements in “bulk” and cannot differentiate the oxidation state while XPS can give near surface region composition (a few nm from surface). Due to the principle of both analysis, it is safe to assume that XPS has a higher precision and accuracy because it is based on the energy differences at orbital shells.

Table 21 BR samples average atomic % based on wide scan spectra peak intensities

Sample	C 1s %	Ni 2p %	O 1s %	Y 3d %	Zr 3d %	Sn 3d %	Si 2p %
UD	13.097	5.542	51.893	3.795	22.133	-	3.160
4D	17.320	9.993	48.660	2.753	18.447	1.010	1.786
6D	16.790	7.900	48.800	2.927	19.827	1.220	2.530

The Sn 3d/5 peaks after charge correction to C 1s are displayed on Figure 73. The peaks positions for the Sn 3d/5 in BR samples were detected around 485 to 488 eV. According to Table 22 from [146], these peaks correspond with Sn in its oxidation states (SnO or SnO₂). Another option for this binding energy range was for SnF₂, SnF₄, SnCl₂ and Na₂SnO₃ which

was quite unreasonable. Even if the Sn dopant solution was using $\text{SnCl}_2 \cdot 2\text{H}_2\text{O}$, there was no peaks found for Cl thus the SnCl_2 option was also not a good fit.

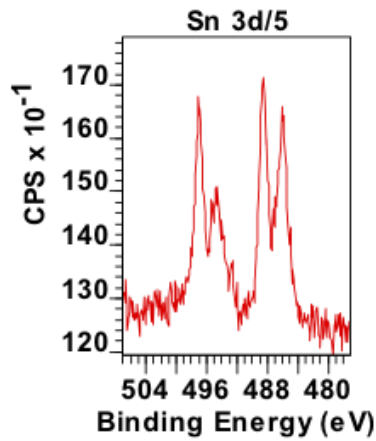


Figure 73 Sn 3d/5 spectrum BR sample

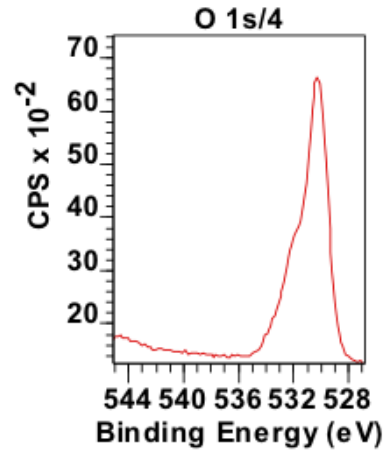


Figure 74 O 1s/4 spectrum BR sample

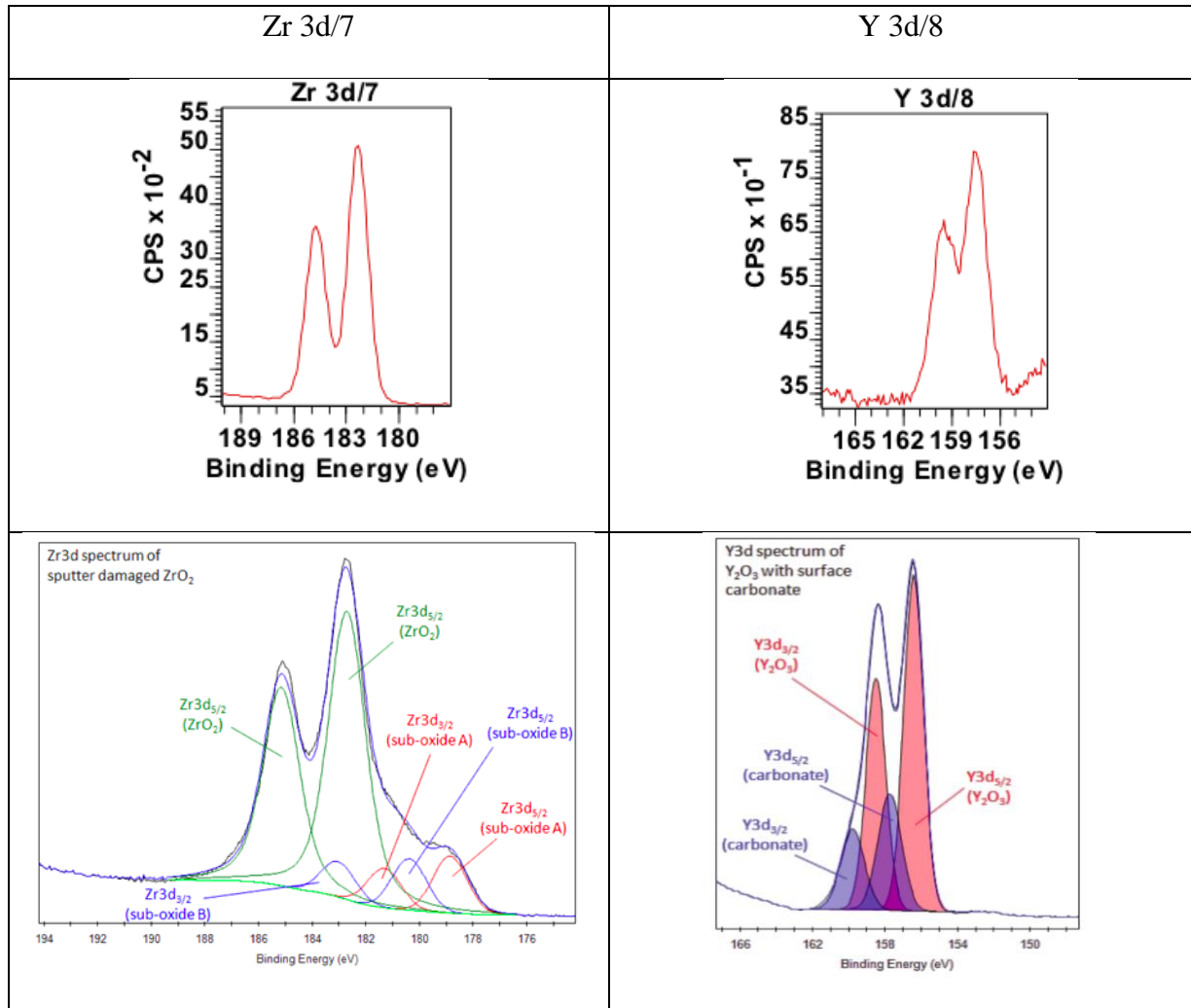
Another important spectrum that is thoroughly explained by the XPS result is O 1s. Both Ni and Sn were detected in oxidation state. The O 1s peaks in BR samples was supposed to be in metal oxides with defective states (530.2 eV and 531.8 eV), especially the one with nickel. This conclusion is suggested from its peak spectrum in Figure 74. If it was a pure oxide sample, there should be a second higher BE peak found that can be ascribed to contributions from a defective oxide component inherent in these oxide surfaces, as suggested previously in section 4.2. The possibility of a hydroxide state can be ruled out by using another method [151]. According to [146], the defective sites are unlikely to compromise the assignment of the chemical states, which happened to be the case with transitional metal oxides. Thus, the Ni in the samples can be concluded to be in the oxide states (with defective sites). It is probably the reason behind the perpetual Sn tendency to attach to the nickel oxide on the defective sites.

Table 22 Sn 3d binding energy lists [146]

Species	B.E. (eV)	Std. Dev
Sn (0)	485.0	0.5
SnO	486.5	0.6
SnO ₂	486.7	0.3
SnF ₂	487.2	0.2
SnF ₄	488.1	0.2
SnCl ₂	486.6	0.1
Na ₂ SnO ₃	486.7	0.4

In the previous section, both EDX and XRD ruled out the possibility of YSZ transformation caused by Sn. EDX indicated that Y and Zr elements were always found together. XRD results for BR samples suggested that YSZ was found in the oxidation state (Yttrium Zirconium Oxide). Both Y and Zr peaks spectrum from the XPS also pointed out the same conclusion. Zr 3d_{5/2} peak was found at 182.3 eV and Y 3d_{5/2} was found at 157.5 eV. These two peaks represented ZrO₂ and Y₂O₃ by referring to the database on [145,146].

Table 23 Zr 3d/7 and Y 3d/8 comparison analysis with database spectrum from [145]



5.3 After Reduction

After reduction (AR) is the most important ex-situ characterisation because it is the stage after the samples had been reduced overnight with hydrogen gas. After reduction samples would show the nearest condition of the sample from the actual sample that was tested on the rig. The AR ex-situ characterisation was expected to elucidate the change in the microstructures, especially with Ni and Sn. Chemical connection transformation between these two metals which had become the main focus of this study would also be expected to have happened.

5.3.1 SEM-EDX

After reduction results of SEM-EDX were expected to show the differences in the topographical or microstructural interconnections. The BR imaging results from SEM-EDX show interesting conditions such as surface tension phenomena, SnO tendency to be adsorbed onto NiO sites, and inhomogeneous distribution difference of infiltrated Sn dopant solution on the anode surface. By observing the samples after reduction using SEM-EDX, the change in SnO on the anode surface is clearer. The BSE images of the AR cells surface is shown on Figure 75.

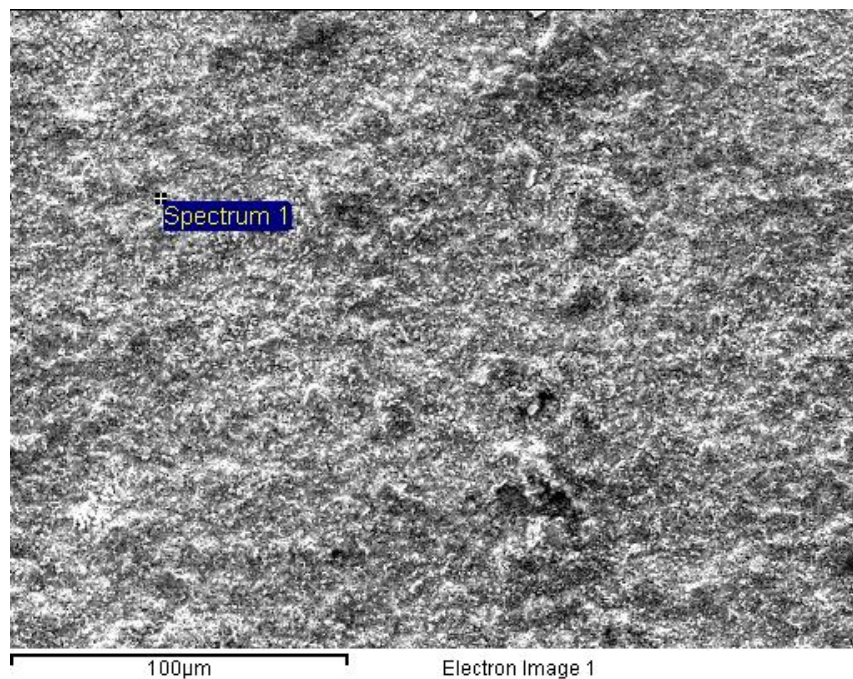


Figure 75 BSE images of 4D samples AR at 500x magnification

The average calculated chemical composition on 4D and 6D samples is shown in Table 24 and Table 25. It would be expected to show massive reduction of oxygen because the sample had been completely reduced. Even if the quantification using EDX cannot accurately and precisely represent the whole anode surface, it would help to see the decrease percentage at some point on molecular level.

Table 24 4D chemical composition for after reduction on anode surface at 500x magnification area

	Atomic Number	Normalised Calc. (wt%)	Atomic Calc. (at%)	Error
Nickel	28	17.85	19.57	0.01
Yttrium	39	4.36	3.16	0.80
Zirconium	40	68.95	48.66	0.30
Tin	50	2.00	1.09	0.40
Oxygen	8	6.84	27.52	2.04

Table 25 6D chemical composition for after reduction on anode surface at 500x magnification area

	Atomic Number	Normalised Calc. (wt%)	Atomic Calc. (at%)	Error
Nickel	28	35.55	38.31	0.01
Yttrium	39	3.64	2.59	0.80
Zirconium	40	50.47	35.00	0.35
Tin	50	4.90	2.61	0.50
Oxygen	8	5.43	21.48	3.05

The change in the average chemical compositions is related closely with overnight reduction on hydrogen gas. By comparing Table 24 and Table 25 with the previous section 5.2.1 (see Table 17 and Table 18), there are a huge different with the results. Nickel in AR samples were increased from 0.55 wt% to 17.85 wt% and from 0.43 wt% to 35.55 wt%, for 4D and 6D respectively. Meanwhile, Sn was reduced sharply from 13.16 wt% to 2 wt% for 4D and from 25.72 wt% to 4.90 wt% for 6D sample. This is the effect of the reduction where the Ni and Sn in oxidation state being stripped from oxygen. The oxygen was decreased sharply from around 70 wt% to approximately 5 wt% in the after-reduction samples. Both Y and Zr also underwent massive change according to the EDX quantification results. AR samples showed higher number of Zr but the BR samples showed higher number of Y. This change needs to be studied further to explain more about the microstructural condition of Sn/Ni-YSZ.

5.3.2 XRF

XRF results after reduction are shown in Table 26 and Table 27. The calculated statistical errors for the main elements (Ni, Y, Zr) were lower than 0.5%. For the representative impurities (Hf, Si, Zn), the statistical error was lower than 5%. There is a change on Sn statistical calculation for the AR results which decreased into lower than 1% error. The change in the scan error can be pointed to the possibility of easier Sn states (change into metal or alloy) on the anode surface that makes the calculation more precise and accurate.

Table 26 Comparison of elements concentration after reduction

Cell Type	Calculated Concentrations (wt%)						
	Ni	Y	Zr	Sn	Hf	Si	Zn
UD	51.22	2.04	45.92	-	0.77	-	0.02
4D	49.58	2.07	46.37	1.05	0.77	-	-
6D	46.94	2.08	48.51	1.66	0.77	-	-

The analysed layer between the AR results is not different from each other, as established from the previous BR results (shown in Table 20). One thing that is important to note in the AR XRF scan results is the disappearance of the Si and Zn impurities. There were no peaks found for Si and Zn, or other impurities. The disappearance of the impurities has a high chance to be the effect of reduction. The reduction stage was not only releasing the oxygen from main components oxidation state but also releasing the impurities from the cells (except for Hf).

Table 27 Comparison of analysed layer for the elements before reduction

Cell Type	Analysed Layer (μm)						
	Ni	Y	Zr	Sn	Hf	Si	Zn
UD	19.6	44	50	-	22.8	-	10.2
4D	19.2	44	51	78	22.3	-	-
6D	18.7	46	53	77	21.7	-	-

The elements comparison for before and after reduction is shown in Table 28. For doped cells, all the main elements (Y, Zr, and Sn) increased in concentrations except for nickel. The decreased concentration in nickel is proposed to be because the nickel state before and after reduction. Before reduction, nickel was in oxidation state (NiO) and not yet formed alloy with Sn (still in SnO state). After reduction, Ni is expected to change into Ni metal, Sn/Ni alloy, and some Ni in oxidation state (discussed more on section 5.2.3 and 5.2.4). Based on the XRF results, there is a change in the nickel state but still need more data is needed to find out more about the transformation.

Table 28 Comparison of element concentrations before and after reduction (in wt%)

Element	UD		4D		6D	
	BR	AR	BR	AR	BR	AR
Ni	49.18	51.22	50.19	49.58	47.66	46.94
Y	2.08	2.04	1.99	2.06	2.06	2.08
Zr	48.03	45.95	46.19	46.37	47.65	48.51
Sn	-	-	0.91	1.05	1.24	1.66
Hf	0.61	0.76	0.69	0.77	0.76	0.76
Si	0.05	-	-	-	-	-
Zn	0.03	-	0.03	-	0.03	-

The Sn concentration is also higher in the AR results. This might be because previously in BR samples, Sn was in SnO structures. It was assumed that the oxidation state of tin was “interfering” with the XRF scan. However, in the AR samples, the SnO transformed into Ni/Sn alloy and a little bit of Sn metal, lowering the concentration of SnO on the anode

surface. The x-ray beam replaced the electron inside the orbital shells of the metal and alloy easier than in the oxidation state.

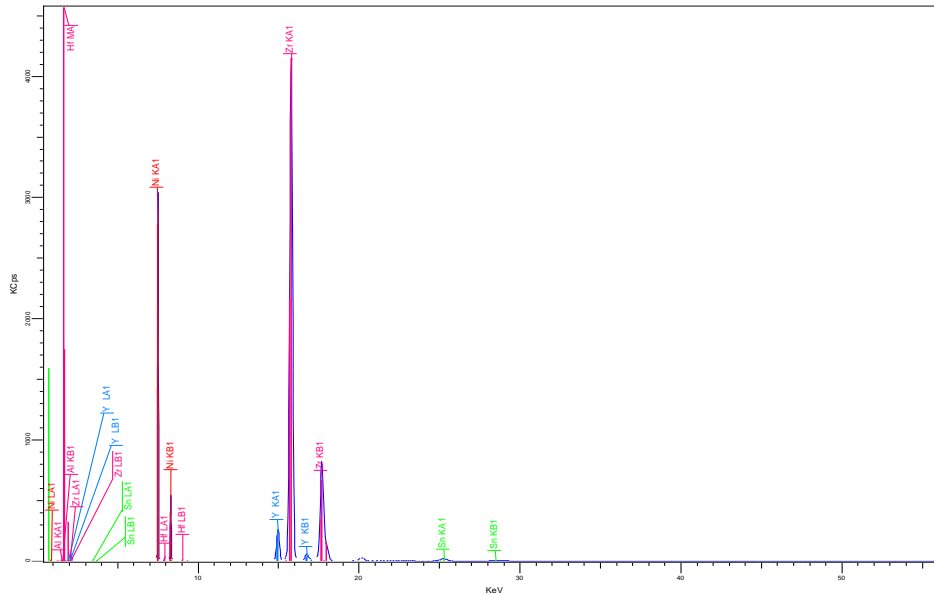


Figure 76 XRF qualitative scan for 4D (impurities removed)

Sn calculated concentration in XRF for after reduction is showing consistency with previous finding in determining the highest performance in cell testing. Both from literature [61,64,137] and cell testing results (in section 4.3.2) pointed out that 4D with approximately 1 wt% of Sn dopant on the anode surface gave the best performance. Sn/Ni-YSZ offers better carbon resistance and higher power density compared to commercial cells.

5.3.3 XRD

XRD scan results for the AR samples are very important in this study. The results were expected to prove some theories on SnO microstructural and chemical changes. The theories for the SnO changes are as follows:

- Sn dopant solution would transform into SnO \rightarrow Sn (metal) \rightarrow Sn/Ni alloy
- SnO is more inclined to attach to the NiO sites on the anode surface

Figure 77 and Figure 78 displays the UD and 4D spectra after reduction respectively. Phase analysis from the UD sample showed the changes in the NiO. The analysis from the DIFFRAC.EVA software revealed that the phase found on the UD samples were Ni (metal phase), NiO, and YSZ. NiO from the previous discussion in section 5.2.3 was expected to change into its metal state. However, there was a little bit of NiO found on the AR samples (shorter peaks than the BR spectrum from the same sample). The NiO is related with the oxidation with air (discussed more on 5.3.4) and stayed on the anode surface of the samples. XRD is a very sensitive instrument for surface analysis. Furthermore, the surface samples were not cleaned or scrubbed with anything to get the most precise results on their surfaces.

Figure 78 and Figure 79 shows the XRD spectrum of AR 4D and 6D samples, respectively. The phase analysis from both doped cells came out as follows: Ni, Ni₃Sn, NiO, and YSZ. According to the Ni/Sn phase diagram in Figure 23, Ni₃Sn alloy phase is possible to form in the range of 24-26 atomic% of tin at 750°C. Based on the EDX quantification results after reduction, the atomic% of tin was less than 10%. This shows that the EDX could not represent the actual composition of the anode surface but still can be used to give the idea of the topography and physical changes.

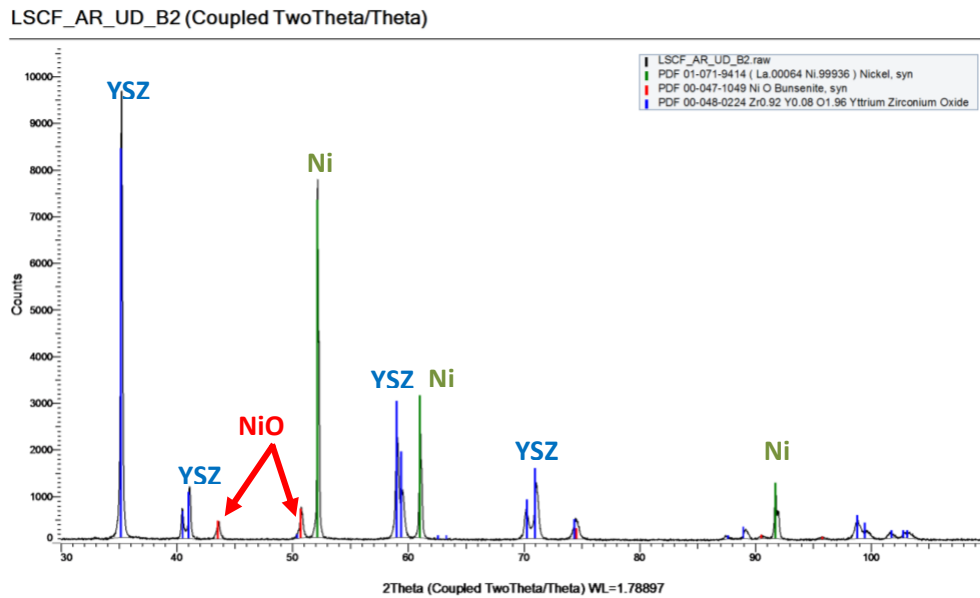


Figure 77 XRD spectrum of after reduction UD sample

The Ni_3Sn phase is one type of Sn/Ni alloy phase that is found at 34° , 46° , and 53° on the 2theta/theta scanning area of the doped cells. Aside from the Ni_3Sn , the NiO and NiSnO_2 also transformed into nickel in its metal state and some NiO . There was no striking change that happened to the YSZ aside from the difference in the ‘Counts’ on the Y-axis (related to detected photons). Nickel in metal state was detected at 52° , 61° , and 91° degree, meanwhile the NiO phase was detected at 44° , 51° , and 74° . The detected degree for NiO was the same as the BR spectra for UD, 4D, and 6D but with much shorter peaks (fewer photons detected). Thus, it was concluded that both NiO and NiSnO_2 are responsible for the transformation into metal and alloy state of Ni and Sn.

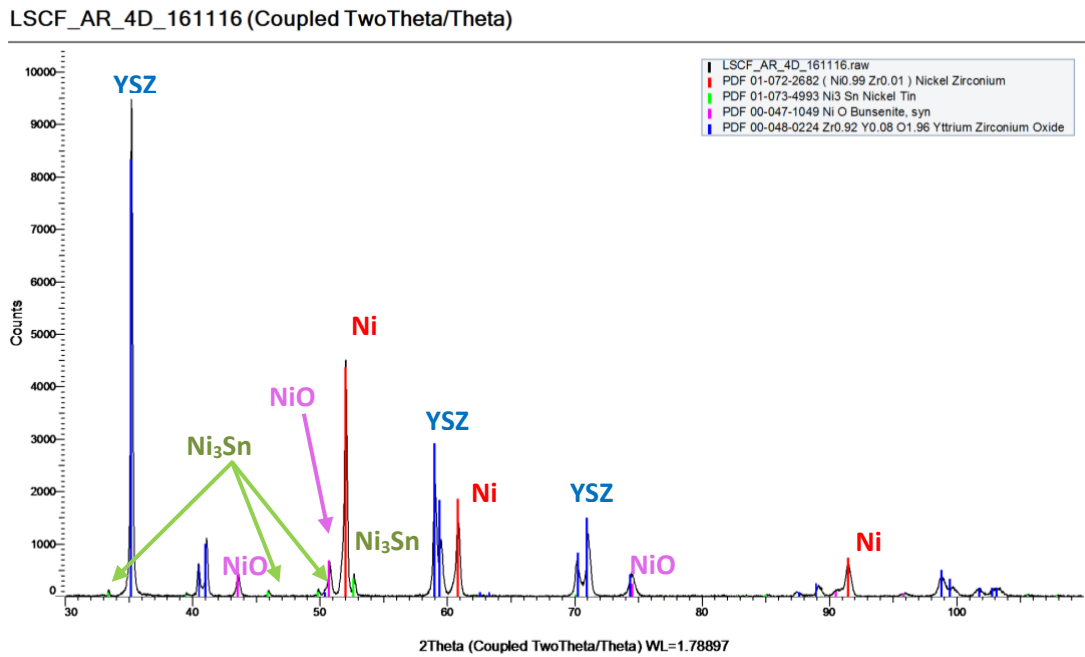


Figure 78 XRD spectrum of after reduction 4D sample

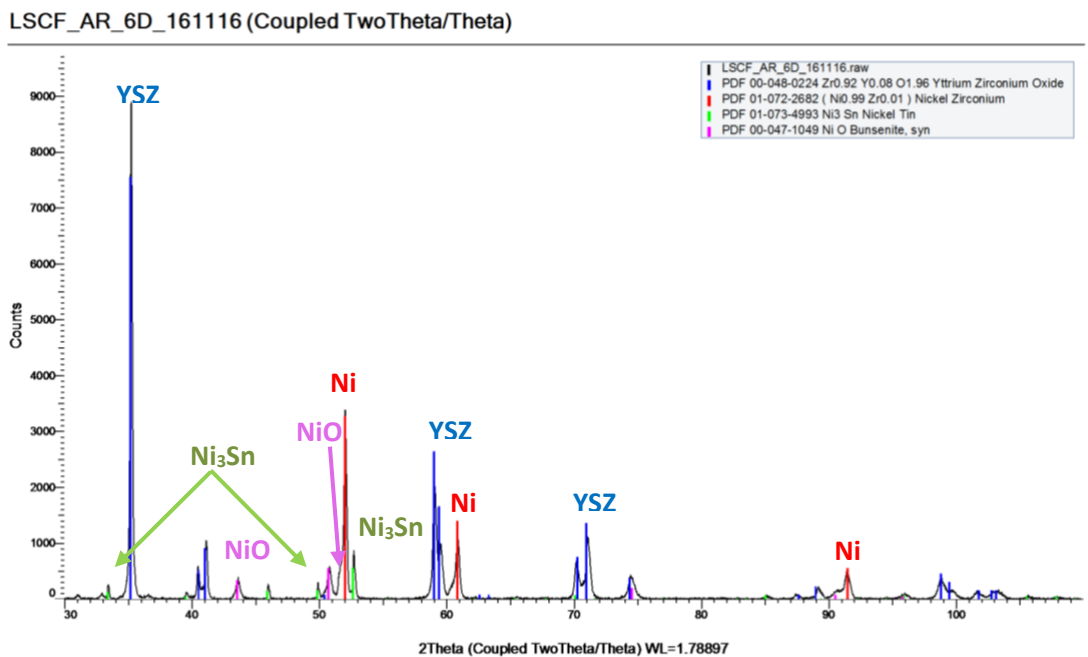


Figure 79 XRD spectrum of after reduction 6D sample

The superimposed XRD spectra of UD, 4D, and 6D is shown in Figure 80. The red oval line is pointing at the position differences between the undoped and doped cells on the 2theta area. As shown on Figure 80, the important changes were detected between the range of 37°

to 54° of 2θ area. This is because that is the area where nickel and its different phases had the most peaks.

For the comparison, the three-peaks chosen area is essential to see the differences of the SnO in undoped and doped cells. It has been concluded from the literature and section 4.3 that the doped cells which were suspected to contain the Sn/Ni alloys gave the higher performance. The XRD after reduction is confirming the theory of the present Sn/Ni alloy on the anode surface related to the increase performance of the cells.

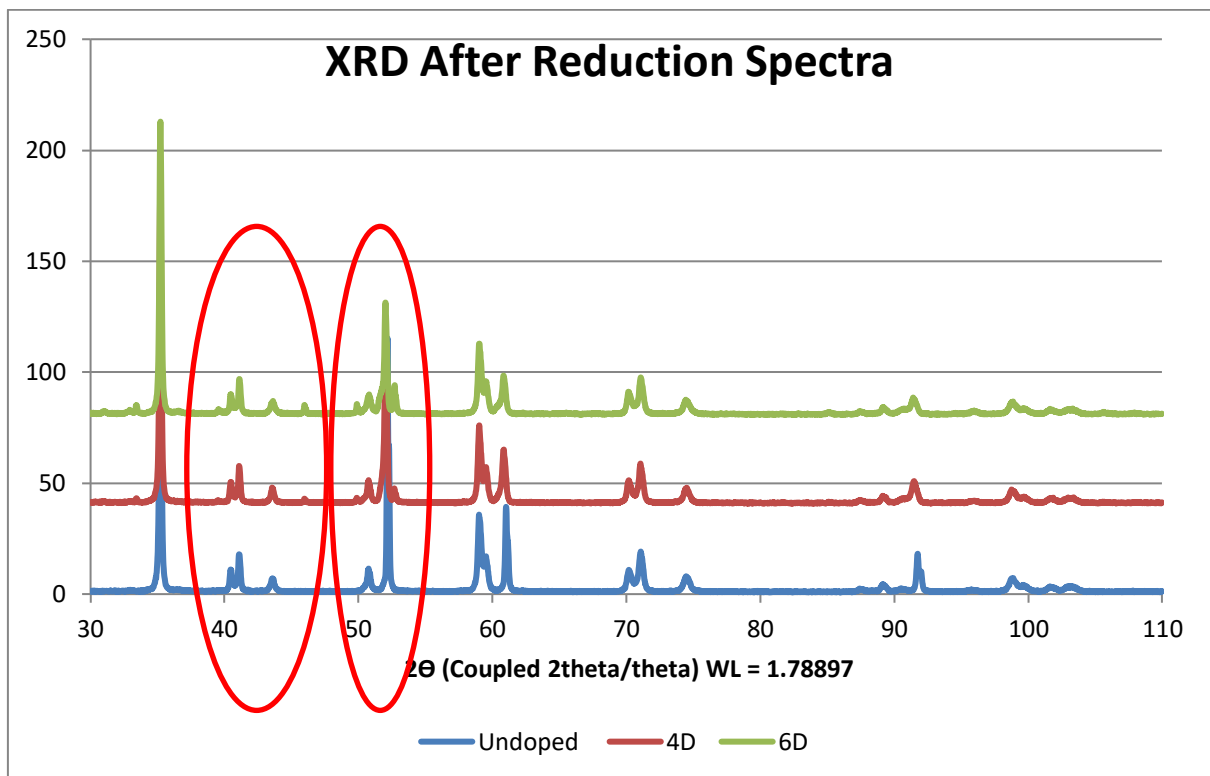


Figure 80 Superimposed XRD spectra of UD, 4D, and 6D

5.3.4 XPS

The XPS spectrum from AR samples was superimposed with the BR results to clearly show the change in chemical activities between the two sample groups. As stated in the section 4.2, the highest peaks found in the Ni 2p spectrum was at 856.4 eV binding energy.

Different spectra will inherently follow by the alteration on binding energy. The following images use previous data from the sample reference (UD BR sample) to compare the spectra shift for each type of samples. Figure 81 shows the the Ni 2p spectra of UD, 4D, and 6D samples before (red) and after (black) reduction.

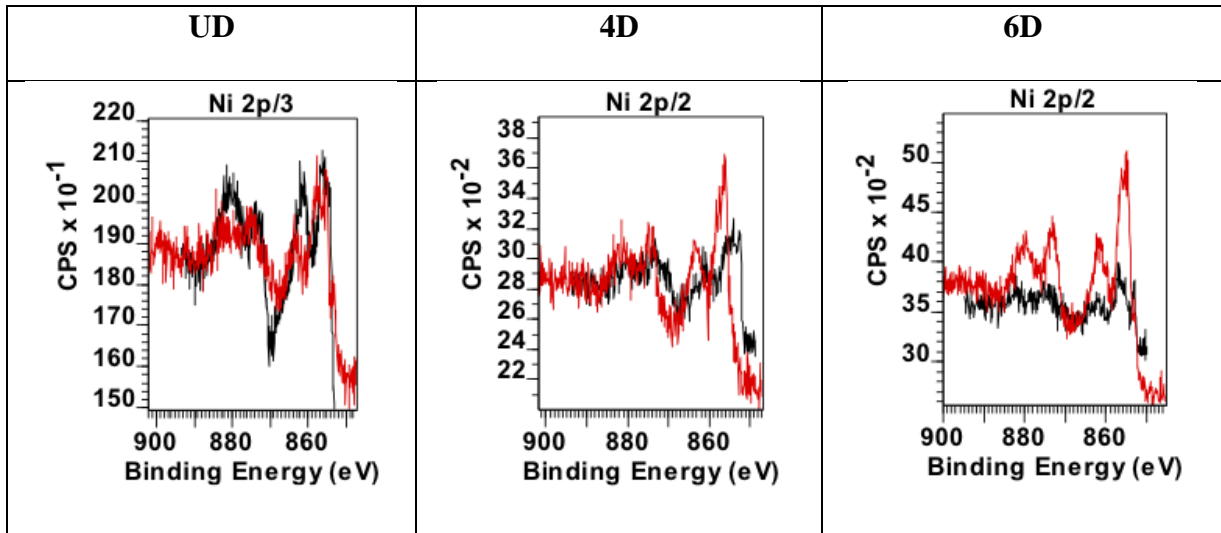


Figure 81 Various superimposed Ni 2p spectra for before (red) and after (black) reduction

According to Figure 51 in section 4.2, Ni metal highest peak is expected to be detected at around 852.6 eV. If there was nickel metal present in the AR samples, the black spectrum would have shifted to the right. As displayed in Figure 81, the doped samples AR spectrum is shifted to the right with shorter peaks as it contained less Sn. The UD samples Ni 2p spectra also shows some chemical change as the red and black spectrum have different patterns.

More in-depth analysis using CASAXPS shows that AR samples for doped cells contained traces of nickel metal, NiO and complex Ni sites in the range of 870 eV to 885 eV. There is one study found regarding this binding energy range corresponding with nickel-iron catalysts [152]. In this study, it was proposed to be the corresponding peak sites of Sn/Ni alloy.

Table 29 shows the average atomic percentage present in the samples after reduction. It is important to note that this data is from the post-testing samples to clearly see the effect of Sn dopant. It is clear that the Sn dopant is producing less carbon on the cell after used in dry reforming on both biogas and hydrogen fuels. According to the data from the Table 21, there is less amount of Sn 3d detected on the samples compared to the BR samples (1-at%-1.5-at%). It is safe to assume that the Sn has been transformed into mixed alloy and oxidation state during the testing. Sn also had been used in the chemical reaction during the testing period. Thus, the Sn present in the aftermath is the leftover Sn detected on the anode surface.

Table 29 XPS average atomic concentration for each elements spectrum in AR samples

Sample	C 1s %	Ni 2p %	O 1s %	Si 2p %	Sn 3d %	Y 3d %	Zr 3d %
UD	40.780	4.445	42.080	0.700	-	1.255	7.405
4D	24.360	12.980	39.350	1.600	0.735	1.560	8.825
6D	28.045	12.980	41.880	0.300	0.175	1.880	10.790

*Several impurities are not shown and considered negligible as the value is less than 0.5-at%

Sn spectra comparison for the doped cells is shown in Figure 80 (a) and (b). The different amount of Sn in atomic concentration between 4D and 6D is the representation of the peaks found for the corresponding samples in Figure 80. For BR samples (red line spectra), 6D sample had more prominent peaks as the Sn concentration is higher than the 4D. As for the Sn concentration after the reduction and used in the cell testing, the amount of Sn left could not be determined with the previous reference in BR condition.

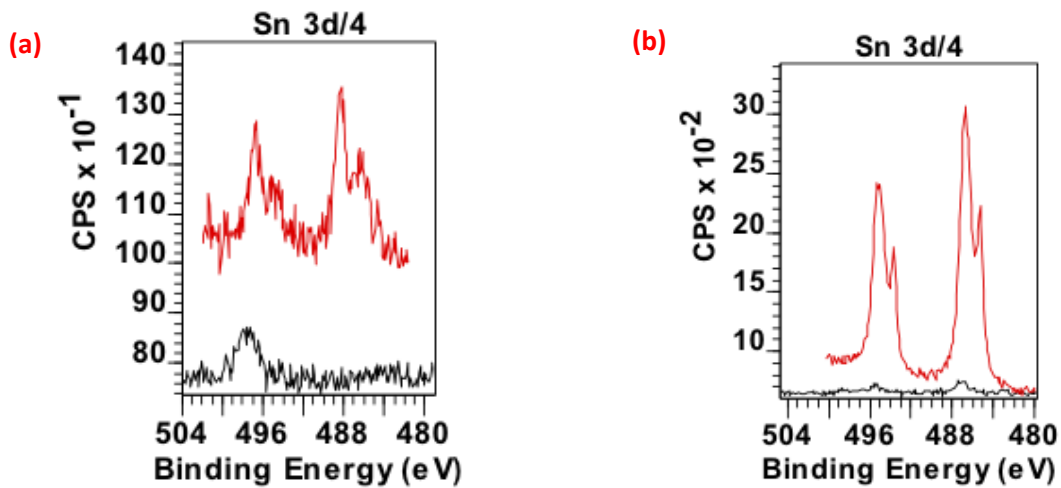
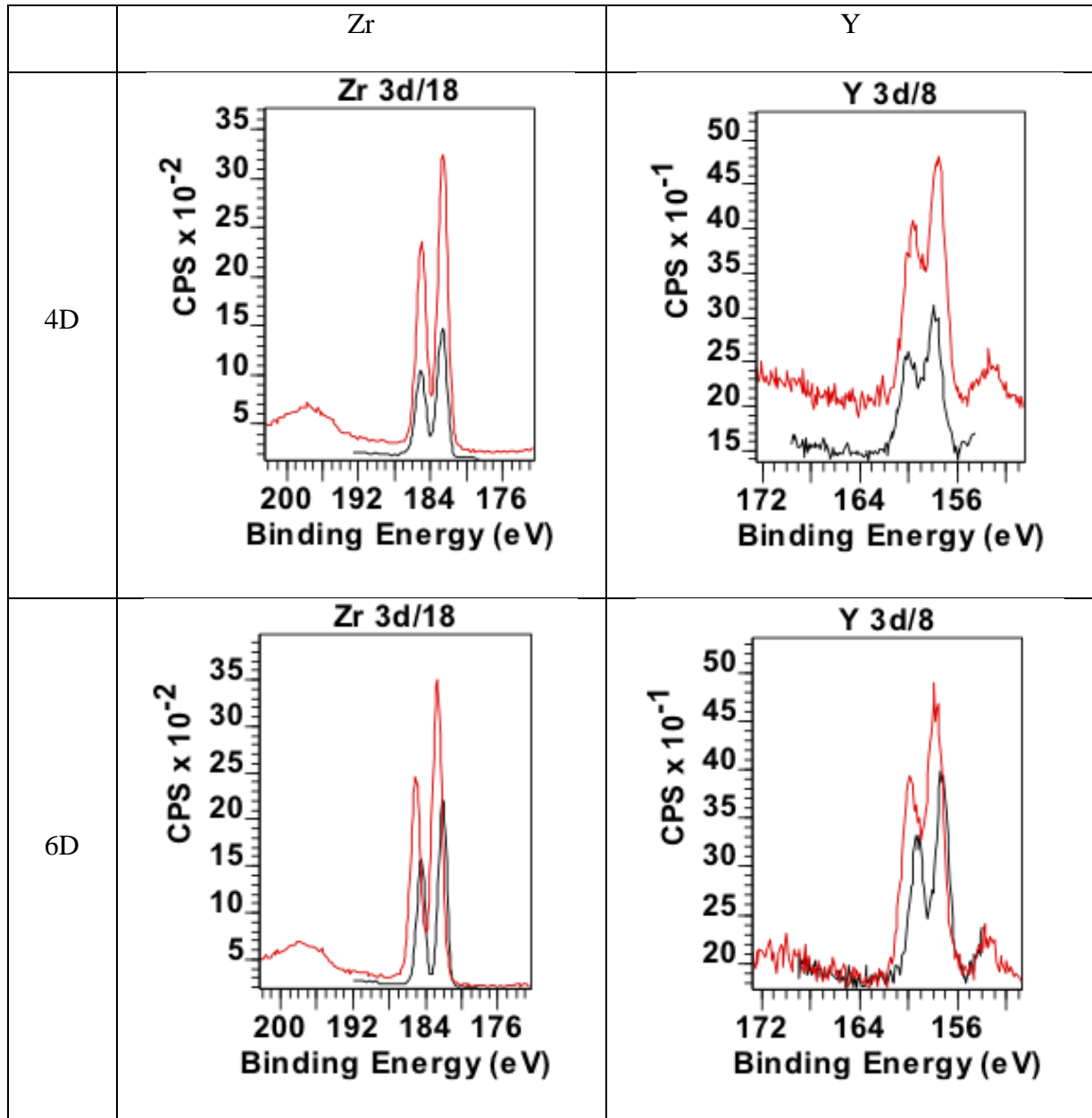


Figure 82 Sn 3d/4 spectra comparison for before (red) and after used (black) for (a) 4D and (b) 6D

The Y and Zr appear to stay in the same oxidation states based on their spectra as shown in Table 31. This result is consistent with other instrument results such as EDX and XRD. The difference lies only in the amount of atomic concentration which is based on the peak height. Aside from that, there is no large change in the chemical states themselves. The UD spectra also show no differences between BR and AR spectrum results.

Table 30 Zr and Y spectra comparison for 4D and 6D



Chapter 6 Conclusions

6.1 Overview

There are several important findings from this study. The following conclusions represent the main points from results and discussion from the previous chapters. The conclusions are meant to answer the objectives of this study as stated in section 1.6.

6.2 Main Points

1. Sn-infiltration into full cell anode support Ni-YSZ via pipette drop technique is repeatable and reproducible for manufacturing Sn/Ni-YSZ even on low porosity anode surface.
2. Slow drying process in-between drops when preparing the doped cell is the key to reduce the possibility of surface area phenomena. It is recommended to do calcination at 600° C for 2 hours every 4 mg to 6 mg of Sn has been added onto the cells.
3. The highest performance of Sn/Ni-YSZ has been obtained from around 1 wt% Sn on the anode surface of SOFCs with dry reforming on biogas feed, with 0.35 ± 0.05 W/cm² at 1.1 ± 0.05 V. Other variation of Sn/Ni-YSZ also show higher electrical performance with approximately 20-30% better methane reforming compared to undoped Ni-YSZ during dry reforming with biogas feed.
4. Different content of Sn on the anode surface led to different electrochemical performance. Sn content in the range of 0.57 mg/cm² to 0.85 mg/cm² on the cell anode resulted in lower activation resistance, better ohmic resistance, and polarisation resistance compared to standard commercial cells (undoped).
5. Sn-infiltration via pipette drop using a mixture solvent with SnCl₂.2H₂O and 95 vol% ethanol could be used to form Sn/Ni-YSZ. Ni₃Sn is the alloy state that was found on the anode surface after completely reducing with hydrogen gas overnight.

6. SnO is the state of the Sn dopant solution after the calcination process which is inclined to attach to NiO sites, forming NiSnO₂ sites. SnO is not inclined to attach to YSZ sites on the anode surface.
7. NiSnO₂ transformed into Ni metal, NiO in complex mixed oxidations states and Ni₃Sn (alloy) on the anode surface after reduction. YSZ has little changes in phase form from before and after reduction without any remarkable shift on XRD peaks.
8. Sn/Ni sites after reduction is forming “highway” for easier fuel gas flow into the triple boundary phase. It is proposed that Sn/Ni alloy incorporated to electrically connect more Ni sites (on the surface and inside the pores) more fuel gas directly contacts both the nickel and Sn catalysts. This condition leads to higher electrochemical oxidation rates which eventually resulted in higher current and power density.

6.3 Further Work

Based on the results in this study, further work is suggested in the following areas:

- Using SEM, FIB-SEM, or TEM to see the physical changes in microstructures and topography of the anode surface.
- Using adsorption and desorption instruments for further characterisation of the chemical reactions.
- Study the upper limit for Sn content inside the anode support Ni-YSZ cells to get the whole range of Sn dopant for SOFCs.

Bibliography

1. Karl TR, Trenberth KE. Modern Global Climate Change. *Science* (80-). 2003;302(5651):1719–23.
2. IPCC. Climate Change 2014: Mitigation of Climate Change: Contribution of Working Group III to the Fifth Assessment Report of the Intergovernmental Panel on. Cambridge Univ Press 2014;1132 pp.
3. IEA. Key World Energy Statistics [Internet]. 2016.
4. Peterson TC, Connolley WM, Fleck J. The myth of the 1970s global cooling scientific consensus. Vol. 89, *Bulletin of the American Meteorological Society*. 2008. p. 1325–37.
5. Williams JC. History of energy. Franklin Institute’s Resour Sci Learn Sci Energy. 2006;
6. Righter RW. Wind energy in America: A history. University of Oklahoma Press; 1996.
7. Lewis M. Technics and civilization. *ESST Core Lit*. 1934;145–215.
8. Perlin J. From space to Earth: the story of solar electricity. In: *From Space to Earth*. 1999. p. 224.
9. Laird FN, Stefes C. The diverging paths of German and United States policies for renewable energy: Sources of difference. *Energy Policy*. 2009 Jul [cited 2015 Aug 19];37(7):2619–29.
10. Gan L, Eskeland GS, Kolshus HH. Green electricity market development: Lessons from Europe and the US. *Energy Policy*. 2007 Jan [cited 2015 Nov 20];35(1):144–55.
11. Björheden R. Drivers behind the development of forest energy in Sweden. *Biomass and Bioenergy*. 2006 Apr [cited 2016 Feb 11];30(4):289–95.
12. Jacobsson S, Johnson A. The diffusion of renewable energy technology: an analytical framework and key issues for research. *Energy Policy*. 2000 Jul [cited 2015 Jan 16];28(9):625–40.
13. Chu S, Majumdar A. Opportunities and challenges for a sustainable energy future.

- Nature. 2012 Aug 16;488(7411):294–303.
14. Economy TH, Committee N, Production FH, Isbn C, Pdf T, Press NA, et al. The Hydrogen Economy: Opportunities, Costs, Barriers, and R&D Needs [Internet]. SciencesNew York. 2004. 256 p.
 15. Yildiz B, Kazimi M. Efficiency of hydrogen production systems using alternative nuclear energy technologies. *Int J Hydrogen Energy*. 2006;31(1):77–92.
 16. Ritter J a., Ebner AD. State-of-the-Art Adsorption and Membrane Separation Processes for Hydrogen Production in the Chemical and Petrochemical Industries. *Sep Sci Technol*. 2007;42(6):1123–93.
 17. Düsterwald HG, Günnewig J, Radtke P. DRIVE – The Future of Automotive Power: Fuel Cells Perspective. *Fuel Cells*. 2007 Jun [cited 2016 Feb 9];7(3):183–9.
 18. Xu J, Yeung CMY, Ni J, Meunier F, Acerbi N, Fowles M, et al. Methane steam reforming for hydrogen production using low water-ratios without carbon formation over ceria coated Ni catalysts. *Appl Catal A Gen*. 2008;345(2):119–27.
 19. Ni M, Leung DYC, Leung MKH, Sumathy K. An overview of hydrogen production from biomass. *Fuel Process Technol*. 2006 May [cited 2014 Aug 20];87(5):461–72.
 20. Larminie J, Dicks A. Fuel cell systems explained [Internet]. *Fuel*. 2003. xxii, 406 .
 21. Mekhilef S, Saidur R, Safari A. Comparative study of different fuel cell technologies. *Renew Sustain Energy Rev*. 2012;16(1):981–9.
 22. Colella W. Design options for achieving a rapidly variable heat-to-power ratio in a combined heat and power (CHP) fuel cell system (FCS). *J Power Sources*. 2002;106(1):388–96.
 23. Colella W. Implications of electricity liberalization for combined heat and power (CHP) fuel cell systems (FCSs): A case study of the United Kingdom. In: *Journal of Power Sources*. 2002. p. 397–404.
 24. Hawkes AD, Brett DJL, Brandon NP. Fuel cell micro-CHP techno-economics: Part 1 – model concept and formulation. *Int J Hydrogen Energy*. 2009;34(23):9545–57.
 25. Hamada Y, Takeda K, Goto R, Kubota H. Hybrid utilization of renewable energy and fuel cells for residential energy systems. *Energy Build*. 2011;43(12):3680–4.
 26. Keim M, Kallo J, Friedrich KA, Werner C, Saballus M, Gores F. Multifunctional fuel

- cell system in an aircraft environment: An investigation focusing on fuel tank inerting and water generation. *Aerosp Sci Technol.* 2013;29(1):330–8.
27. Cleveland DJ, Morris C. Handbook of Energy: Chronologies, Top Ten Lists, and Word Clouds. In: *Handbook of Energy: Chronologies, Top Ten Lists, and Word Clouds.* 2013. p. 968.
 28. Srinivasan S, Mosdale R, Stevens P, Yang C. Fuel cells: reaching the era of clean and efficient power generation in the twenty-first century. *Annu Rev Energy Environ.* 1999;24(1):281–328.
 29. Atkinson a, Barnett S, Gorte RJ, Irvine JTS, McEvoy a J, Mogensen M, et al. Advanced anodes for high-temperature fuel cells. *Nat Mater.* 2004;3(1):17–27.
 30. Zhu W., Deevi S. A review on the status of anode materials for solid oxide fuel cells. *Mater Sci Eng A.* 2003;362(1):228–39.
 31. Irshad M, Siraj K, Raza R, Ali A, Tiwari P, Zhu B, et al. A Brief Description of High Temperature Solid Oxide Fuel Cell's Operation, Materials, Design, Fabrication Technologies and Performance. *Appl Sci.* 2016;6(3):75.
 32. Manglik RM, Magar YN. Heat and Mass Transfer in Planar Anode-Supported Solid Oxide Fuel Cells: Effects of Interconnect Fuel/Oxidant Channel Flow Cross Section. *J Therm Sci Eng Appl.* 2015 Dec 1;7(4):41003–10.
 33. Su S, Gao X, Zhang Q, Kong W, Chen D. Anode- Versus Cathode-Supported Solid Oxide Fuel Cell : Effect of Cell Design on the Stack Performance. *Int J Electrochem Sci.* 2015;10:2487–503.
 34. Yakabe H, Ogiwara T, Hishinuma M, Yasuda I. 3-D model calculation for planar SOFC. *J Power Sources.* 2001;102(1–2):144–54.
 35. Minh NQ. Solid oxide fuel cell technology - Features and applications. Vol. 174, *Solid State Ionics.* 2004. p. 271–7.
 36. Droushiotis N, Grande FD, Dzarfan Othman MH, Kanawka K, Doraswami U, Metcalfe IS, et al. Comparison between anode-supported and electrolyte-supported Ni-CGO-LSCF micro-tubular solid oxide fuel cells. *Fuel Cells.* 2014;14(2):200–11.
 37. Vijaya Lakshmi V, Bauri R, Gandhi AS, Paul S. Synthesis and characterization of nanocrystalline ScSZ electrolyte for SOFCs. *Int J Hydrogen Energy.*

- 2011;36(22):14936–42.
38. Gong M, Liu X, Trembly J, Johnson C. Sulfur-tolerant anode materials for solid oxide fuel cell application. *J Power Sources*. 2007 Jun [cited 2016 Mar 15];168(2):289–98.
 39. McPhail SJ, Leto L, Boigues-Munoz C. *The Yellow Pages of SOFC Technology International Status of SOFC Deployment 2012-2013*. 2013.
 40. Naimaster EJ, Sleiti AK. Potential of SOFC CHP systems for energy-efficient commercial buildings. *Energy Build*. 2013;61:153–60.
 41. UNFCCC. Copenhagen Accord of 18 [Internet]. Fifteenth Session of the Conference of the Parties to the United Nations Framework Convention on Climate Change. 2009.
 42. Horiuchi K. Current Status of National SOFC Projects in Japan. *ECS Trans* . 2013;57(1):3–10.
 43. Wachsman E, Singhal S. Solid oxide fuel cell commercialization, research and challenges. *The Electrochemical Society Interface*. 2009;(Fall):38–43.
 44. McPhail SJ, Cigolotti V, Moreno A. Fuel cells in the waste-to-energy Chain. *Green Energy Technol*. 2012;45.
 45. Stambouli AB, Traversa E. Solid oxide fuel cells (SOFCs): A review of an environmentally clean and efficient source of energy. *Renew Sustain Energy Rev*. 2002;6(5):433–55.
 46. History of Biogas 1 [Internet]. Kingdom BioEnergy. [cited 2017 Mar 23].
 47. Penn State College of Agricultural Science. A Short History of Anaerobic Digestion. In: *Methane Recovery from Animal Manures: The Current Opportunities Casebook*. 2016. p. 4–6.
 48. College M, McCabe J, Eckenfelder WW. *Biological treatment of sewage and industrial wastes*. 1956;
 49. Deublein D, Steinhauser A. *Biogas from waste and renewable resources. Choice: Current Reviews for Academic Libraries*. 2008. 443 p.
 50. Herout M, Malaták J, Kucera L, Dlabaja T. Biogas composition depending on the type of plant biomass used. *Res Agric Eng*. 2011;57(4):137–43.

51. Rostrup-Nielsen JR, Anderson JR, Boudart M. Catalysis science and technology, vol. 5. by JR Anderson and M. Boudart, Springer, Berlin. 1984.
52. Yamazaki O, Tomishige K, Fujimoto K. Development of highly stable nickel catalyst for methane-steam reaction under low steam to carbon ratio. *Appl Catal A Gen.* 1996;136(1):49–56.
53. Choudhary T V, Goodman DW. Stepwise methane steam reforming: a route to CO-free hydrogen. *Catal Letters.* 1999;59(2–4):93–4.
54. Amin AM, Croiset E, Epling W. Review of methane catalytic cracking for hydrogen production. Vol. 36, *International Journal of Hydrogen Energy.* 2011. p. 2904–35.
55. Zhang T, Amiridis MD. Hydrogen Production via the Direct Cracking of Methane over Silica-Supported Nickel Catalysts. *Appl Catal A Gen.* 1998;167(2):161–72.
56. Holladay JD, Hu J, King DL, Wang Y. An overview of hydrogen production technologies. *Catal Today.* 2009 Jan [cited 2014 Jul 10];139(4):244–60.
57. Vernon PDF, Green MLH, Cheetham AK, Ashcroft AT. Partial oxidation of methane to synthesis gas. *Inorg Chem.* 1990;6(2):181–6.
58. Freni S, Calogero G, Cavallaro S. Hydrogen production from methane through catalytic partial oxidation reactions. *J Power Sources.* 2000 Apr [cited 2016 Feb 10];87(1–2):28–38.
59. Niakolas DK. Sulfur poisoning of Ni-based anodes for Solid Oxide Fuel Cells in H/C-based fuels. *Appl Catal A Gen.* 2014;486:123–42.
60. Niakolas DK, Athanasiou M, Dracopoulos V, Tsiaoussis I, Bebelis S, Neophytides SG. Study of the synergistic interaction between nickel, gold and molybdenum in novel modified NiO/GDC cermets, possible anode materials for CH₄ fueled SOFCs. *Appl Catal A Gen.* 2013;456:223–32.
61. Nikolla E, Schwank J, Linic S. Comparative study of the kinetics of methane steam reforming on supported Ni and Sn/Ni alloy catalysts: The impact of the formation of Ni alloy on chemistry. *J Catal.* 2009;263(2):220–7.
62. Niakolas DK, Athanasiou M, Neophytides SG, Bebelis S. Characterization and carbon tolerance of new Au-Mo-Ni/GDC cermet powders for use as anode materials in methane fuelled SOFCs. *ECS Trans.* 2011;35(2 PART 2):1329–36.

63. Niakolas DK, Ouweltjes JP, Rietveld G, Dracopoulos V, Neophytides SG. Au-doped Ni/GDC as a new anode for SOFCs operating under rich CH₄ internal steam reforming. *Int J Hydrogen Energy*. 2010 Aug [cited 2015 Nov 12];35(15):7898–904.
64. Nikolla E, Schwank J, Linic S. Promotion of the long-term stability of reforming Ni catalysts by surface alloying. *J Catal*. 2007;250(1):85–93.
65. Nikolla E, Schwank JW, Linic S. Hydrocarbon steam reforming on Ni alloys at solid oxide fuel cell operating conditions. *Catal Today*. 2008;136(3):243–8.
66. Demoret R. Nickel - A Brief History and Modern Application [Internet]. 2016.
67. Mills GA, Steffgen FW. Catalytic Methanation. *Catal Rev*. 1974 Jan 1;8(1):159–210.
68. Rostrup-Nielsen JR. Mechanisms of carbon formation on nickel-containing catalysts. *J Catal*. 1977 Jun [cited 2016 Feb 10];48(1–3):155–65.
69. Ananikov VP. Nickel: The “Spirited Horse” of Transition Metal Catalysis. *ACS Catal*. 2015 Mar 6;5(3):1964–71.
70. Freni S, Cavallaro S, Mondello N, Spadaro L, Frusteri F. Production of hydrogen for MC fuel cell by steam reforming of ethanol over MgO supported Ni and Co catalysts. *Catal Commun*. 2003;4(6):259–68.
71. Hegarty MES, O’Connor AM, Ross JRH. Syngas production from natural gas using ZrO₂-supported metals. *Catal Today*. 1998;42(3):225–32.
72. Murata K, Wang L, Saito M, Inaba M, Takahara I, Mimura N. Hydrogen Production from Steam Reforming of Hydrocarbons over Alkaline-Earth Metal-Modified Fe- or Ni-Based Catalysts. *Energy & Fuels*. 2004 Jan 1;18(1):122–6.
73. Li H, Li H, Dai W-L, Wang W, Fang Z, Deng J-F. XPS studies on surface electronic characteristics of Ni–B and Ni–P amorphous alloy and its correlation to their catalytic properties. *Appl Surf Sci*. 1999 Nov [cited 2016 Feb 9];152(1–2):25–34.
74. Okamoto Y. Surface state and catalytic activity and selectivity of nickel catalysts in hydrogenation reactions III. Electronic and catalytic properties of nickel catalysts. *J Catal*. 1980 Aug [cited 2016 Feb 9];64(2):397–404.
75. Ghenciu AF. Review of fuel processing catalysts for hydrogen production in PEM fuel cell systems. *Curr Opin solid state Mater Sci*. 2002;6(5):389–99.
76. Courson C, Makaga E, Petit C, Kiennemann A. Development of Ni catalysts for gas

- production from biomass gasification. Reactivity in steam- and dry-reforming. *Catal Today*. 2000 Dec [cited 2016 Feb 9];63(2–4):427–37.
77. Freni S, Mondello N, Cavallaro S, Cacciola G, Parmon VN, Sobyenin VA. Hydrogen production by steam reforming of ethanol: A two step process. *React Kinet Catal Lett*. 2000;71(1):143–52.
 78. Mariño FJ, Cerrella EG, Duhalde S, Jobbagy M, Laborde MA. Hydrogen from steam reforming of ethanol. characterization and performance of copper-nickel supported catalysts. *Int J Hydrogen Energy*. 1998;23(12):1095–101.
 79. Ashrafi M, Pfeifer C, Pröll T, Hofbauer H. Experimental study of model biogas catalytic steam reforming: 2. Impact of sulfur on the deactivation and regeneration of Ni-based catalysts. *Energy & Fuels*. 2008;22(6):4190–5.
 80. Halinen M, Saarinen J, Noponen M, Vinke IC, Kiviaho J. Experimental analysis on performance and durability of SOFC demonstration unit. *Fuel Cells*. 2010;10(3):440–52.
 81. Rasmussen JFB, Hagen A. The effect of H₂S on the performance of SOFCs using methane containing fuel. *Fuel Cells*. 2010;10(6):1135–42.
 82. Zhou X, Zhen J, Liu L, Li X, Zhang N, Sun K. Enhanced sulfur and carbon coking tolerance of novel co-doped ceria based anode for solid oxide fuel cells. *J Power Sources*. 2012;201:128–35.
 83. Ermakova M., Ermakov DY, Kuvshinov G. Effective catalysts for direct cracking of methane to produce hydrogen and filamentous carbon. *Appl Catal A Gen*. 2000 Jun [cited 2015 Dec 16];201(1):61–70.
 84. Kan H, Lee H. Sn-doped Ni/YSZ anode catalysts with enhanced carbon deposition resistance for an intermediate temperature SOFC. *Appl Catal B Environ*. 2010 Jun 9 [cited 2016 Jan 15];97(1–2):108–14.
 85. Saqib N, Porter JM. An impedance-based coke sensor for methane reforming systems. *Sensors Actuators, B Chem*. 2016;224:755–63.
 86. Steinfeld A, Kirillov V, Kuvshinov G, Mogilnykh Y, Reller A. Production of filamentous carbon and hydrogen by solarthermal catalytic cracking of methane. *Chem Eng Sci*. 1997 Oct [cited 2016 Feb 10];52(20):3599–603.

87. Suelves I, Lazaro M, Moliner R, Corbella B, Palacios J. Hydrogen production by thermo catalytic decomposition of methane on Ni-based catalysts: influence of operating conditions on catalyst deactivation and carbon characteristics. *Int J Hydrogen Energy*. 2005 Dec [cited 2016 Feb 10];30(15):1555–67.
88. Tsai T-I, Troskialina L, Majewski A, Steinberger-Wilckens R. Methane internal reforming in solid oxide fuel cells with anode off-gas recirculation. *Int J Hydrogen Energy*. 2015 Nov [cited 2016 Jan 2];41(1):553–61.
89. Choudhury IA, El-Baradie MA. Machinability of nickel-base super alloys: a general review. *J Mater Process Technol*. 1998;77(1–3):278–84.
90. Ezugwu EO, Wang ZM, Machado AR. The machinability of nickel-based alloys: a review. *J Mater Process Technol*. 1999 [cited 2017 Apr 25];86(1):1–16.
91. Ahmed K, Foger K. Kinetics of internal steam reforming of methane on Ni/YSZ-based anodes for solid oxide fuel cells. *Catal Today*. 2000;63(2):479–87.
92. Kan WH, Samson AJ, Thangadurai V. Trends in electrode development for next generation solid oxide fuel cells. *J Mater Chem A*. 2016;4(46):17913–32.
93. Araki M, Ponc V. Methanation of carbon monoxide on nickel and nickel-copper alloys. *J Catal*. 1976 Sep [cited 2017 Apr 25];44(3):439–48.
94. Lavoie J-M. Review on dry reforming of methane, a potentially more environmentally-friendly approach to the increasing natural gas exploitation. *Front Chem*. 2014;2(November):81.
95. Hou, Hughes. The kinetics of methane steam reforming over a Ni/ α -Al₂O₃ catalyst. *Chem Eng J*. 2001;82(1–3):311–28.
96. Laosiripojana N, Assabumrungrat S. Catalytic steam reforming of methane, methanol, and ethanol over Ni/YSZ: The possible use of these fuels in internal reforming SOFC. *J Power Sources*. 2007 Jan [cited 2016 Jan 12];163(2):943–51.
97. Nikoo MK, Amin NAS. Thermodynamic analysis of carbon dioxide reforming of methane in view of solid carbon formation. *Fuel Process Technol*. 2011 Mar;92(3):678–91.
98. Guerra C, Lanzini A, Leone P, Santarelli M, Brandon NP. Optimization of dry reforming of methane over Ni/YSZ anodes for solid oxide fuel cells. *J Power*

- Sources. 2014 Jan [cited 2015 Dec 9];245:154–63.
99. Hecht ES, Gupta GK, Zhu H, Dean AM, Kee RJ, Maier L, et al. Methane reforming kinetics within a Ni-YSZ SOFC anode support. *Appl Catal A Gen.* 2005;295(1):40–51.
 100. Lee J. Quantitative analysis of microstructure and its related electrical property of SOFC anode, Ni-YSZ cermet. *Solid State Ionics.* 2002 May 1 [cited 2017 Mar 13];148(1–2):15–26.
 101. Vivet N, Chupin S, Estrade E, Richard A, Bonnamy S, Rochais D, et al. Effect of Ni content in SOFC Ni-YSZ cermets: A three-dimensional study by FIB-SEM tomography. *J Power Sources.* 2011 Dec [cited 2017 Mar 13];196(23):9989–97.
 102. Koide H. Properties of Ni/YSZ cermet as anode for SOFC. *Solid State Ionics.* 2000 Jul 2 [cited 2017 Mar 13];132(3–4):253–60.
 103. He H, Gorte RJ, Vohs JM. Highly Sulfur Tolerant Cu-Ceria Anodes for SOFCs. *Electrochem Solid-State Lett.* 2005;8(6):A279.
 104. Gross MD, Vohs JM, Gorte RJ. A study of thermal stability and methane tolerance of Cu-based SOFC anodes with electrodeposited Co. *Electrochim Acta.* 2007 Jan [cited 2017 Mar 20];52(5):1951–7.
 105. Azad A-M, Duran MJ. Development of ceria-supported sulfur tolerant nanocatalysts: Rh-based formulations. *Appl Catal A Gen.* 2007 Oct 10 [cited 2017 Mar 20];330:77–88.
 106. Hibino T, Hashimoto A, Suzuki M, Sano M. A Solid Oxide Fuel Cell Using Y-Doped BaCeO₃ with Pd-Loaded FeO Anode and Ba_{0.5}Pr_{0.5}CoO₃ Cathode at Low Temperatures. *J Electrochem Soc.* 2002;149(11):A1503–8.
 107. Rossmeisl J, Bessler WG. Trends in catalytic activity for SOFC anode materials. *Solid State Ionics.* 2008;178(31–32):1694–700.
 108. Caillot T, Gelin P, Dailly J, Gauthier G, Cayron C, Laurencin J. Catalytic steam reforming of methane over La_{0.8}Sr_{0.2}CrO₃ based Ru catalysts. *Catal Today.* 2007;128(3–4):264–8.
 109. Bebelis S, Neophytides S, Kotsionopoulos N, Triantafyllopoulos N, Colomer MT, Jurado J. Methane oxidation on composite ruthenium electrodes in YSZ cells. *Solid*

- State Ionics. 2006;177(19–25 SPEC. ISS.):2087–91.
110. Gorte RJ, Kim H, Vohs JM. Novel SOFC anodes for the direct electrochemical oxidation of hydrocarbon. *J Power Sources*. 2002;106(1–2):10–5.
 111. Xiao G, Liu Q, Dong X, Huang K, Chen F. $\text{Sr}_2\text{Fe}_{4/3}\text{Mo}_{2/3}\text{O}_6$ as anodes for solid oxide fuel cells. *J Power Sources*. 2010;195(24):8071–4.
 112. Huang Y-H, Dass RI, Xing Z-L, Goodenough JB. Double Perovskites as Anode Materials for Solid-Oxide Fuel Cells. *Science* (80-). 2006;312(5771):254–7.
 113. Zhang P, Huang YH, Cheng JG, Mao ZQ, Goodenough JB. $\text{Sr}_2\text{CoMoO}_6$ anode for solid oxide fuel cell running on H_2 and CH_4 fuels. *J Power Sources*. 2011;196(4):1738–43.
 114. Li X, Zhao H, Xu N, Zhou X, Zhang C, Chen N. Electrical conduction behavior of La, Co co-doped SrTiO_3 perovskite as anode material for solid oxide fuel cells. *Int J Hydrogen Energy*. 2009;34(15):6407–14.
 115. Gorte RJ, Vohs JM, McIntosh S. Recent developments on anodes for direct fuel utilization in SOFC. In: *Solid State Ionics*. 2004. p. 1–6.
 116. Troskialina L, Dhir A, Steinberger-Wilckens R. Improved Performance and Durability of Anode Supported SOFC Operating on Biogas. *ECS Trans*. 2015;68(1):2503–13.
 117. Kan H, Hyun SH, Shul YG, Lee H. Improved solid oxide fuel cell anodes for the direct utilization of methane using Sn-doped Ni/YSZ catalysts. *Catal Commun*. 2009;11(3):180–3.
 118. Hornés A, Gamarra D, Munuera G, Conesa JC, Martínez-Arias A. Catalytic properties of monometallic copper and bimetallic copper-nickel systems combined with ceria and Ce-X (X=Gd, Tb) mixed oxides applicable as SOFC anodes for direct oxidation of methane. *J Power Sources*. 2007 [cited 2017 Apr 17];169(1):9–16.
 119. Sin A, Kopnin E, Dubitsky Y, Zaopo A, Aricò AS, La Rosa D, et al. Performance and life-time behaviour of NiCu–CGO anodes for the direct electro-oxidation of methane in IT-SOFCs. *J Power Sources*. 2007;164(1):300–5.
 120. An W, Gatewood D, Dunlap B, Turner CH. Catalytic activity of bimetallic nickel alloys for solid-oxide fuel cell anode reactions from density-functional theory. *J*

- Power Sources. 2011;196(10):4724–8.
121. Niakolas DK, Athanasiou M, Dracopoulos V, Tsiaoussis I, Bebelis S, Neophytides SG. Study of the synergistic interaction between nickel, gold and molybdenum in novel modified NiO/GDC cermets, possible anode materials for CH₄ fueled SOFCs. *Appl Catal A Gen.* 2013;456:223–32.
 122. Huang T-J, Huang M-C, Huang M-S. Novel methane steam-reforming catalyst of Ni-Bi₂O₃/GDC to reduce CO for hydrogen production. *Appl Catal A Gen.* 2009;354(1):127–31.
 123. Park HC, Virkar A V. Bimetallic (Ni–Fe) anode-supported solid oxide fuel cells with gadolinia-doped ceria electrolyte. *J Power Sources.* 2009;186(1):133–7.
 124. Kan H, Lee H. Enhanced stability of Ni–Fe/GDC solid oxide fuel cell anodes for dry methane fuel. *Catal Commun.* 2010;12(1):36–9.
 125. da Paz Fiuza R, Da Silva MA, Boaventura JS. Development of Fe–Ni/YSZ–GDC electrocatalysts for application as SOFC anodes: XRD and TPR characterization and evaluation in the ethanol steam reforming reaction. *Int J Hydrogen Energy.* 2010;35(20):11216–28.
 126. Souentie S, Athanasiou M, Niakolas DK, Katsaounis a., Neophytides SG, Vayenas CG. Mathematical modeling of Ni/GDC and Au–Ni/GDC SOFC anodes performance under internal methane steam reforming conditions. *J Catal.* 2013;306:116–28.
 127. Hibino T, Hashimoto A, Asano K, Yano M, Suzuki M, Sano M. An intermediate-temperature solid oxide fuel cell providing higher performance with hydrocarbons than with hydrogen. *Electrochem solid-state Lett.* 2002;5(11):A242–4.
 128. Modafferi V, Panzera G, Baglio V, Frusteri F, Antonucci PL. Propane reforming on Ni–Ru/GDC catalyst: H₂ production for IT-SOFCs under SR and ATR conditions. *Appl Catal A Gen.* 2008;334(1):1–9.
 129. Hibino T, Hashimoto A, Yano M, Suzuki M, Sano M. Ru-catalyzed anode materials for direct hydrocarbon SOFCs. *Electrochim Acta.* 2003;48(17):2531–7.
 130. Nabae Y, Yamanaka I, Hatano M, Otsuka K. Catalytic behavior of Pd–Ni/composite anode for direct oxidation of methane in SOFCs. *J Electrochem Soc.* 2006;153(1):A140–5.

131. Nabae Y, Yamanaka I, Hatano M, Otsuka K. Mechanism of Suppression of Carbon Deposition on the Pd– Ni/Ce (Sm) O₂– La (Sr) CrO₃ Anode in Dry CH₄ Fuel. *J Phys Chem C*. 2008;112(27):10308–15.
132. Boaro M, Modafferi V, Pappacena A, Llorca J, Baglio V, Frusteri F, et al. Comparison between Ni–Rh/gadolinia doped ceria catalysts in reforming of propane for anode implementations in intermediate solid oxide fuel cells. *J Power Sources*. 2010;195(2):649–61.
133. Ferrandon M, Kropf AJ, Krause T. Bimetallic Ni-Rh catalysts with low amounts of Rh for the steam and autothermal reforming of n-butane for fuel cell applications. *Appl Catal A Gen*. 2010;379(1):121–8.
134. Gavrielatos I, Montinaro D, Orfanidi A, Neophytides SG. Thermogravimetric and Electrocatalytic Study of Carbon Deposition of Ag-doped Ni/YSZ Electrodes under Internal CH₄ Steam Reforming Conditions. *Fuel Cells*. 2009 Dec 1 [cited 2017 Aug 23];9(6):883–90.
135. Nikolla E, Schwank J, Linic S. Measuring and Relating the Electronic Structures of Nonmodel Supported Catalytic Materials to Their Performance. *J Am Chem Soc*. 2009 Feb 25;131(7):2747–54.
136. Singh A, Hill JM. Carbon tolerance, electrochemical performance and stability of solid oxide fuel cells with Ni/yttria stabilized zirconia anodes impregnated with Sn and operated with methane. *J Power Sources*. 2012 Sep [cited 2016 Jan 14];214:185–94.
137. Troskialina L. Improved Performance of Solid Oxide Fuel Cell Operating on Biogas using Tin Anode-infiltration. University of Birmingham; 2015.
138. Schmetterer C, Flandorfer H, Richter KW, Saeed U, Kauffman M, Roussel P, et al. A new investigation of the system Ni–Sn. *Intermetallics*. 2007;15(7):869–84.
139. Nikolla E, Schwank JW, Linic S. Hydrocarbon steam reforming on Ni alloys at solid oxide fuel cell operating conditions. *Catal Today*. 2008;136(3):243–8.
140. Helveg S, López-Cartes C, Sehested J, Hansen PL, Clausen BS, Rostrup-Nielsen JR, et al. Atomic-scale imaging of carbon nanofibre growth. *Nature*. 2004;427(6973):426–9.

141. Haanappel V a C, Mai a., Mertens J. Electrode activation of anode-supported SOFCs with LSM- or LSCF-type cathodes. *Solid State Ionics*. 2006;177(19–25 SPEC. ISS.):2033–7.
142. Grant JT. *X-Ray Photoelectron Spectroscopy (XPS/ESCA)*. Newcastle: University of Newcastle; 2016. p. 204.
143. Fergus J, Hui R, Li X, Wilkinson DP, Zhang J. *Solid oxide fuel cells: materials properties and performance*. CRC press; 2016.
144. Blum L, Buchkremer HP, Gross S, Gubner A, De Haart LGJ, Nabielek H, et al. Solid oxide fuel cell development at Forschungszentrum Juelich. In: *Fuel Cells*. 2007. p. 204–10.
145. Thermo Scientific XPS [Internet].
<https://xpssimplified.com/periodictable.php>[accessed on August 2017]
146. X-ray Photoelectron Spectroscopy (XPS) Reference Pages.
<http://www.xpsfitting.com/search/label/Nickel> [accessed on August 2017]
147. Biesinger MC, Lau LWM, Gerson AR, Smart RSC. Resolving surface chemical states in XPS analysis of first row transition metals, oxides and hydroxides: Sc, Ti, V, Cu and Zn. *Appl Surf Sci*. 2010;257(3):887–98.
148. Biesinger MC, Payne BP, Lau LWM, Gerson A, Smart RSC. X-ray photoelectron spectroscopic chemical state Quantification of mixed nickel metal, oxide and hydroxide systems. *Surf Interface Anal*. 2009;41(4):324–32.
149. Stevenson J. SOFC seals: materials status. In: *SECA Core Technology Program-SOFC Seal Meeting*. 2003.
150. O'hayre R, Cha S-W, Prinz FB, Colella W. *Fuel cell fundamentals*. John Wiley & Sons; 2016.
151. Hagelin-Weaver HAE, Weaver JF, Hoflund GB, Salaita GN. Electron energy loss spectroscopic investigation of Ni metal and NiO before and after surface reduction by Ar⁺ bombardment. *J Electron Spectros Relat Phenomena*. 2004;134(2–3):139–71.
152. Jiang M, Li Y, Lu Z, Sun X, Duan X. Binary Nickel-iron Nitride Nanoarrays as Bifunctional Electrocatalysts for Overall Water Splitting. *Inorg Chem Front*. 2016;3(5):630–4.

